Enhanced Treatment Planning and Navigation for Image-Guided Microwave Ablation of Hepatic Tumors

By

Jarrod Collins

Dissertation

Submitted to the Faculty of the

Graduate School of Vanderbilt University

in partial fulfillment of the requirements

for the degree of

DOCTOR OF PHILOSOPHY

in

Biomedical Engineering

December 15, 2018

Nashville, Tennessee

Approved:

Michael I. Miga, Ph.D.

Brett C. Byram, Ph.D.

William A. Grissom, Ph.D.

Benoit M. Dawant, Ph.D.

Daniel B. Brown, M.D.

ACKNOWLEDGMENTS

I would like to begin by first acknowledging and thanking the many people that have provided their support throughout this endeavor.

I would like to thank my dissertation committee, Dr. Mike Miga, Dr. Brett Byram, Dr. Will Grissom, Dr. Benoit Dawant, and Dr. Dan Brown, for guiding and teaching me through this work and for providing life and career advice along the way. I would like to especially thank my advisor, Dr. Miga, for always pushing further and asking the hard questions – without which, this work would not be what it is today. Dr. Miga has been a valuable mentor and provided much appreciated support to my academic and professional interests.

In addition, I would like to acknowledge the National Institutes of Health grant R01CA162477 from the National Cancer Institute for providing necessary funding and Perseon Medical for providing essential equipment for the completion of this research.

I am grateful to the many people that I have worked with within the Biomedical Modeling Laboratory at Vanderbilt over the years. In particular, I would like to sincerely thank Dr. Jared Weis and Dr. Logan Clements for their patience and guidance in helping me to understand and develop some of the more technical features of this work. Furthermore, I would like to thank the current and former members of our lab for their helpful discussions, both personal and professional, and their help with experiments and data collection. I am also extremely grateful to our clinical collaborators at Memorial Sloan Kettering Cancer Center, Dr. Amber Simpson and Dr. Bill Jarnagin.

Most of all I would like to thank my family and friends for their support. I am especially thankful to my parents and my closest friend, my future wife Taylor, for their motivation and encouragement.

TABLE OF CONTENTS

Page

TABLE OF CONTENTS

Page

TABLE OF CONTENTS

Page

LIST OF TABLES

LIST OF FIGURES

LIST OF FIGURES

LIST OF FIGURES

Figure Page

LIST OF FIGURES

LIST OF FIGURES

Figure Page

Chapter I

Introduction

I.1 Specific Aims

Primary and metastatic liver cancers are a considerable and increasing U.S. and global health concern. Patients presenting with hepatic tumors are preferably treated with surgical resection which has a record of long-term patient survival. While resection has proven effective and can be potentially curative, constraints associated with risk and patient suitability narrow the population of patients eligible to receive this approach to only around 10-30%. More local therapies, such as thermal ablation, have received increased indications for use in recent years including the treatment of surgically unresectable malignancies. A combination of recent advances in neoadjuvant care, therapeutic options, and improved patient selection criterion have improved the survival rate of patients receiving primary ablative treatments for hepatic cancers to be comparable to the clinical standard set by surgical resection. As they inherently target internal structures, the efficacy of ablation methods is highly reliant on accurate localization and targeting of subsurface anatomies during a procedure, as inaccurate delivery can lead to incomplete treatment and local recurrence.

This dissertation advances image-guided hepatic microwave ablation by developing methods which provide enhanced procedural planning and intraoperative tumor localization. A true multiphysics framework is developed herein which utilizes patient-specific therapeutic predictive modeling and advanced surgical navigation methodologies. The guidance approach applied in this work creates a spatial mapping between information-rich preoperatvely acquired image data and the state of the patient during therapy. This

registration is further enhanced by the application of a biomechanical model which corrects for soft-tissue deformation that occurs peri-operatively. This approach allows physicians to effectively navigate to a targeted lesion by using the registered and corrected preoperative image data for intraoperative guidance. Furthermore, this work develops and presents a proof-of-concept for image-data driven patient-specific predictive modeling of microwave ablation. This is the first work to demonstrate a model-based therapeutic and guidance framework for hepatic ablation procedures. The results demonstrate the feasibility of such a multiphysics approach and represent a significant advancement towards a more comprehensive model-predictive paradigm for an important image-guided therapeutic process in use today.

The primary objective of this dissertation was to advance image-guided hepatic microwave ablation by developing methods which provide enhanced procedural planning and intraoperative anatomical localization. The following tasks were accomplished to meet this goal: 1) methods were developed to address variations in image-to-physical registration data quality which can present between cases and physicians, 2) a deformation correction method was applied within the context of image-to-physical registration for image-guided microwave ablation, 3) a procedural model of hepatic microwave ablation procedures was developed, and 4) these methods were evaluated within the scope of phantom and clinical data. The results and applications presented in this work represent an important advancement in the field of image-guided hepatic microwave ablation. The breadth of this dissertation was defined by the following specific aims.

I.1.1 Aim 1: Advances in Image-Guidance Techniques

The first aim of this project was to improve upon current image-guided liver surgery

(IGLS) techniques by developing a sparse surface data resampling method to normalize the quality and extent of intraoperatively collected IGLS data. Further, a procedure for creating clinically-inspired ground truth phantom data was developed. This human-to-phantom data framework provides a valuable methodology for current and future IGLS methods validation. Its use within this study allowed for the characterization of the accuracy and variation associated with current IGLS localization methods as well as the newly developed data resampling approach.

I.1.2 Aim 2: Application of Deformation Correction to Image-Guided Ablation

The second aim of this project was to apply multiphysics modeling for comprehensive guidance in image-guided hepatic microwave ablation. A retrospective, best-fit model of microwave ablation was developed and applied alongside current rigid and deformation correction IGLS registration methods. The combined methods were evaluated within a series of clinically-relevant deformable hepatic ablation phantoms and represent the first application and evaluation of a combined procedural modeling and enhanced image-guidance approach for hepatic microwave ablation procedures.

I.1.3 Aim 3: Prospective Computational Modeling of Microwave Ablation

The final aim of this project was to develop a truly prospective patient-specific model of microwave ablation procedures. The method developed in this aim modified the previous approach developed in Aim 2 by approximating patient-specific tissue properties based from a prior quantitative medical imaging of tissue fat content. The model was evaluated with observed ablation extent and temperature profiles within a series of agar-albumin ablation phantoms and represents an advancement towards image-data driven

patient-specific predictive procedural modeling.

I.2 Dissertation Overview

This dissertation begins in Chapter II with an introduction to the clinical significance of liver cancers, image-guidance techniques, and the fundamental basis and current research trends for hepatic microwave ablation procedural modeling. A thorough description of the common methods used throughout the aims of this project are presented in Chapter III, including patient and phantom data collection and image-to-physical registration. The following chapters of this dissertation go into detail regarding the previously defined specific aims. Chapter IV describes the development and results of the human-to-phantom data framework and surface data resampling method. Chapter V describes the development of a retrospective, best-fit microwave ablation model and its application alongside current IGLS techniques in phantom image-guided microwave ablation procedures. Chapter VI defines a methodology which further develops the microwave ablation model from Chapter V into a truly prospective approach which exploits quantitative medical imaging of organ fat content. Finally, Chapter VII presents the overall contributions and conclusions of this dissertation and suggests future directions for investigation.

Chapter II

Background

II.1 Clinical Significance and Management

Primary and metastatic liver cancers are an increasing U.S. and global health concern. With an estimated 145,000 cases annually, colorectal cancer is the 3rd most diagnosed cancer in the U.S [1]. Additionally, upwards of 35% of colorectal cancer patients at the time of surgery and 70% in the lifespan of their disease are estimated to present with liver metastases [2-7]. When combined with an annually estimated 40,000 new diagnoses of primary liver cancer, liver tumors are present in greater than 5% of U.S. cancer diagnoses each year [1]. Furthermore, when considering the lifespan of these diseases and mortality, liver tumors contribute to greater than 10% of annual cancer-related deaths in the U.S. [1]. Additionally, although less common, metastatic liver cancer can arise from primary breast, esophageal, stomach, pancreatic, lung, kidney, skin, and other cancers. Globally, over 782,000 primary liver cancer and 1.36 million colorectal cancer patients are diagnosed annually, contributing to over 1.23 million deaths [8].

Preferably, patients presenting with primary and metastatic hepatic tumors are treated with surgical resection [9-10] due to a record of long-term patient survival (e.g. providing five-year survival of 44-50% in patients with metastatic colorectal cancer [11]). Recent advances in surgical approach have expanded the indications for hepatic resection to include patients with more complex disease and therefore improved patient eligibility. Additionally, more complex procedures (e.g. two-stage hepatectomy [12], multi-segment resection [13-14], and ablation assisted resection [12-14]) are now being performed. These advances are in part due to improvements in procedural safety and the application of advanced image-

guidance and surgical navigation techniques. Such methods aim to provide accurate localization of relevant anatomical structures for the real-time guidance of surgical procedures. Treatment selection for hepatic tumors requires the consideration of multiple factors such as the number and distribution of lesions, accessibility of vascular control, the presence of extrahepatic disease, and the expected residual volume of functional liver. While resection has proven effective and can be potentially curative, more aggressive approaches risk impairing normal liver function which can lead to post-operative liver failure [15]. With these considerations, only between 10-30% of patients are eligible for surgical resection [16-17].

Loco-regional therapies, such as thermal ablation, have received increased indications for use in neoadjuvant roles, ablation assisted resection, and for the treatment of unresectable hepatic malignancies [18-30] and can be performed in open, laparoscopic, or percutaneous settings. While radiofrequency ablation (RFA) is the most common ablative therapy used clinically, it has presented a relatively high local recurrence rate (12-39%) when compared to microwave ablation (MWA) (6-8.8%) [20-24]. Additionally, in matched cohort studies, patients receiving MWA saw improved survival compared to those receiving RFA [21-22]. Furthermore, MWA has received considerable interest due to its larger spatial extent of power distribution, penetration through charred tissues, and ability to ablate up to and around large vessels [21-22, 31]. Due to advances in neoadjuvant care, therapeutic options, and improved patient selection criterion, the 5-year survival rate for patients receiving ablation treatments for hepatic colorectal cancer metastases has improved from 18.9% in 2000 to 53.3% in 2014 [29]. More recent studies specifically concerning MWA treatment presented 4-year survival rates of 58.3% when treating colorectal cancer metastases and 79.4% for other pathologies [18] and median survival of 38.3 months for hepatocellular

carcinoma and 36.3 months for colorectal cancer metastases [19].

II.2 Image-Guidance

As they inherently target internal structures, the efficacy of ablation and resection procedures is highly reliant on accurate localization and targeting of subsurface anatomies during a procedure, as inaccurate delivery can lead to incomplete treatment and local recurrence [32]. As such, ablations are generally performed using image-guidance (e.g. traditionally intraoperative ultrasound imaging (iUS) or computed tomography (CT)) to assist in tumor localization and probe placement. Image-guidance, in medicine, is a broad term which has come to encompass the use of imaging modalities which augment the delivery of therapy and can be utilized in any of the following distinct ways: planning, assessment, targeting, and monitoring [33]. Planning and assessment are generally perioperative applications of image-guidance. Planning in image-guidance has come to encompass the use of imaging data to diagnose, determine patient suitability, and to develop a procedural plan. Assessment entails the use of postoperative medical imaging (either immediately or in follow-up) to gauge the success of therapeutic delivery. Targeting and monitoring applications of image-guidance are utilized during therapeutic delivery. Targeting is the use of imaging to improve the localization and efficacy of therapeutic delivery (e.g. ablation antenna, biopsy needle, or resection plane). Ideal targeting systems provide clear localization of the tumor, procedural hardware, and other relevant critical anatomy in real-time [34-36]. For the purposes of ablation, physicians rely heavily on 2D iUS for targeting; however, techniques have been described for more workflow cumbersome modalities such as intraoperative CT and MRI [37]. Monitoring in image-guidance describes imaging to observe the impact of a procedure during application. MRI and US techniques

have both been described for visualizing the thermal fronts associated with ablation, however MRI is currently the only imaging modality with well-validated temperature monitoring for temperatures exceeding 50°C [38].

However, with these methods, real-time localization, monitoring, and assessment are still extremely limited in the operating room. Advanced surgical navigation approaches have been used to create a spatial mapping between surgical instrumentation and imaging data to improve visualization of anatomical structures. These techniques allow for the tracking of surgical tools in the operating room and viewing of their predicted location in the information-dense preoperative image data. The following sections discuss the historical development of surgical navigation for image-guidance within the liver and current state-of-the-art techniques.

II.2.1 Rigid Registration and Image-Guided Liver Surgery

Several studies have investigated image-to-physical registration methods for application in IGLS. Rigid registration techniques were first developed to align preoperatively acquired image data to a representation of physical space in the operating room. This alignment has generally been achieved using point-based or surface-based methods. For point-based rigid registration methods, corresponding points are acquired in both image and physical space. These points may represent particular anatomical landmarks or artificial fiducial markers. Such point-based registration methods provide an optimal rigid body transformation that aligns the corresponding points but are therefore highly influenced by the accuracy of demarcating points (i.e. fiducial localization error (FLE)). These point-based techniques are not readily applicable in soft-tissue registration scenarios such as the liver, where precise surface features are absent.

For surface-based rigid registration methods, corresponding surfaces, rather than points, are aligned. Often iterative in nature, these algorithms search to minimize an objective function that is typically defined by a measure of residual closest point distance between the two surfaces. For example, the iterative closest point (ICP) algorithm conducts a series of point-based registrations, determining a new point correspondence at each iteration and continuing until the selected objective function is minimized [39]. Such methods are limited in their ability to determine true surface correspondence and are therefore dependent on a reasonable initial orientation.

Cash et al. described a method of rigid registration for IGLS that determines an initial rigid image-to-physical alignment through a point-based fiducial registration that was then followed by a surface-based ICP registration [40]. However, this method was still influenced and hindered by the identification of anatomical fiducials in soft-tissue (i.e. FLE) [41]. A current clinical protocol for surface-based rigid registration in IGLS was introduced by Clements et al. [42]. This salient-feature weighted ICP rigid image-to-physical registration utilizes homologous anatomical features that can be identified in both image and physical space (e.g. the falciform ligament, left and right inferior ridges, and round ligament) to bias point correspondence estimation at each iteration of the ICP registration. The biased weighting scheme is dynamic through iterations of the algorithm allowing the anatomical features to produce a robust initial alignment while providing support to the digitized organ surface in later iterations. With this method, correspondence is estimated using a conventional closest point operator with a weighting scheme which biases correspondence between points identified to belong to homologous features. The algorithm provides a rigid transformation which minimizes the distance between the surface of a 3D model generated from preoperative imaging and the digitized intraoperative organ surface data.

II.2.2 Image-Guided Ablation Procedures

Recent applications of such work to image-guided ablation procedures have reported enhanced localization of tumors and improved accuracy of ablation antenna placement in open [43-47] and laparoscopic procedures [48-50]. These methods have employed a variety of electromagnetic (EM) tracking and image-to-physical registration methods to provide enhanced image-guidance. Sindram et al. intraoperatively tracked the real-time position and orientation of an ablation antenna and iUS image plane using optical [45] and later EM-tracking strategies [48]; presenting the physician with an enhanced 3D US image with visualization of the ablation antenna tip. In a study by Hammill et al., MWA antennas were placed using iUS-guidance with optical tracking. Rigid image-to-physical feature-based registration was used to display the tracked iUS and ablation antenna within the preoperative image space [46]. In a similar study, Banz et al. determined image-to-physical space registrations to visualize optically tracked intraoperative tools in relation to preoperative imaging data using landmark-based and iUS vessel-based alignment strategies [47]. Recently, such methods have been applied to the laparoscopic environment using EM-tracked enhanced US guidance [49] and optical tracking with landmark based image-to-physical registration [50]. These techniques have presented greater efficiency in MWA antenna placement and higher procedural success in comparison to purely iUS guided prior studies. However, to date, image-guided ablation methods providing image-to-physical registration have been limited to rigid registration approaches, which neglect soft-tissue deformations that occur from organ mobilization during procedures and can cause substantial registration error [51]. EM-tracking methods avoid this issue by limiting tracking to the real-time position of surgical tools and iUS imaging. However, when compared to image-to-physical registration the EM-tracking approach limits the subsurface information that is

provided and loses efficacy when targeting lesions in cirrhotic patients or in those with chemotherapy-induced hyperechogenicity associated with steatosis, both which can compromise ultrasound lesion visualization [52-54].

II.2.3 Deformation Correction

A 2005 review by Hawkes et al. identified critical limitations of rigid-based registrations in soft tissue environments [51]. In the surgical and laparoscopic settings, the organ is first separated from abdominal ligamenture and often mobilized for surgical presentation by posteriorly placing supportive packing material. These changes in support manifest as deformations (i.e. global shape changes) when comparing the organ in imaging data to the intraoperative state. Several model-based soft-tissue deformation correction approaches have been presented in the literature for image-to-physical registration for hepatic resection. For example, Lange et al. published an algorithm using thin-plate splines to deform preoperatively acquired vessels to intraoperative vessels acquired from tracked iUS [55]. More recently, Hu et al. presented a method using coherent point drift to nonrigidly register vessel landmarks, such as bifurcations [56]. Alternatively, other approaches have concentrated on achieving surface-based deformation correction methods. Miga et al. proposed a biomechanical model for neurosurgery driven by laser range scan (LRS) surface acquisition which was validated with residual surface error [57]. Cash et al. introduced a linear elastic model approach to incrementally apply closest point boundary conditions to deform a preoperative organ model to intraoperatively collected sparse surface data following rigid registration [58]. Dumpuri et al. then improved upon these methods by applying a surface Laplacian based filter to improve the determination of boundary conditions [59]. Rucker et al. described an inverse approach which optimizes boundary

conditions described by a parameterized posterior displacement field, based on the reality of organ deformation during operative mobilization, to minimize the residual error between the intraoperatively collected anterior surface digitization and the deformed model surface [60]. More recently, Heiselman et al. expanded upon the work of Rucker et al. by reformulating the application of boundary conditions to a control point strategy which allows for multiple independent support surfaces to be designated [61]. Both methods have demonstrated effective correction of soft-tissue deformation in phantom and clinical applications for hepatic resection [60-64].

II.3 Procedural Planning Methods

For planning ablation procedures, MWA device manufacturers currently provide 2D specifications for generating expected ablation volumes given specific power and time settings. These estimates are empirically derived from ablations observed within *ex vivo* animal tissue. In doing so, these models ignore the influence of patient-specific anatomical variation, tissue heterogeneity, cross-patient differences in disease state, and tissue perfusion. As a result, the manufacturer specifications are often larger and more uniform than clinically observed ablations [65-66]. Moreover, there is often no integration of these 2D predictions with the 3D patient images, placing burden on the physician to mentally reconstruct and compare complex volumes. The development of clinically accurate, computational models of MWA procedures presents a powerful alternative to the ablation zone estimates provided by manufacturers and a lower-cost, less cumbersome alternative to interventional imaging strategies.

Computational models of MWA employ numerical methods to solve the differential equations governing electromagnetic wave propagation, power deposition, and biological

heat transfer and have been investigated within the literature for two distinct purposes: (1) assisting the optimization of ablation hardware design [67-71] and (2) more recently towards the eventual development of patient-specific treatment planning [72-76]. For clinical application, research into these approaches seeks to provide more accurate and reliable estimates of personalized procedures for the purposes of planning, guidance, and assessment. When considering the shortcomings of the manufacturer provided estimates, computational models tailored to an individual could incorporate specifications for geometric, dielectric, and thermal properties of the tissue. Sensitivity studies performed on models of 2.45 GHz MWA have expressed the extensive influence that these tissue properties have on MWA models, especially the dielectric properties and the rate of blood perfusion [77-78]. Recent studies at both 915 MHz and 2.45 GHz frequencies have incorporated tissue properties that vary as a function of temperature as derived from experimental measurements [74-76] or due to dynamic changes in tissue water content and blood perfusion [79-83].

However, an inherent shortcoming in these models is that they neglect the variation in material properties that can occur between patients. A recent study in MWA antenna design concluded that there is a need for more accurate and comprehensive modeling of dielectric and thermal tissue properties [71]. Presently, patient-specific organ material properties are unavailable in a clinical setting. As such, these various models of tissue properties are often derived from experimental conditions in *ex vivo* animal tissue. Furthermore, there is clear variation when considering patients presenting with other common disease states such as cirrhosis or fatty liver disease [84-85]. Therefore, a need exists for modeling frameworks that account for patient-specific variations in the state of organ tissue and disease. One possibility is to use MRI [86] or US [87] methods to non-invasively measure quantities that could be correlated to material property changes (e.g.

varying liver fat content may significantly affect dielectric and thermal properties). Therefore, there exists potential that *a priori* knowledge of organ disease state, such as this, may be used to facilitate predictive modeling of thermal ablation.

The following sections will discuss the foundational basis for the computational modeling of microwave ablation, modeling approaches in the literature, approaches to determining relevant material properties, and preoperative planning methods.

II.3.1 Computational Modeling of Microwave Ablation

Computational models of MWA employ numerical methods to solve the differential equations governing electromagnetic wave propagation, power deposition, and biological heat transfer and can be used to predict the volume of tissue damage induced during therapy. Tissue damage is a function of temperature and length of exposure. Therefore, accurate prediction of temperature development and distribution is crucial. Thermal development is a product of the deposition of microwave energy within the tissue and subsequent heat transfer to neighboring tissue. The following text will review the computational framework used to approximate these phenomena and the resulting tissue damage.

II.3.1.1 Electromagnetic Wave Propagation

The motion and absorption of microwaves in tissue is governed by Maxwell's equations (presented in both differential and phasor form):

$$\nabla \cdot \vec{E} = \frac{\rho}{\varepsilon} \quad \text{Eq. II.1}$$

$$\nabla \cdot \vec{H} = 0 \quad \text{Eq. II.2}$$

$$\nabla \times \vec{E} = -\frac{\partial \vec{B}}{\partial t} \qquad \nabla \times \vec{E} = -j\omega\mu\vec{H} \qquad \text{Eq. II.3}$$

$$\nabla \times \vec{H} = \sigma\vec{E} + \varepsilon\frac{\partial \vec{E}}{\partial t} \qquad \nabla \times \vec{H} = j\omega\varepsilon_c\vec{E} \qquad \text{Eq. II.4}$$

where $\vec{E}$ [V/m] is the electric field strength, $\vec{H}$ [A/m] is the magnetic field strength, ρ [C/m^2] is the free charge density, ω [rad/s] is the angular frequency of the electromagnetic wave, ε [F/m] is the permittivity, and μ [H/m] is the permeability. Eq. II.1, II.3, and II.4 may be combined under the assumption that no initial charge is present within the medium to arrive at the electromagnetic wave equation – which describes the propagation of electromagnetic waves through a medium (presented in both differential and phasor form).

$$\left(\nabla^2 - \mu\varepsilon\frac{\partial^2}{\partial t^2}\right)\vec{E} = 0 \qquad (\nabla^2 + \omega^2\mu\varepsilon_c)\vec{E} = 0 \qquad \text{Eq. II.5}$$

Eq. II.5 describes the propagation of electromagnetic waves through a medium. The absorption of electromagnetic power in tissue is a function of electrical conductivity σ [S/m] and dielectric permittivity ε [F/m]. Electromagnetic energy deposition in a medium is characterized by the medium's loss tangent, which is defined as σ/ωε. The medium is considered to be a low loss material, i.e. one that does not absorb much energy from a propagating wave, when $\sigma/\omega\varepsilon << 1$. A medium is considered lossy when $\sigma/\omega\varepsilon \sim 1$, in which case the material absorbs a large amount of energy from propagating electromagnetic waves. The loss tangent of a material may further be lumped together as a single, complex valued number known as the complex permittivity:

$$\varepsilon_c = \varepsilon_r - j\frac{\sigma}{\omega\varepsilon_0} \qquad \text{Eq. II.6}$$

where ε_r is the real relative permittivity of the material and ε_0 is the permittivity of free space. Most organ tissue is considered lossy and in soft tissue particularly, both σ and ε have been shown to vary with frequency, temperature, and water content. Therefore, for the

development of a wholly accurate ablation model it is important to characterize a tissue's electromagnetic properties.

II.3.1.2 Biological Heat Transfer

For modeling of thermal development and heat transfer the temperature profile in tissue is most often solved using Pennes bioheat equation:

$$\rho c \frac{\partial T}{\partial t} = \nabla \cdot k \nabla T + Q - Q_p + Q_m \quad \text{Eq. II.7}$$

where ρ [kg/m^3] is mass density, c [J/kg·K] is specific heat capacity, k [W/m·K] is thermal conductivity, T [K] is temperature, Q [W/m^3] is heat generation due to absorbed electromagnetic energy, Q_p [W/m^3] is heat loss due to perfusion, and Q_m [W/m^3] is metabolic heat generation. Heat loss due to perfusion is calculated as follows:

$$Q_p = \omega_{blood} c_{blood} (T - T_{blood}) \quad \text{Eq. II.8}$$

where ω_{blood} [kg/m^3·s] is the blood perfusion rate, c_{blood} [J/kg·K] is the specific heat capacity of blood, and T_{blood} [K] is the blood temperature, 310.15°K (37°C). Metabolic heat generation is often assumed to be negligible. Heat generation due to the absorbed electromagnetic energy is computed directly from the electric field distribution:

$$Q = \frac{1}{2} \sigma |E|^2 \quad \text{Eq. II.9}$$

Specific absorption rate (SAR) is often reported in the literature and is Q normalized by tissue density. Both k and c vary with temperature and water content. Therefore, characterization of these properties is essential to the accurate prediction of temperature.

II.3.1.3 Prediction of Tissue Necrosis

Thermally-induced tissue damage is a function of both instantaneous temperature and thermal history. Reviews of methods used for quantifying tissue damage due to hyperthermia

exist in the literature [88-90]. The Arrhenius damage integral can be used to estimate the degree of damage to cells in tissue experiencing hyperthermia:

$$\alpha = \int_0^t A exp\left(-\frac{E_a}{RT(t)}\right) dt \qquad \text{Eq. II.10}$$

where α is the degree of damage at a given time, A [1/s] is a frequency factor, E_a [J/mol] is the activation energy required to damage tissue, R [J/mol·K] is the universal gas constant, and T(t) [K] is the temperature history of the tissue. Values of E_a have been experimentally measured for various tissues [89]. The fraction of damaged tissue can then be determined by:

$$\theta_d = 1 - e^{-\alpha} \qquad \text{Eq. II.11}$$

In current models, critical temperature isotherms (55-60°C) are often used in lieu of Eq. II.10-11 as these contours often correspond with the visible treatment zone. Incorporation of more advanced tissue damage models, such as the Arrhenius damage integral, can further improve predictive modeling efficacy.

II.3.2 Current Ablation Modeling Research

The following section discusses computational models of MWA of varying complexities. The simplest model of MWA derives tissue temperature directly from a steady state solution to electromagnetic energy deposition by neglecting transient material properties and thermal contributions from metabolism, conduction, and perfusion in Eq. II.7 as follows:

$$Q = \rho c \frac{\partial T}{\partial t} \qquad \text{Eq. II.12}$$

With this method, a steady-state solver is used to solve the electromagnetic problem and determine energy deposition (often precomputed for a generic geometry as SAR) and resistive heating in tissue, Q, from which determining the temperature is straightforward.

The deposition of electromagnetic energy has been reported to be the major contributor to heat transfer in thermal ablation techniques. This method is attractive for situations which require a fast solution (i.e. when a first-order approximation is appropriate). SAR models are often used during optimization and validation of thermal ablation antenna in *ex vivo* tissue [67-71, 91-92].

More complex models of MWA incorporate thermal conduction and blood perfusion in the bioheat equation (Eq. II.7), which has been shown to have a large impact on ablation zone extent [81-83]. The simplest implementations of this method assume that tissue material properties remain at steady-state throughout simulation [93-95]. By holding tissue properties constant, these models are only coupled in one dimension. Therefore, as before, the electromagnetic problem is solved once to establish the electric field and is not required to be updated. Consequently, temperatures obtained from these models are unrealistically large in comparison to experimentally recorded temperatures since tissue properties have been found to change as a function of temperature (e.g. which lead to a dynamically changing electric field *in vivo*) [79-80]. Although predicted temperatures are large, the geometric extent of predicted ablation zones correlate with ablation zones observed in *ex vivo* procedures which is likely due to variability in the methods used to predict tissue necrosis. As tissue water content decreases from evaporation at higher temperatures, the tissue becomes less lossy. Therefore, microwave penetration depth is increased and less energy is absorbed near the antenna. While these models do address perfusion and large-vessel conduction, further work involving *in vivo* studies is certainly needed for accurate model development.

Going further, sensitivity studies have highlighted the extensive influence that tissue properties have on computational MWA models [77-78]. More comprehensive models of

ablation have been presented which incorporate dynamic changes in tissue properties based on instantaneous temperature [74-76, 96-97] or tissue water content [92, 96]. Ji and Brace created temperature-dependent models of dielectric properties after measuring experimental values of *ex vivo* bovine tissue undergoing 2.45 GHz MWA. These empirically-derived temperature-dependent property models showed improvement when deployed within a computational model of MWA and compared to existing linear and static property models [75]. Deshazer et al. observed similar improvement in a comparable *ex vivo* study performed at 915 MHz but concluded that further investigation is needed to effectively model dielectric properties in this dynamic environment [74]. Liu and Brace then expanded on the previous work of [75] by adding in a tissue thermal mechanics component to account for tissue shrinkage that occurs with protein denaturing [76]. Yang et al. presented a model which incorporated dynamic changes in tissue properties from empirical formulae based on water content [92]. Their model presents a function to compute water content from instantaneous temperature and provides good correlation with experimentally measured temperatures and ablation zone extent. Cavagnaro et al. compared tissue property models based on instantaneous temperature and tissue water content and found that temperature-dependent property models should be utilized for high power ablations [96].

II.3.3 Hepatic Tissue Properties

Other groups have reported the sensitivity of MWA model results to material property values. Studies at both clinical frequencies of ablation have attempted to model tissue properties from experimental measurements. The following section discusses material property values, their dynamic nature, and property models that have been applied within the literature.

Dielectric material properties (i.e. relative permittivity and electrical conductivity) of normal and cancerous hepatic tissues have been reported in the literature. Stauffer et al. reported dielectric properties of HCC, mCRC, and normal hepatic tissue excised from human subjects – finding that relative permittivity and conductivity in tumors were 12% and 24% higher than in normal tissue respectively [85]. O'Rourke et al. measured dielectric properties of healthy and malignant human liver tissue, both *ex vivo* and *in vivo*. Their results agree with [85] indicating that dielectric properties are higher in malignant tissue when measured *ex vivo* [98]. However, *in vivo* measurements showed no significant differences in dielectric properties. Tissue dielectric properties are also temperature dependent due to protein and water content. Proteins in tissue denature at temperatures above 60°C causing irreversible changes to dielectric properties. Dielectric property changes as a function of temperature have been measured for temperatures below 60°C [99-100]. Relative permittivity decreases with temperature: -0.2/°C and -0.1/°C at 915 MHz and 2.45 GHz respectively [99-100]. Electrical conductivity increases with temperature: 1.33/°C and 0.4/°C at 915 MHz and 2.45 GHz respectively [99-100]. Brace reported measurements of dielectric properties taken during RF ablation of *ex vivo* tissue that showed a sharp decline (~50%) at temperatures nearing 100°C – likely due to water vaporization [80]. At higher temperatures, which are regularly reached during thermal ablation, it is difficult to isolate the cause of changes to dielectric properties. Changes in dielectric properties have also been reported as a function of tissue water content [101]. Hepatic tissue becomes less lossy as water evaporates, resulting in greater microwave penetration and lower SAR.

Thermal material properties (i.e. blood perfusion rate, density, specific heat capacity, and thermal conductivity) have been measured and reported in the literature. Tissue density is assumed to be constant with temperature. However, for procedures where the temperature

exceeds 100°C tissue density may be adjusted to account for water vaporization and tissue desiccation [99]. Specific heat capacity for various tissues has been reported [99]. Haemmerich et al. measured specific heat of bovine liver as a function of temperature up to 85°C and found it to increase by up to 18% at high temperature [102-103]. Thermal conductivity has been measured as a function of temperature in *ex vivo* bovine liver and increased slightly with temperature at a rate of 0.00033/°C [104]. Changes to thermal conductivity at higher temperatures have not been presented.

From Eq. II.8, heat loss by blood perfusion is proportional to the difference between inflow blood temperature and tissue temperature. Many models in the literature consider blood perfusion constant up until 60°C above which perfusion is assumed to cease due to collagen shrinkage in capillary walls. Schutt and Haemmerich showed that in hepatic RFA the choice of blood perfusion model substantially impacts the model-predicted ablation zone geometry [81]. Furthermore, differences in vasculature of tumor and healthy tissue likely introduce differences in blood perfusion. The Pennes bioheat equation (Eq. II.7) does not account for heat loss due to blood flow in large vasculature, i.e. the "heat sink effect". Thermal ablations performed near these vessels are susceptible to heat transfer due to bulk blood flow. At this point in the literature, computational models of MWA have generally been investigated within phantom or *ex vivo* tissue and have neglected to account for tissue perfusion.

II.3.4 Preoperative Planning Methods

Preoperative planning techniques for MWA may be used to facilitate the selection of risk-averse optimal antenna placements and trajectories by the physician. Zhai et al. (2008) presented a preoperative planning method for percutaneous MWA [72] which

allows for surgeons to iteratively adjust antenna position and trajectory within a 3D visualization of patient anatomy rendered from preoperative imaging. At each iteration, the SAR profile is solved with an analytical approximation based on input power parameters [105]. Temperature and cell death are then approximated directly from the SAR profile. The resulting necrotic field is then reconstructed within the 3D visualization, resulting in a manual determination of antenna placement. During the MWA procedure, the physician is provided with trajectory angle, puncture location on the skin, and penetration depth of the antenna to achieve the planned ablation. However, validation was limited. Results of the preoperative ablation prediction were manually registered to the postoperative follow-up CT and compared - providing no inclination of incurred registration error.

Liu et al. (2013) presented an intraoperative planning method for hepatic MWA based on EM-tracked iUS and ablation antenna [106]. During the procedure, the physician selects 4 anatomical landmarks from the 3D iUS imaging and then manually selects the corresponding locations from the preoperative CT to determine an image-to-physical registration. The plan for MWA antenna placement is then optimized such that: (1) the entire tumor and margin are covered by the necrotic zone, (2) the number of required ablations is minimized, (3) the number of insertions is minimized, and (4) critical structures are avoided. The predicted ablation zone is assumed to be ellipsoidal with major and minor axes defined by experimental observations [107-108]. Results presented a statistically higher success rate compared to procedures targeted only with 2D iUS.

Berber (2015) presented patient outcomes following laparoscopic MWA using the Covidien Emprint Ablation System and planning application (Medtronic, Minneapolis, MN, USA) [109]. Patient preoperative CT images are loaded into the planning software and target lesions are manually labeled within a 4-panel multiplane view. An ablation zone label is then

automatically generated which encompasses the target lesion and a safety margin – given desired input power, tissue type, and procedural time. The elliptical contours defining the ablation zone may be adjusted manually, in which case procedural time adjusts accordingly. The relationship between ablation zone size, power, and time in a given tissue type are empirically predetermined. Additionally, the physician may adjust the MWA antenna between a set of trajectories which would provide the same ablation zone outcome – which in the case of the Covidien Emprint Ablation System is assumed to be purely spherical. No additional guidance is provided to further enhance MWA delivery.

II.4 Summary

Improved procedural efficacy and therapeutic outcomes have been presented from studies investigating preoperative planning and advanced navigational methods for MWA. Herein, we will advance current IGLS methods and show that soft-tissue deformation correction can be applied to image-guided MWA procedures to improve the accuracy and efficiency of intraoperative localization of internal anatomy and probe placement when compared to rigid registration methods. In addition, we will present a method for computational modeling of MWA which assumes patient-specific material properties from *a priori* quantitative medical imaging. This method will allow for more accurate predictive modeling of clinical MWA procedures by accounting for variation in material properties between patients. Furthermore, we present an initial study in which a retrospective computational model of MWA is integrated within the surgical navigation framework to evaluate the combined errors associated with localization and modeling. Moving forward, while providing anatomical localization is the principal feature of the applied navigational methods, it is equally interesting to extend biophysical modeling methods, such as predictive

MWA modeling, into the image-guidance domain.

Chapter III

Methodology

The methods presented in the following sections describe the common supportive methods and techniques used throughout the aims of this project. In overview, these sections detail the protocols used to collect clinical IGLS data, the hardware and software required to create various phantom datasets, and the registration methods used to provide image-to-physical alignment.

III.1 Patient Data Collection

III.1.1 Patient Geometric Model Construction

Preoperative patient image data for hepatic surgical navigation procedures typically consists of contrast-enhanced CT or MRI images from which relevant anatomical structures can be identified. Within this dissertation, segmentation of image-data (for both patient and phantom data) was performed using ITK-SNAP [110] which allows for both manual and semi-automated segmentation. During segmentation, the location of anatomical features of interest (e.g. artificial fiducial markers, the liver surface, tumors, and vasculature) can be identified. The segmentation process results in the generation of a binary mask of the particular anatomical feature (e.g. the bounding liver surface) which can then be used to generate a 3D surface using an implementation of the marching cubes algorithm [111] in the Visualization Toolkit (VTK) [112]. The surface is then smoothed with a radial basis function implemented by the FastRBF Toolbox (Farfield Technologies, Christchurch, New England) and input into a custom mesh generator (SPMESH) to create a mesh of tetrahedral elements with approximately 4 mm spacing [113]. Figure IV.2 presents an example segmented and

meshed patient liver before (red) and after (blue) the application of deformation.

This meshed, preoperative patient geometric model is designed to predict how tissue deforms when subjected to appropriate boundary conditions representing the intraoperative organ state. The model assumes that the liver is an isotropic solid described by the 3D Navier-Cauchy equation:

$$\nabla\left(\frac{E}{2(1+v)(1-2v)}\nabla\cdot u\right)+\left(\frac{E}{2(1+v)}\nabla^2 u\right)+\mathrm{F}=0 \qquad \text{Eq. III.1}$$

where E is Young's modulus, v is Poisson's ratio, u is the displacement vector, and F is the distribution of applied body forces. The Galerkin weighted residual method is applied using linear Lagrange basis functions on the tetrahedral geometric mesh to make solvable the linear system of partial differential equations:

$$[K]\{d\}=\{f\} \qquad \text{Eq. III.2}$$

where K is a *3n x 3n* global stiffness matrix, d is the vector of nodal displacements, and f is the vector containing boundary conditions and body force contributions. Equation III.2 can then be solved to resolve the unknown nodal displacements.

III.1.2 Intraoperative Tracking and Digitization

In this dissertation, an NDI Polaris Spectra (Northern Digital, Waterloo, ON, Canada) camera system in conjunction with an OR cart system running either NDI Track (Northern Digital, Waterloo, ON, Canada) or Explorer™ Liver (Analogic Corporation, Peabody, MA) localization software were used to localize instrumentation in physical space with a high degree of accuracy (<0.5 mm [114]). The passive dual-camera system detects the location of geometric patterns of hyper-reflective spheres by emitting infrared light and detecting the reflections, from which the 3D location is triangulated. As such, the system requires unobstructed line of sight between tools and the camera. Different patterns of spheres can be

attached to different tools, allowing several tools to be identified and tracked simultaneously. The Polaris Spectra, a tracked manual stylus, and tracked ultrasound probe are presented in Figure III.1.

Figure III.1. Example setup of image-guidance hardware. (Left) A Polaris Spectra camera system and OR cart. (Right, top) A passively tracked manual-stylus used for surface data collection and organ interrogation. (Right, bottom) A passively tracked ultrasound probe.

During surgery, following organ mobilization, the physician can utilize the tracked stylus to manually digitize the organ surface and particular salient anatomical features (e.g. the left and right inferior ridges and the attachment of the falciform ligament). This digitization creates a sparse 3D point cloud representing the spatial location of the organ surface and features within the OR which can then be used to drive image-to-physical registration methods. Example intraoperative sparse surface digitizations are presented in Figure IV.5.A with reference to the preoperative organ model.

III.2 Phantom Data Generation

Various phantom models were used throughout each of the aims of this dissertation for both image-to-physical registration and MWA model validation. In Chapter IV, a polyvinyl alcohol (PVA) hepatic phantom was used to replicate the elastic properties of tissue to validate image-to-physical registration methods. In Chapters V-VI, an agar-albumin phantom was used to provide a permanent thermal history following microwave ablation within the phantom.

PVA phantom data were acquired consistent with the previously reported study by Rucker [60] and in the dissertation of Pheiffer [115]. The creation of a deformable hepatic PVA phantom begins by combining 7% w/v suspension of hydrolized PVA powder (Flinn Scientific, Batavia, IL) with cold water and heating to 80°C. After heating, 10% w/v glycerol (Fisher Scientific, Pittsburgh, PA) is added until the mixture is clear and achieves a low viscosity. Next, the container is tightly sealed to reduce dehydration and the gel is cooled to room temperature while being thoroughly mixed on a magnetic stir plate. Polymerization of the cryogel phantom is achieved by subjecting the mixture to a series of freeze-thaw cycles where the cryogel is cooled to -37°C over a 12-hour period and then gradually returned to

room temperature over the next 12 hours. The phantom utilized within Chapter IV was given a hepatic shape by pouring the cryogel into a liver-shaped mold prior before the freeze-thaw cycle. Additionally, 47 internal plastic beads were incorporated into the phantom prior to the freeze-thaw cycle to serve as ground truth registration targets. The phantom was imaged with CT in various arrangements, providing the outer boundary of the phantom surface and the coordinate of each internal target.

The creation of an ablation phantom begins by combining 1.5 wt% agar-agar powder (Thermo Fischer Scientific, Waltham, MA) with purified water and gradually heating while being continuously stirred on a hot plate until boiling. After the gel has exceeded 60°C, vegetable shortening (Crisco, The J.M. Smucker Company, Orrville, OH) can be introduced to achieve a desired fat content. The solution is then cooled below 55°C with continuous stirring before adding 50 wt% liquid egg white (Break Free Liquid Egg Whites, The Kroger Company, Cincinnati, OH) and stirring for 1 minute. The phantom utilized within Chapter V was given a hepatic shape by pouring the agar gel into a liver-shaped mold, while the phantoms utilized within Chapter VI were set within a 1L cube. Following ablation, the phantom can be imaged with T_2-weighted MRI to acquire the 3D extent of the ablation lesion. Additionally, the phantom can be sectioned along the centerline of the ablation antenna to provide a mock-histology view of the ablation lesion.

III.3 Image-to-Physical Registration

Two methods of image-to-physical registration were heavily utilized throughout this work: a conventional rigid registration method and a nonrigid registration approach which corrects for deformation. Rigid registration methods are currently the standard method used in commercial navigation systems. It is an essential OR requirement that these methods are

fast, however they rely on the assumption that the transformation from image to physical space is completely rigid. Therefore, these methods can behave poorly when used in the presence soft-tissue deformation. The rigid registration approach used throughout this work was initially presented by Clements [42] and is presented in Figure III.2. This salient-feature weighted iterative closest point registration utilizes homologous anatomical features to bias point correspondence estimation within an iterative closest point registration. This biased weighting scheme preferentially favors alignment of preoperatively designated anatomical features with corresponding intraoperatively designated features. This algorithm provides a coordinate transformation that minimizes the residual error between the preoperative and intraoperative organ surface data and is evaluated within Chapters IV and V of this work.

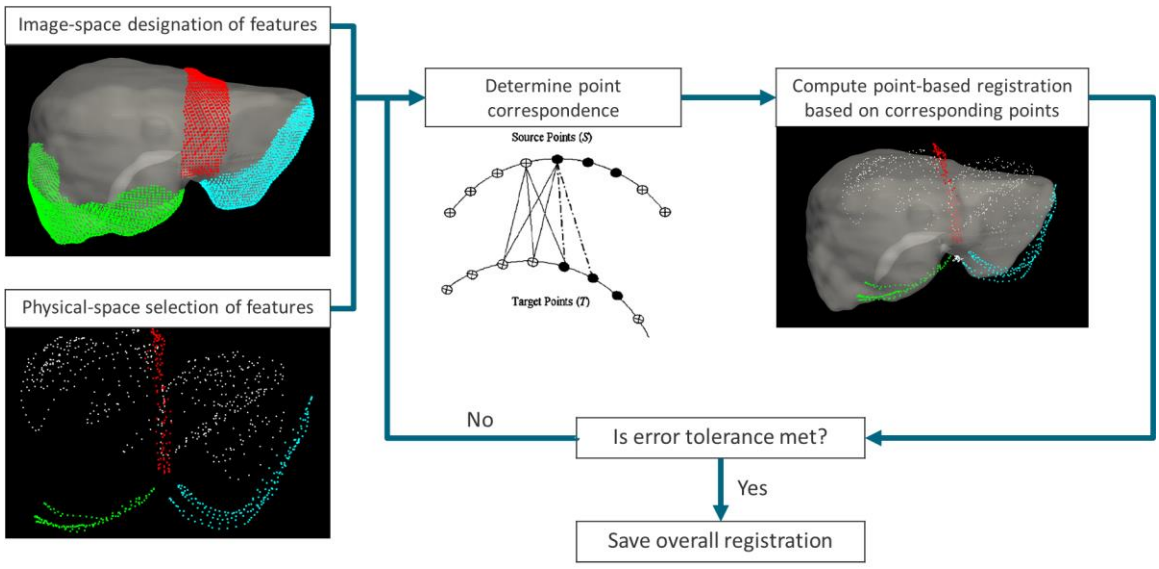

Figure III.2. Flowchart detailing the salient-feature weighted iterative closest point rigid registration algorithm of Clements [42]. First, features are identified from the preoperative image and digitized from the intraoperative organ surface. Next, closest points are determined for each point in physical space to the corresponding image data. A point-based registration is then performed. New closest points are determined and point-based registrations performed until the error tolerance is met.

To better account for intraoperative soft-tissue deformations, a nonrigid, model-based approach first described by Rucker [60] was utilized in Chapters IV and V of this work. This deformable registration applies the previously described patient geometric organ model within an inverse approach to rapidly minimize the difference between the model surface and the intraoperative surface data. The original method by Rucker [60] defines a posterior polynomial displacement field which provides a precomputed distribution of volumetric displacements to the biomechanical model. In the OR, an optimization is utilized to actively reconstruct these boundary conditions along with simultaneous updates to the physical space transformation until the shape of the preoperative organ surface matches the intraoperative counterpart. A modification to this method which introduced tangential components to the polynomial displacement field is presented in Chapter IV of this work. A further modification which reformulates the application of boundary conditions to a control point strategy [61], rather than a polynomial surface, is presented in Chapter V.

Chapter IV

Normalizing Sparse Surface Data for Image-to-Physical Registration

IV.1 Summary and Contributions

In this chapter, a novel method (i.e. a human-to-phantom data framework) was introduced that allows for the development and testing of image-to-physical registration algorithms in the presence of deformation with internal targets for quantifying error and representing realistic clinical data acquisition. Furthermore, this chapter presents a surface data resampling method which was verified within this human-to-phantom data framework and was found to significantly improve registration accuracy. The work herein was motivated by an observation of variability in the extent, uniformity, and the degree of noise associated with a series of clinical sparse liver surface digitizations acquired during IGLS procedures in a separate study [62]. The overall intent of this chapter was to investigate the degree to which such variation in operative sparse surface data collection influences the application of existing surface-based rigid registration [42] and deformation correction [60] methods for IGLS.

In this human-to-phantom data framework, clinically acquired sparse organ surface digitizations collected from patients enrolled in an ongoing study at Memorial Sloan Kettering Cancer Center (MSKCC) were affinely transformed and applied as collection patterns to the surface of a well-characterized deformable hepatic phantom. These clinically acquired data provide a realistic pattern and distribution of surface data that is not otherwise attainable outside of the OR. The deformable hepatic phantom provides pristine image data, including quantifiable internal targets, in both a "preoperative" undeformed state and an "intraoperative" deformed state. Thus, image-to-physical registration can be simulated by

registering the "preoperative" phantom image-data to the clinical surface data which has been applied to the "intraoperative" phantom surface. The accuracy of these registrations can then be quantified from the registration-predicted and ground-truth internal target locations. Furthermore, this framework allows for a large population of clinically-relevant registration scenarios to be rapidly created by applying various clinical collection patterns and simulated digitization noise to the "intraoperative" phantom surface. In summary, this human-to-phantom data framework provides a significant advancement towards the rapid, early stage verification of image-to-physical registration methods for IGLS by providing a wealth of clinically-relevant data in a fully characterized phantom environment, avoiding the burden that would be required to collection such comprehensive data clinically.

Furthermore, the surface data resampling method established in this chapter serves to normalize surface data quality across different cases and physicians. In this work, its application is shown to improve the accuracy and reproducibility of the investigated IGLS registration approaches. In brief, the method works by fitting an approximated surface to intraoperative surface digitizations using the method of [116] and then produces a more uniform sampling of the underlying organ surface. Overall, the results of using this method in the human-to-phantom data framework were very encouraging and it has since been applied in a clinical perception study [64].

IV.2 Improving registration robustness for image-guided liver surgery in a novel human-to-phantom data framework

The work in this chapter is reprinted, with permission, from:

J.A. Collins, J.A. Weis, J.S. Heiselman, L.W. Clements, A.L. Simpson, W.R. Jarnagin, and M.I. Miga, "Improving registration robustness for image-guided liver surgery in a novel human to phantom data framework," *IEEE T Med Imaging*, vol. 36, no. 7, pp. 1502-1510, 2017.

Abstract

In open image-guided liver surgery (IGLS), a sparse representation of the intraoperative organ surface can be acquired to drive image-to-physical registration. We hypothesize that uncharacterized error induced by variation in the collection patterns of organ surface data limits the accuracy and robustness of IGLS registration. Clinical validation of such registration methods is challenged due to the difficulty in obtaining data representative of the true state of organ deformation. We propose a novel human-to-phantom validation framework that transforms surface collection patterns from *in vivo* IGLS procedures (n=13) onto a well-characterized hepatic deformation phantom for the purpose of validating surface-driven, volumetric nonrigid registration methods. An important feature of the approach is that it centers on combining workflow-realistic data acquisition and surgical deformations that are appropriate in behavior and magnitude. Using the approach, we investigate volumetric target registration error (TRE) with both current rigid IGLS and our improved nonrigid registration methods. Additionally, we introduce a spatial data resampling approach to mitigate the workflow-sensitive sampling problem. Using our human-to-phantom approach, TRE after routine rigid registration was 10.9 ± 0.6 mm with a

signed closest point distance associated with residual surface fit in the range of ± 10.0 mm, highly representative of open liver resections. After applying our novel resampling strategy and improved deformation correction method, TRE was reduced by 51%, i.e. a TRE of 5.3 ± 0.5 mm. The work reported herein realizes a novel tractable approach for the validation of image-to-physical registration methods and demonstrates promising results for our correction method.

IV.2.1 Introduction

Image-guided liver surgery (IGLS) aims to improve surgical precision by providing intraoperative guidance of instrumentation. True IGLS requires (1) full volumetric preoperative imaging, (2) the ability to localize instrumentation in physical space, (3) a method of image-to-physical space registration, (4) a method to correct for intra-procedural organ changes, and (5) a display of instrumentation position in accordance to preoperative imaging. A problem central to IGLS is the task of registration in the soft-tissue environment; where organ shape changes that occur between preoperative imaging and intraoperative presentation create significant challenges to the guidance environment. The overall utility of IGLS methods fundamentally hinges on the accuracy of the image-to-physical space mapping. In addition, and not often discussed, there is a fundamental challenge that consists of acquiring sufficient extent and quality of geometric data such that guidance updates are accurate while not compromising the workflow of procedural care. IGLS embodies this demanding and often vexing problem.

In IGLS workflow (for both open and laparoscopic indications), the anterior surface of the organ and some salient features are routinely available (i.e. falciform ligament and inferior ridges [62, 117]). Digitization technologies for acquiring these surfaces are still

somewhat limited [118]. Tracked ultrasound imaging is commonly used and allows for major vasculature to be digitized during surgery [119]. Both surface and ultrasound registration approaches are being pursued for commercial IGLS purposes. Surface-based registration techniques typically rely on an iterative approach with an estimated surface correspondence and assume that surfaces being registered share a high degree of similarity [39-42]. When considering ultrasound-based approaches, these typically rely on local alignments between CT-rendered and ultrasound-identified vasculature. With each of these approaches, of course, alignments can be compromised by deformations from pre-to-intraoperative organ shape changes, respiration, liver mobilization, and resection [120-122]. In recognition of this, ongoing efforts have been made towards soft-tissue deformation correction in IGLS using these modalities of geometric data. For example, in [123] an elastic registration technique is used in combination with ultrasound vasculature data to nonrigidly correct for deformations. In our work, we have concentrated on approaches that minimize differences between surfaces extracted from the preoperative imaging and those gathered intraoperatively. Our approaches use patient-specific biomechanical models to nonrigidly align the data [42, 60, and 62] (adding very sparse subsurface data, i.e. tumor centroid location in [60], has also been pursued).

When considering sparse surface data digitization for IGLS, registration has been performed using manual swabbing with a tracked probe [124], laser-range scanning [40], ultrasound [62, 125-126], time of flight imaging [127], stereoscopic imaging [128-129], and conoscopic holographic surface scanning [130]. Recently, we did a comprehensive study comparing registration results using swabbing, laser range scanning, and conoscopic holographic scanning in [131]. While results indicated better performance from non-contact digitization methods, challenges of integration into the operating room still persist which is

why manual surface swabbing is still the only commercial IGLS surface-based approach in use today.

Regardless of the sparse-data source, data collection is commonly contingent on the surgeon's ability to acquire data within a surgical procedure. As a result, variability in density, uniformity, extent, and degree of noise (either from the modality of measurement or physician technique) all affect registration but have received limited study. This is largely due to the extreme challenge of needing extensive bystander acquisition capabilities to assess and record data within the operating room. Going further, the resources for validation precipitate an even more excessive clinical burden, i.e. intraoperative volumetric imaging and a series of consenting patients. The encumbrance of intraoperative volumetric validation, either with partial volume methods such as tracked intraoperative ultrasound [62] or full volumetric imaging methods such as computed tomography or magnetic resonance imaging [37, 125], is considerable and adds impetus for a new way to characterize methods rapidly. Therefore, we present a novel human-to-phantom validation framework which aims to bypass the burden of such cumbersome clinical data acquisition.

In the work presented herein, routine intraoperative patient data associated with conventional IGLS were collected to study the influence of variability in organ surface acquisition. This study has been motivated by the observation of a high degree of variation in the spatial pattern and density of surface data in a series of intraoperative procedural acquisitions (Fig. IV.1). The aim of this study was to characterize the influence that these variations have on IGLS accuracy using both conventional rigid and our improved nonrigid registration methods. While we report on the characterization of our particular approach, the framework described herein has broader impact by demonstrating how clinical workflow

data can be combined with a realistic phantom for rapid methodological prototyping.

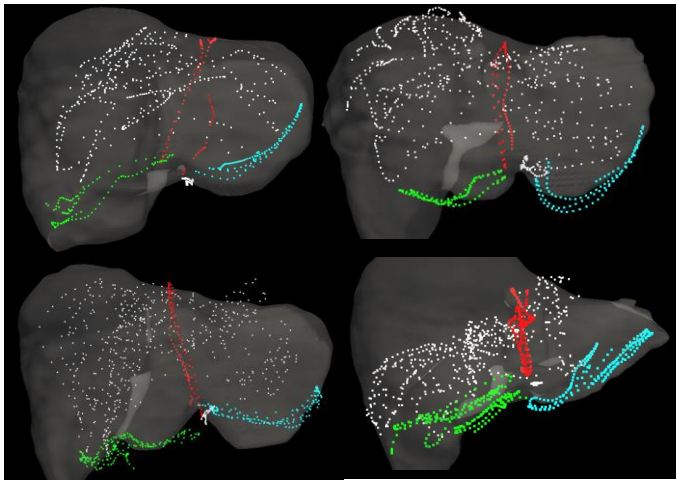

Fig. IV.1. Manual surface swabbing results collected within the Explorer™ Liver navigation system. Digitized surface and feature data are presented for 4 clinical cases following an initial rigid alignment generated by the salient feature registration algorithm of Clements et al. [42]. Data representing the falciform, left inferior ridge, right inferior ridge, and anterior organ surface are presented in red, blue, green, and white respectively. (© 2017 IEEE)

Briefly described, in the human-to-phantom validation framework, the surface collection patterns of a series of clinical surface data were individually transformed and applied to a well-characterized hepatic deformation phantom designed to have deformations similar to the OR. This allows the replication of multiple independent surface collections while facilitating the measurement of full volumetric shift with CT imaging and distributed CT-visible targets, thus providing ground truth data for accuracy and reproducibility assessment. Such complete and discrete ground-truth data is typically unavailable in clinical data and has become a major obstacle in the quantitative assessment of registration accuracy. In addition, we use the novel framework to assist in designing a spatial data resampling

strategy that demonstrates dramatic improvements in both rigid and nonrigid registration results. We conclude by discussing the methods and results of our study to understand the influence of data collection on registration accuracy in IGLS.

IV.2.2 Methodology

IV.2.2.1 Overview of Experimental Design

The methods of this study are designed to accomplish three goals: first, create a novel human-to-phantom data framework for extensive use in IGLS methodological validation; second, develop a resampling approach which improves the accuracy and variance of IGLS registration methods; third, perform an analysis to systematically study the impact that variations in organ surface data quality have on IGLS registration methods.

IV.2.2.2 Patient Data Collection

Patients were consented and enrolled in an ongoing prospective study of deformation correction for IGLS approved by the Memorial Sloan Kettering Cancer Center (MSKCC) Institutional Review Board. Thirteen patients undergoing open liver resection at MSKCC are presented within this study. Prior to surgery, contrast enhanced CT images were acquired of each patient as part of routine clinical management. 3D anatomical models of the liver, tumors, and vasculature were generated using surgical planning software (Scout™ Liver, Analogic Corporation, Peabody, MA). Following this processing, the preoperative 3D model was loaded into a surgical navigation system (Explorer™ Liver, Analogic Corporation, Peabody, MA). During surgery, after organ mobilization, the surgeon manually swabbed anatomical surfaces with an optically tracked stylus. This digitization creates a sparse 3D point cloud representing the organ surface and salient anatomical features. A

visualization of intraoperative surface collection is presented in Fig. IV.1.

IV.2.2.3 Phantom Data Collection

Phantom data were acquired consistent with a previously reported study by Rucker et al. [60]. Briefly, a compliant hepatic phantom was created to mimic clinical organ deformation based on our experience in a previously reported 75 patient multi-center clinical trial [59]. The phantom consisted of water, 7% by volume polyvinyl alcohol, and 10% by volume glycerin that was subjected to a 12-hour freeze-thaw cycle to develop stiffness [132]. The phantom incorporated 47 subsurface plastic beads, which served as ground truth target locations. Similarly to clinical cases, a preoperative CT scan of the phantom in an undeformed state was acquired to generate an organ model and to identify target locations. Intraoperative organ deformation was replicated by altering support at the posterior phantom surface (Fig. IV.2). An intraoperative CT scan of the deformed phantom was captured to acquire the true deformed organ surface, volume, and target locations. Salient anatomical feature regions (falciform ligament and inferior ridges) were designated from the intraoperative CT.

IV.2.2.4 Human-to-Phantom Data Preparation

Thirteen clinically acquired surface datasets (II.B) were applied as collection patterns to the hepatic deformation phantom (II.C) to observe the effect of intraoperative organ surface digitization on registration accuracy. Furthermore, randomized sinusoidal noise was applied to these collection patterns to simulate the natural periodic level of contact that occurs during manual organ swabbing (i.e. compressing into or lifting off the surface) – resulting in easily generated, unique, and realistic digitizations of the intraoperative phantom

surface.

The clinical surface data were aligned to the intraoperative phantom data using rigid salient feature weighted registration [42]. This registration aligned the phantom and clinical data according to the salient features, but differences in organ size and extent remained. We should also note that others are also following this approach [133]. Following initial rigid alignment, the finite iterative closest point registration method by Kroon [134] incorporated scale and skew into the optimization of a transformation matrix, providing an affine registration which accounts for differences in data extent and organ size. Following alignment and scaling of the clinical and phantom intraoperative surfaces, the clinical surface data were projected to their closest point on the intraoperative phantom CT, producing thirteen clinically representative surface digitizations of the CT documented deformed phantom surface.

Fig. IV.2. The CT segmented preoperative and intraoperative phantom surfaces are presented in red and blue respectively. The differences in surfaces highlights the volumetric deformation undergone in the simulated phantom data. (© 2017 IEEE)

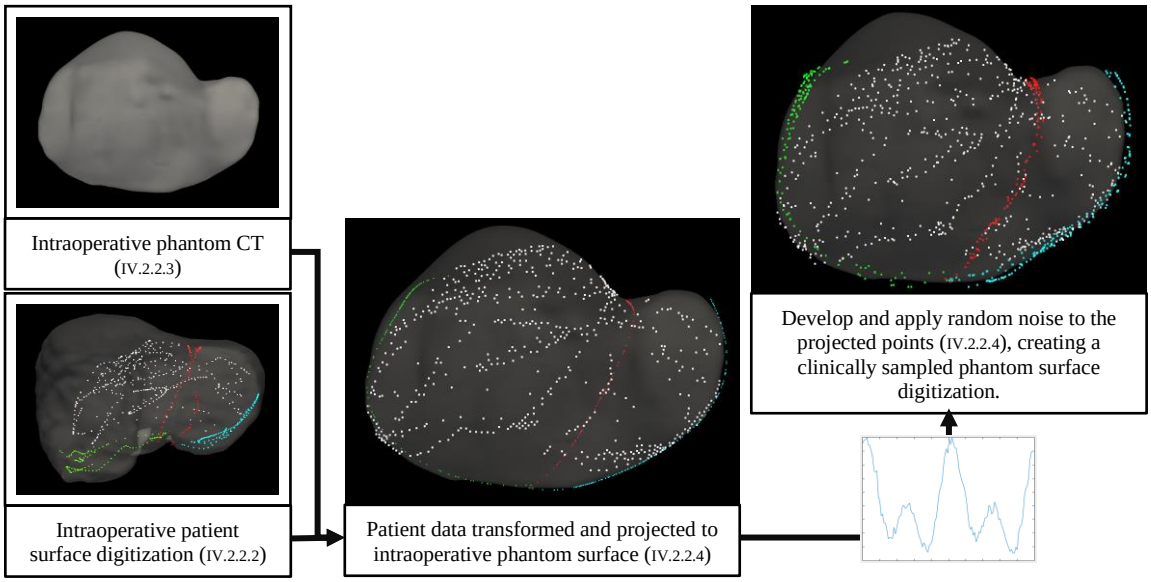

Fig. IV.3. Structure of the proposed human-to-phantom data set presented in flowchart form. Human data is aligned, scaled, and projected onto the intraoperative phantom CT surface. Randomly defined sinusoidal waveforms are generated and applied to the projected data to simulate collection noise. Noise patterns are applied independently to the surface and feature data. The right and center columns serve as examples of surface digitization with and without applied noise. (© 2017 IEEE)

Next, realistic noise was added to the phantom collections along the spatial trajectory associated with the particular clinical swab. To accomplish this, randomized sinusoidal waveforms were generated for each simulated phantom surface and feature designation (Fig. IV.3). Independent noise was applied in the normal and tangential directions for each data point as follows:

$$\widehat{N} = (\sin(2\pi s f_1 + \varphi_1) + \mathrm{a} \cdot \sin(2\pi s f_2 + \varphi_2) + R) * \hat{d} \qquad \text{Eq. IV.1}$$

where $\widehat{N}$ is the vector of applied noise, $\hat{d}$ defines the normal or tangential directions at each data point, f_i is a randomly assigned low frequency (between 0-10 Hz in qualitative accordance with clinical swabbing), φ_i is a randomly assigned phase shift (between 0-2π), a is a randomly assigned amplitude (between 0-5), and R is uniform pseudorandom noise. Applying smoothly varying noise in the spatial order of clinical collections mimicked the pattern of noise associated with intraoperative data collection. The amplitude of noise was established by curve fitting each clinical data swab and averaging the residual error in the directions normal and tangential to the organ surface. The RMS amplitudes of noise in the normal (0.9 mm) and tangential (1.8 mm) directions were specified by the average noise measured across the whole clinical data set. Each application of random noise to a clinical surface data pattern results in an independent simulated surface digitization of the intraoperative phantom. To ensure adequate characterization, we used this strategy to simulate 50 phantom surface data acquisitions with independent randomized noise added for each of the 13 clinical cases (Fig. IV.4). With the above process realized, any organ surface data pattern taken intraoperatively could be transformed with noise onto our 3D deformation phantom system, thus allowing for a quantitative assessment of its impact on *any* proposed registration scheme in the presence of realistic deformations.

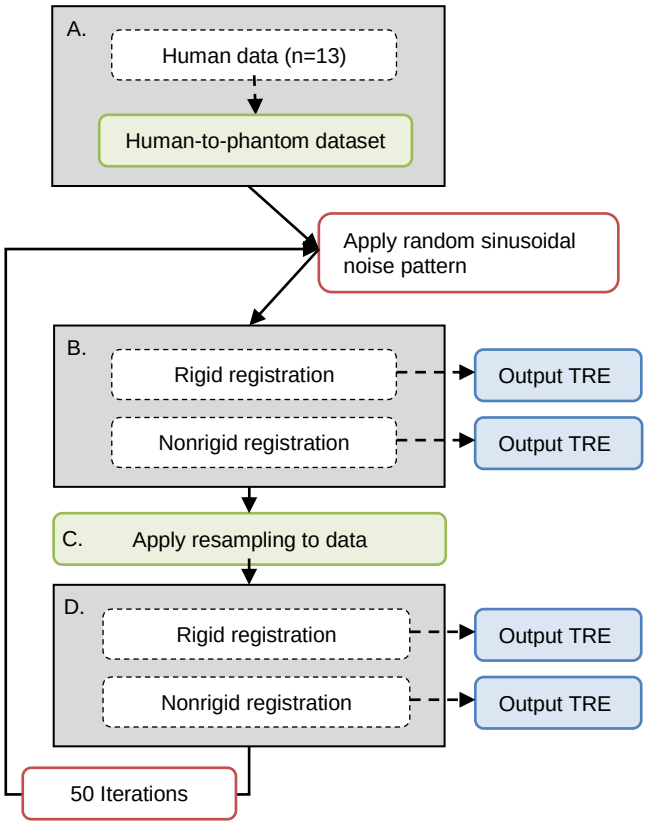

Fig. IV.4. Schematic of the proposed study. For a given clinical case (n=13), surface data is aligned, scaled, and projected onto the intraoperative phantom CT surface with a randomly determined noise pattern (A). Our rigid and nonrigid registration methods are applied, while quantifying subsurface TRE (B). The simulated surface is then resampled (C) and registrations are recalculated (D). This process is repeated with 50 different applications of noise per clinical case – creating 50 independent surface acquisitions for each of the (n=13) clinical organ surface digitization patterns. (© 2017 IEEE)

IV.2.2.5 Surface Data Resampling

In our experience with OR-amenable IGLS processes, surface data collection varies with real-world surgeon use. To improve robustness in light of this variability, we propose a resampling approach and test its impact using our novel human-to-phantom framework. To begin, we assume that the anterior organ surface, where the sparse surface data were collected, may be treated as a bounded, continuous, and unique surface of the form:

$$z = f(x, y) \quad \text{Eq. IV.2}$$

This assumption reduces dimensionality, thus decreasing complexity and computational burden. To improve consistency regardless of initial raw data orientation in Cartesian space, a 3D least squares plane was fit to the raw data and a rigid registration was determined which transforms the least squares plane to the $x - y$ plane by aligning its normal to the z axis. A discrete grid was fit to the transformed raw data using a joint interpolation and approximation method [116]. The approach fits locally to the transformed raw data using barycentric interpolation as follows:

$$f(x, y) = \sum_{i=1}^{3} \lambda_i f(x_i, y_i) \quad \text{Eq. IV.3}$$

where the height at a location within the triangular grid, $f(x, y)$, is reconstructed as a linear combination of the heights at the vertices of an encompassing triangle, $f(x_i, y_i)$, weighted by the ratio of area within the triangle, λ_i, where each vertex contributes to the queried location. The approach then regularizes the grid with a discrete approximation of the Laplacian using the finite difference method for a given grid node as follows:

$$\nabla^2 f(x, y) = \frac{d^2 z}{dx^2} + \frac{d^2 z}{dy^2} = 0 \quad \text{Eq. IV.4}$$

$$\nabla^2 f(x, y) \approx \frac{1}{h^2}\left(f(x - h, y) + f(x + h, y) + f(x, y - h) + f(x, y + h) - 4f(x, y)\right) \quad \text{Eq. IV.5}$$

where $f(x, y)$ is a nodal height value and h is the grid spacing. Next, a weighting scheme was

applied which sampled the surface more densely in areas local to the raw surface data. Weighting in this manner increases the influence of well-fit areas of the resampled surface on our nonrigid correction method. The strategy was composed of (1) a sparse set of points set at 5 mm spacing underlying the full extent of the surface and (2) a dense set of points set at 0.25 mm spacing within a specified capture radius, 1 mm, of the raw surface data. Parameter values were established through a parametric sweep. Finally, the fitted surface was trimmed, such that it represents a single region accurately bounded by the outer contour of the raw data, using a dilate-and-fill image processing procedure.

IV.2.2.6 Rigid Registration

For the purposes of image-to-physical registration, rigid alignment was determined using a salient feature weighted iterative closest point registration [42], specifically designed for liver anatomy and used in a commercial IGLS system. More specifically, salient feature registration utilizes homologous anatomical features to bias point correspondence estimation at each iteration. The biased weighting scheme preferentially favors alignment of preoperatively designated anatomical features with corresponding intraoperative surface data, producing a robust initial alignment that provides support to successive digitization of the remainder of the organ surface. Correspondence is estimated using a conventional closest point operator. The algorithm provides a coordinate transformation that minimizes residual error between preoperative and intraoperative organ surface data.

IV.2.2.7 Nonrigid Registration

When modeling nonrigid behaviors, we employ a linear elastic biomechanical model of the preoperative organ described previously [60]. Large deformations and more

sophisticated constitutive models are possible; however, applying a rigid registration followed by smaller nonrigid deformations is a first order deformation correction approach which, when considering localization errors and tracking accuracy, is appropriate. The benefit of a nonlinear corotational finite element formulation (one nonlinear approach for accounting for large deformations) yielded no statistical difference in our previous work [60]. It is likely that geometric and material nonlinearities will be needed in the future as instrumentation integration matures but our present framework does represent a step forward in providing significant localization improvement over rigid registration. In addition, the use of a linear model allows for pre-computation strategies for providing fast intraoperative nonrigid registration for real time use. The patient-specific geometric model assumes that the liver is an isotropic solid described by the 3D Navier-Cauchy equation:

$$\nabla\left(\frac{E}{2(1+v)(1-2v)}\nabla\cdot u\right)+\nabla\cdot\left(\frac{E}{2(1+v)}\nabla u\right)=0 \qquad \text{Eq. IV.6}$$

E is Young's modulus, v is Poisson's ratio, and u is the displacement vector. We solve the system of partial differential equations (PDE) by applying the Galerkin weighted residual method using linear Lagrange basis functions on tetrahedral finite elements. Displacement boundary conditions are employed on the posterior liver surface to simulate the impact of liver mobilization and packing. On remaining surfaces, the natural stress-free boundary condition is employed. Potential posterior displacement surfaces can be designated *a priori* and allow for pre-computation strategies for fast model correction. We embed this model within a novel nonrigid registration framework. In the surgical setting, the organ is first mobilized from abdominal connective tissue and packed with supportive material for presentation. These changes in support manifest as deformations, i.e. global shape changes, in comparison to the preoperative organ configuration. The algorithm we employ to correct

for these deformations is an improved form of the nonrigid registration method introduced by Rucker et al. [60]. The method assumes a predetermined support surface based on operative approach, in this case the posterior surface of the liver. A parameterized posterior displacement field is iteratively computed to minimize residual error between the intraoperatively collected anterior surface data and the deformed model surface. The result is a reconstructed volumetric prediction of the deformed organ based on the preoperative biomechanical model and sparse intraoperative surface data. With respect to modifications to the method presented in Rucker et al., posterior support surfaces were allowed to move only in the direction of the posterior surface normal [60]. In this paper, we employ an improved extension to the posterior surface parameterization to include tangential displacements as well. Thus, the set of parameters used to generate our nonrigid fitting is:

$$P = \{\bar{c}_n, \bar{c}_{t1}, \bar{c}_{t2}, t_x, t_y, t_z, \theta_x, \theta_y, \theta_z\} \quad \text{Eq. IV.7}$$

where $t_x, t_y, t_z, \theta_x, \theta_y, \theta_z$ are the traditional translational and rotational components associated with rigid body registration, and $\bar{c}_n, \bar{c}_{t1}, \bar{c}_{t2}$ are the control parameters for the posterior surface conditions for the normal and the newly added two tangential components. The control parameters are associated with a bivariate polynomial that systematically deploys boundary conditions to the entire support surface in a given iteration. The methodology has incorporated the salient feature weighting throughout and traditional elastic energy constraints for controlled deformations. Following Rucker et al., the Levenberg-Marquardt algorithm was employed to reconstruct the optimal parameter set to fit acquired surface data.

IV.2.2.8 Experimental Design

To evaluate the accuracy and robustness of surface-based IGLS registration methods as a function of surface collection pattern, density, and noise level, we conducted an extensive

study with our novel human-to-phantom IGLS validation framework. An overview of the simulation design is presented in Fig. IV.4. In this simulation, for each clinical surface collection pattern (i.e. one of the n=13 cases reported herein), surface data were aligned, scaled, and projected onto the intraoperative phantom CT surface (as described in II.D). For each clinical pattern, 50 distinct surface digitizations were created by temporally applying distinct random sinusoidal noise patterns, resulting in a total of 650 independent, clinically representative digitizations of the intraoperative phantom surface. Our rigid (II.F) and nonrigid (II.G) registration methods were used to determine predictions of the intraoperative subsurface target locations. Our resampling approach (II.E) was applied to the simulated surface collections. Similarly, the resampled data were used to drive rigid and nonrigid registration to form predictions of the intraoperative subsurface target locations. This analysis was repeated with increasing levels of noise (base, 2x, 4x, and 8x). *Notably, any surface-based registration, rigid or nonrigid, can be evaluated using this novel validation approach while requiring no additional clinical effort.*

It is important to emphasize that all simulated surface digitizations of the human-to-phantom data set exist on the same phantom which underwent mock OR deformation documented within a CT imaging unit. Furthermore, subsurface beads embedded within the hepatic phantom and tracked throughout deformation provided true positions of targets for the evaluation of registration accuracy. For this study, target registration error (TRE) serves as the primary measurement of accuracy. Deformed target locations extracted from the mock intraoperative CT serve as the observed, true locations of targets. TRE is calculated as the Euclidean distance between the model predicted and true observed target locations.

The Wilcoxon rank-sum test was used to determine significance in differences between registration results between the 4 categories of results: raw data rigid registration,

raw data nonrigid registration, resampled data rigid registration, and resampled data nonrigid registration. The Wilcoxon rank-sum test tested the null hypothesis that the distributions of average TRE for given methods were equivalent with a significance level of $\alpha = 0.05$.

IV.2.3 Results

IV.2.3.1 Phantom and Resampling Suitability

Clinically acquired organ surface digitizations (i.e. Fig. IV.5.A) were applied to the hepatic deformation phantom (i.e. Fig IV.5.B) to observe the impact that clinically-relevant variation in organ surface digitization has on IGLS registration accuracy and variance. As Fig. IV.5.B demonstrates, the ability of the proposed method to transform clinically collected surface data as a template for surface acquisition on the hepatic phantom is quite appropriate. In each set shown (left, and right column of Fig. IV.5.A-B), regional point density and acquisition pattern are preserved from clinical to phantom surface. The base amount of applied noise resulted in measured noise within the simulated surfaces of approximately 1.0 ± 0.7 mm. Fig IV.5.C shows the resampling treatment of the data from each case using methods described in II.E. The overall fit of the resampled surface to the raw input data had a residual closest point error of 1.5 ± 1.3 mm.

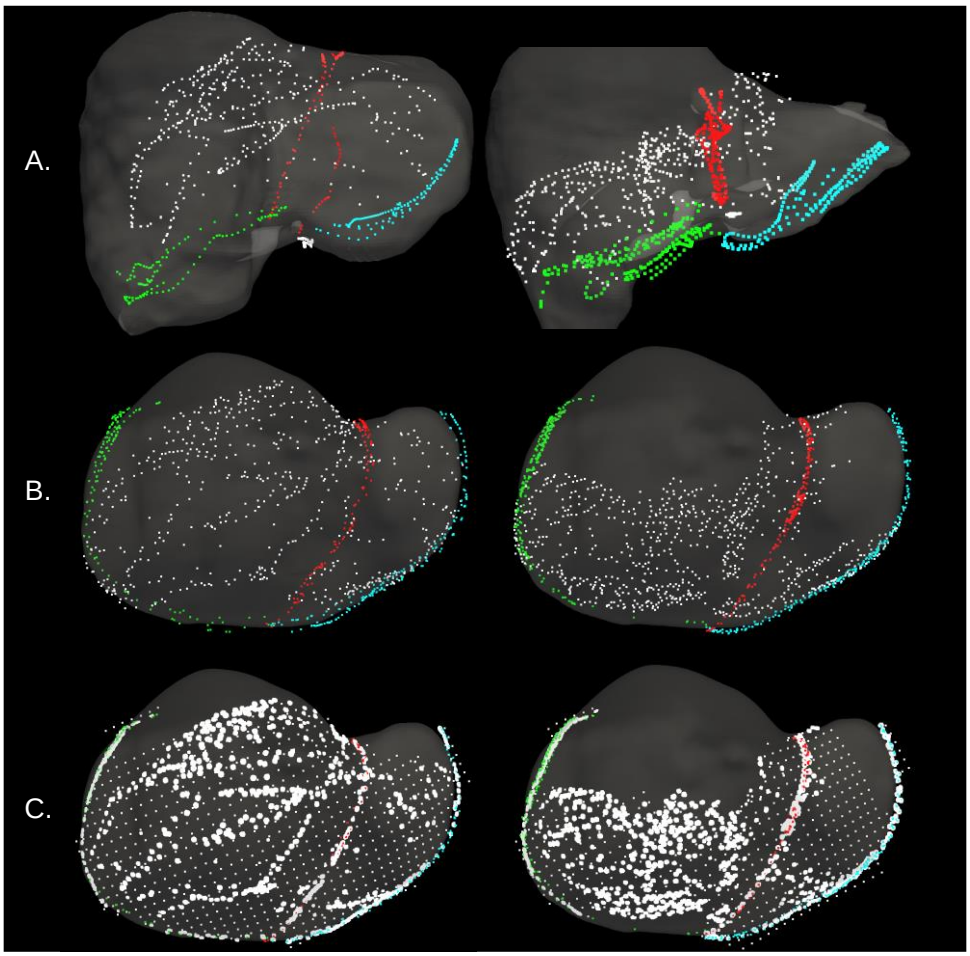

Fig. IV.5. Surface digitizations from two cases are presented. Anterior organ surface, falciform, left inferior ridge, and right inferior ridge data are presented in white, red, blue, and green respectively. (A) Surface data from clinical studies collected with an optically tracked stylus. Surface data are overlaid on the preoperative organ model following rigid registration. (B) Examples of the human-to-phantom data set following translation of the clinical surface data from (A) onto the hepatic deformation phantom – used to simulate clinical collection patterns and sampling. (C) A representation of the spatial data resampling approach applied to the human-to-phantom data in (B). Areas of high density and sparse surface points present as the bright white and gridded white points respectively. For (B) and (C), surface data are overlaid on the intraoperative phantom CT model. (© 2017 IEEE)

A qualitative analysis of the degree and pattern of deformation within the phantom is presented in Fig. IV.6. Rigid registration results are displayed for a representative clinical data registration in Fig. IV.6.A and its hepatic phantom counterpart data in Fig. IV.6.B. In both, the preoperative derived model surface is color-coded by the signed closest point distance of the rigidly registered intraoperative surface data (note that as phantom data is acquired from CT images, we have access to the entire surface extent). The phantom presents a similar pattern and magnitude of deformation to the clinical case.

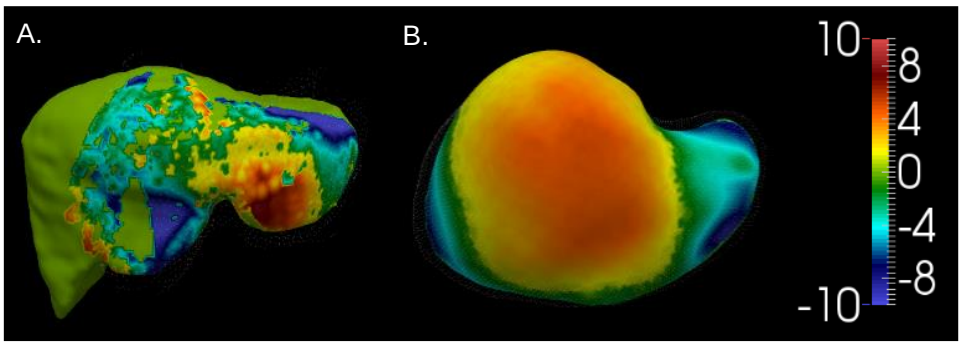

Fig. IV.6. Deformed surfaces from (A) a clinical / human data case and (B) the phantom case are shown. The color map illustrates the observed deformation in each case as the Euclidean distance between the preoperative and intraoperative organ anterior surfaces (in mm) following rigid registration. (© 2017 IEEE)

IV.2.3.2 Registration Error

The objective of this investigation was to characterize the impact that variations in collected organ surface data have on surface-based IGLS registration techniques in a clinically-relevant manner. TRE results using both raw and resampled surface acquisitions were compiled following rigid and nonrigid registration. Fig. IV.7 presents a histogram of the average values of TRE measured from subsurface targets for each case of surface data in our human-to-phantom data set. The (*) represents the difference between procedural

standard and the approach we are proposing. Fig. IV.8 presents a scatterplot which contrasts the raw data TRE and resampled data TRE for both rigid (blue) and nonrigid (gold) registration methods. With both clusters, we see a shift to the right side of the unity line indicating that the process of resampling serves to reduce target error. Fig. IV.8 also indicates that nonrigid registration consistently produces lower TRE than rigid registration. For reference, if the resampling method had no effect on the surface data, all points would align along the line of unity. Table IV.I represents the average value of TRE in a case-by-case manner. In the case of both raw and resampled data, nonrigid registration produced significantly lower TRE ($p < .001$). Rigid registration with resampled data (8.4 ± 0.5 mm) produced significantly lower TRE ($p < .001$) than rigid registration with raw data (10.9 ± 0.6). Nonrigid registration with resampled data (5.3 ± 0.5 mm) also produced significantly lower TRE ($p < .001$) than nonrigid registration with raw data (6.7 ± 0.9 mm). It is particularly noteworthy to point out that nonrigid registration using the proposed resampling method resulted in significantly lower TRE ($p < .001$) than the current commercially available procedural standard method with unprocessed, raw data. For reference, rigid, and nonrigid registration results using the dense, full anterior surface from the intraoperative phantom CT also are presented in Table IV.I as a gold standard comparison.

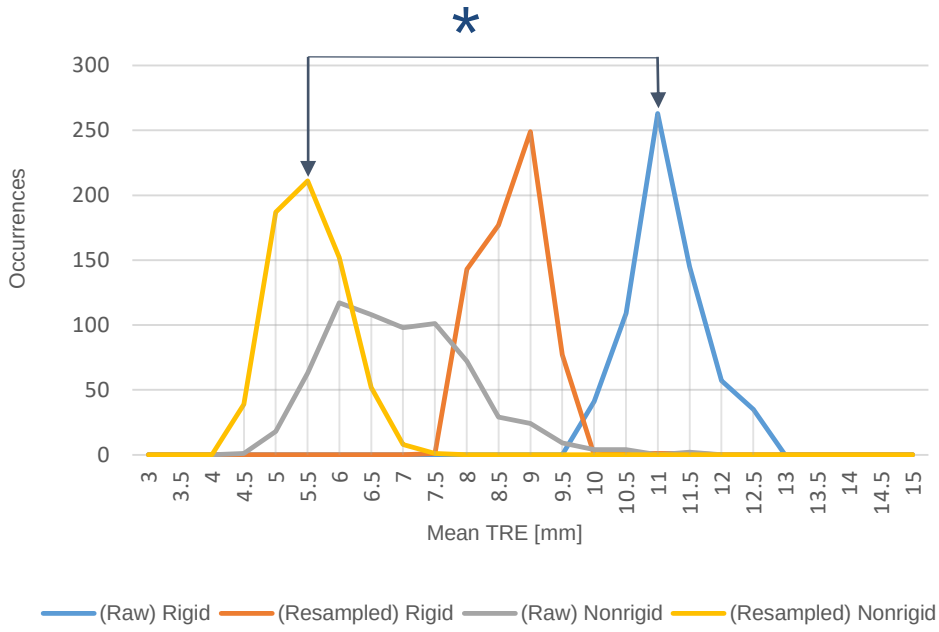

Fig. IV.7. Histogram of average TRE over the 650 simulated cases using raw and resampled data to drive rigid and nonrigid registration. The asterisk denotes significant reduction in error between the current commercial IGLS rigid registration method (blue) and proposed nonrigid registration with resampled data (gold).

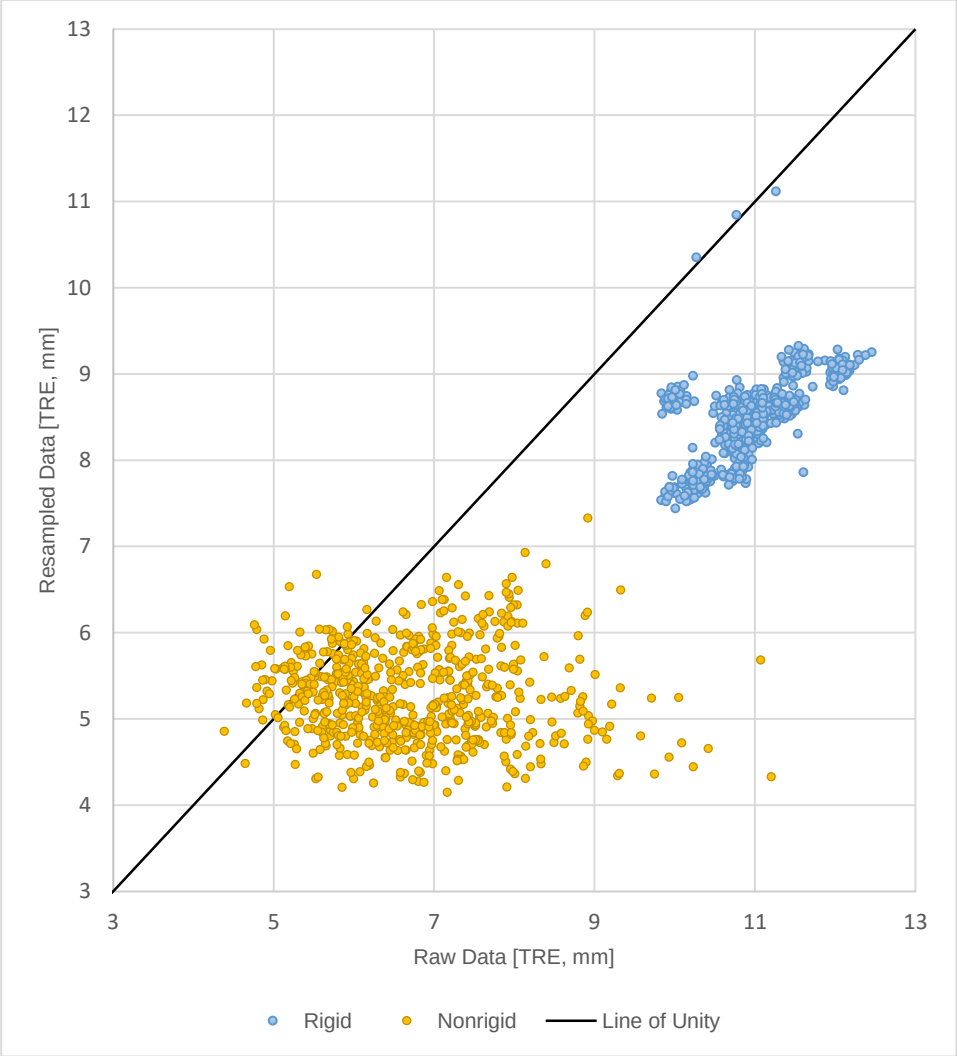

Fig. IV.8. A scatterplot of average TRE over the 650 simulated cases. The x-axis represents average case TRE using a simulated raw surface data scenario while the y-axis represents that simulated surface data after undergoing resampling. Rigid and nonrigid registration results are presented in blue and gold respectively.

TABLE IV.I
Average case TRE (mm) at base noise level

Case #	Raw Data		Resampled Data	
	Rigid	Nonrigid	Rigid	Nonrigid
1	10.8 ± 0.1	7.0 ± 0.6	7.9 ± 0.1	5.8 ± 0.3
2	10.3 ± 0.1	7.4 ± 0.3	7.9 ± 0.4	5.2 ± 0.3
3	10.2 ± 0.2	7.8 ± 0.5	7.7 ± 0.1	6.2 ± 0.4
4	11.0 ± 0.1	5.5 ± 0.4	8.3 ± 0.1	5.4 ± 0.2
5	10.7 ± 0.1	5.9 ± 0.8	8.6 ± 0.1	5.6 ± 0.4
6	10.9 ± 0.1	8.3 ± 0.9	8.6 ± 0.1	5.1 ± 0.4
7	11.2 ± 0.1	6.9 ± 0.4	8.7 ± 0.4	4.8 ± 0.2
8	10.8 ± 0.1	7.7 ± 1.3	8.2 ± 0.1	4.6 ± 0.3
9	11.4 ± 0.1	5.6 ± 0.3	8.6 ± 0.1	5.2 ± 0.3
10	11.5 ± 0.1	6.9 ± 0.9	9.1 ± 0.1	4.9 ± 0.2
11	10.7 ± 0.1	6.0 ± 0.5	8.4 ± 0.4	4.9 ± 0.3
12	10.0 ± 0.1	6.2 ± 0.8	8.7 ± 0.1	5.7 ± 0.3
13	12.1 ± 0.1	6.2 ± 0.4	9.0 ± 0.1	5.3 ± 0.3
AVG	10.9 ± 0.6	6.7 ± 0.9	8.4 ± 0.5	5.3 ± 0.5
Ideal Data (CT)	Rigid, 6.4 & Nonrigid, 4.7			

Table IV.II presents average TRE results for increasing amounts of noise. The evaluation was implemented for the base level of noise (1.0 mm) and amplifications of 2 (1.9 mm), 4 (3.8 mm), and 8 (7.6 mm) times the base level. For all scenarios of registration method and surface data, TRE results were observed to increase as the noise level was increased. Improvement in rigid registration TRE provided by resampling was observed to remain at all levels of noise. At an amplification of 8 times clinically observed noise the improvement to nonrigid registration provided by resampling was absent.

TABLE IV.II
Average TRE (mm) at varying noise levels

Noise Level	Raw Data		Resampled Data	
	Rigid	Nonrigid	Rigid	Nonrigid
Base	10.9 ± 0.6	6.7 ± 0.9	8.4 ± 0.5	5.3 ± 0.5
2x	10.9 ± 0.5	6.7 ± 0.8	8.5 ± 0.4	5.5 ± 0.3
4x	11.0 ± 0.6	6.9 ± 0.9	8.7 ± 0.5	6.4 ± 0.3
8x	11.3 ± 0.6	7.5 ± 0.9	9.1 ± 0.5	8.5 ± 0.7

IV.2.4 Discussion

The results presented illustrate the first study designed to characterize the impact of varying IGLS modus operandi on rigid registration and model-based deformation correction methods. While prior work in the field has investigated varying methods of image-to-physical registration and varying methods of sparse data collection, this study is novel in that it examines the extent to which operational differences in data collection may influence registration results. More explicitly, this study is novel in that it approaches the problem of surface-based registration by considering the registration itself as a black box and solely investigates how the quality of input data influences the registration output. In addition, it proposes to investigate this within the context of a novel data-driven approach whereby applied clinically acquired surface digitization patterns are transformed to a hepatic deformation phantom surface for the purpose of rapid and robust systematic methodological

validation. This validation framework affords the study of large data sets, with true subsurface validation targets, that would require enormous resources to acquire clinically. Lastly, this novel framework provides the ability to propose and validate a resampling procedure which we show to improve registration robustness. Further, we discuss how the results of this study demonstrate that the nature and quality of the data driving registration is as important as the registration method itself and suggest the efficacy of our human-to-phantom data framework.

The representations (shown in Fig. IV.7-8 and Tables IV.I-II) of the impact that variation in acquired surface pattern, density, and noise has on sparse surface-based registration methods in IGLS indicate that IGLS methods based on raw manually swabbed sparse surface data are not optimal with respect to robustness. This is of note considering our experience in observing that surface data collection extent and density varies across patient presentations and physician utilization of the IGLS system. Fig. IV.7 and Tables IV.I-II demonstrate the higher variance that is seen in the current nonrigid approach (Raw Nonrigid) in comparison to the commercial rigid registration method (Raw Rigid), i.e. we see a marked spread in the distribution of occurrences of the gray line as compared to the blue. This behavior makes it quite apparent that the nonrigid registration method is sensitive to variations in surface data collection via swabbing. That being said, the evaluated nonrigid registration method consistently outperformed rigid registration in terms of accuracy when using raw data (with ~39% improvement). The results from our surface resampling technique show our ability to systematically improve the accuracy and reproducibility of both rigid and nonrigid registration methods in IGLS. More specifically, when data are synthesized in a clinically-relevant fashion, surface resampling significantly improved registration results regardless of data pattern and density at reasonable levels of noise. This is dramatically

shown in Fig. IV.7-8 and Tables IV.I-II. The resampling strategy improved rigid and nonrigid registration TRE by 22.5% and 21.3% respectively. Equally striking, resampling combined with nonrigid registration produced a 51.5% improvement in TRE when compared to the current commercial rigid registration method (take note of the * in Fig. IV.7).

Central to the proposed framework was that the deformations induced in our phantom scenario have similar characteristics with the intraoperative counterpart. In Fig. IV.6 we see a direct comparison between clinical signed closest point data in Fig. IV.6.A and the equivalent (although larger extent) for our phantom setup in Fig. IV.6.B. To assist interpretation, both surfaces experience similar magnitudes in surface-to-surface misfit. While the phantom surface appears somewhat different than the clinical surface, the distribution demonstrates a general pattern that we often see within image-to-physical rigid registration in IGLS data. More specifically, it is observed that the anterior surface of the organ becomes more planar after mobilization and packing, which produces an observable elevation of the lateral segments while the more medial regions of the organ remain relatively static. In a separate extensive study looking at patterns of intraoperative model-to-OR-data fit, [122] also observed this behavior. Additionally, these phantom results are in accordance with our previous phantom studies which entailed multiple novel deformations as reported in [60] and a different liver phantom as in [135]. We acknowledge that the human-to-phantom validation framework could be further strengthened with additional phantom work (derived from varying clinically acquired anatomy), more deformations, and more clinical sparse surface data patterns; and while demonstrated in past work [60, 135], all of these areas are an important continued direction for the future. However, we should note that this work does add significantly to past contributions. For example, in Fig. IV.6 it is demonstrated that the current phantom experiences a similar magnitude and a realistic pattern of deformation

to routine IGLS data. In Fig. IV.5, the quality of sparse surface data is maintained between clinical acquisition (Fig. IV.5.A) and application to the phantom (Fig. IV.5.B). While further additions as suggested above will undoubtedly improve the utility and clinical accuracy of our human-to-phantom validation framework, the environment we have developed has provided meaningful results and a potentially powerful pathway forward for validation of image-to-physical registration in the future.

IV.2.5 Conclusions

This investigation represents a significant advancement in the understanding of the degree that acquired intraoperative surface data variation influences the outcome of IGLS sparse-data image-to-physical registration. The work demonstrated that surface data resampling shows significant promise for improving the accuracy and reproducibility of IGLS rigid and nonrigid registration. While further investigation is required to fully characterize the optimal workflow-friendly strategy for IGLS surface data collection, the surface resampling presented here is an advancement toward minimizing the impact of data collection strategy on model-updated surgical navigation systems for the hepatic environment.

While these results are important, it is also important to recognize the novelty and utility of the human-to-phantom framework proposed in this work. As the field of soft-tissue image guidance moves forward, the intraoperative validation of these approaches requires enormous effort either using workflow-cumbersome infrastructure such as intraoperative MRI [37] or lower cost but challenging measurement methods such as spatially localized intraoperative ultrasound [62]. The framework proposed herein creates controlled phantom deformation events comparable to those documented in the OR. The

evaluated registrations are driven based on intraoperative data compatible with the IGLS modus operandi, transformed to the mock organ surface. This approach is unique in that it has the advantage of full volumetric deformation measurements in a controlled environment but also uses data acquired from a realistic workflow to drive alignment strategies. We believe this is a significant step forward in validation design for this challenging environment. When comparing the study presented here with our more burdensome ultrasound counterpart study in [62], the compatibility of results suggests that this may indeed be an exciting step forward for more tractable investigations in the future.

Chapter V

Deformation Correction and Retrospective Modeling

V.1 Summary and Contributions

In Chapter IV, a human-to-phantom data framework was introduced to provide extensive and rapid testing of image-to-physical registration methods outside of the OR. Here, this framework was applied to a new deformable hepatic ablation phantom, allowing ablation information within a series of phantom ablation procedures (e.g. ablation probe location and the extent of the induced necrotic zone) to effectively be used as ground-truth targets for registration assessment. This chapter evaluates the application of a model-based deformation correction method [60] within image-guided MWA in comparison to the rigid registration algorithm of [42]. In addition, a retrospective computational model of MWA was determined and deployed within the image-to-physical registration to evaluate the compounding errors associated with this combined therapeutic and navigational framework. Furthermore, by means of the human-to-phantom data framework of Chapter IV, registrations were evaluated with surface data representative of both open surgery (e.g. sparse anterior surface data from manual swabbing) and interventional radiology (e.g. full surface data from intraoperative imaging).

To date, multiple studies reported in the literature have taken rigid registration approaches to image-to-physical registration for image-guidance during hepatic ablation procedures. However, until the work presented in this chapter, none have addressed the challenges imposed by soft-tissue deformation. The results herein demonstrate, in an initial phantom experiment, a significant advancement in the field of image-guided hepatic microwave ablation. While future work is necessary to apply this modeling and navigational

framework as a prospective, targeting approach, the deformation correction method applied in this study is certainly an advancement toward improved localization. Going further, this work extends the concept of 'model correction' to include a new biophysical domain, namely the deposition of ablative energy, and its corresponding thermal evolution. This combined mechanics and energy framework represents a first study in a more comprehensive model-predictive paradigm for an important image-guided therapeutic process in use today.

V.2 Application of multiphysics modeling for comprehensive guidance in hepatic microwave ablation

The work in this chapter appears in:

J.A. Collins, J.S. Heiselman, L.W. Clements, and M.I. Miga, "Application of Multiphysics modeling for comprehensive guidance in hepatic microwave ablation." In preparation.

Abstract

While numerous methods have been presented which provide varying degrees of intraoperative tumor localization for hepatic microwave ablation procedures, soft-tissue deformation represents a considerable source of error for current applications. With this study, we propose that model-based deformation correction methods can be applied within image-guided microwave ablation procedures to improve the accuracy and efficiency of intraoperative tumor localization and antenna placement. Furthermore, computational modeling of microwave ablation can be integrated within the navigational environment to provide more advanced guidance. In this work, we compare a surface-driven, model-based deformation correction method to a clinically-relevant rigid registration approach within a deformable hepatic ablation phantom. In addition, we employ a retrospective model of microwave ablation following registration – allowing for an evaluation of the fidelity of the combined therapeutic and navigational framework. When driving registrations with radiological intervention-inspired full surface data, the deformation correction method (2.5 ± 1.1 mm) improved average ablation antenna registration error by 58.9% compared to rigid registration (5.6 ± 2.3 mm) and on average improved volumetric overlap between the modeled and ground-truth ablation zones from 67.0 ± 11.8 % (rigid) to 85.6 ± 5.0 % (corrected). Furthermore, when using surgically-inspired sparse surface data, the

deformation correction improved registration error by 38.3% and volumetric overlap from 64.8 ± 12.4 % (rigid) to 77.1 ± 8.0 % (corrected). This work demonstrates, in an initial phantom experiment, an advancement toward improved procedural navigation in image-guided hepatic microwave ablation procedures.

V.2.1 Introduction

Loco-regional therapies, such as thermal ablation, have received increased indications for use in neoadjuvant roles, ablation assisted resection, and for the treatment of unresectable hepatic malignancies [18-30]. While radiofrequency ablation (RFA) is the most common ablative therapy used clinically, it has presented a relatively high local recurrence rate (12-39%) when compared to microwave ablation (MWA) (6-8.8%) [20-24]. Additionally, in matched cohort studies, patients receiving MWA saw improved survival compared to those receiving RFA [21-22]. Furthermore, MWA has received considerable interest due to its larger spatial extent of power deposition, penetration through charred tissues, and ability to ablate up to and around large vessels [21-22, 31]. Due to advances in neoadjuvant care, therapeutic options, and improved patient selection criterion, the long-term survival of patients receiving ablation treatments for hepatic colorectal cancer metastases has improved significantly in recent years [18, 22, 29], and in smaller tumors (≤ 3 cm) is comparable to the clinical standard of surgical resection that offers five-year survival of 44-50% in patients with metastatic colorectal cancer [11].

As the procedural process inherently targets internal structures, the efficacy of ablation is highly reliant on accurate localization and targeting of these subsurface diseased tissues during a procedure, as inaccurate delivery can lead to incomplete treatment and local recurrence [32]. As such, ablations are generally performed using image-guidance (e.g.

intraoperative ultrasound imaging (iUS) or computed tomography (CT)) to assist in tumor localization and probe placement. However, with these methods, real-time localization, monitoring, and assessment are extremely limited [38]. Advanced surgical navigation approaches have been used to create a spatial mapping between surgical instrumentation and imaging data to improve visualization of anatomical structures. Recent applications of such work to image-guided ablation procedures have reported enhanced localization of tumors and improved accuracy of ablation antenna placement in open [43-47] and laparoscopic procedures [48-50]. These methods have employed a variety of electromagnetic (EM) tracking and image-to-physical registration methods to provide enhanced image-guidance. However, to date, image-guided ablation methods providing image-to-physical registration have been limited to rigid registration approaches, which neglect soft-tissue deformations that occur from organ mobilization during procedures and can cause substantial registration error [51]. EM-tracking methods avoid this issue by limiting tracking to the real-time position of surgical tools and iUS imaging. However, when compared to image-to-physical registration the EM-iUS approach limits the subsurface information that is provided and loses efficacy when targeting lesions in cirrhotic patients or in those with chemotherapy-induced hyperechogenicity associated with steatosis, both which can compromise ultrasound lesion visualization [52-53].

Several model-based soft-tissue deformation correction approaches have been presented in the literature for image-to-physical registration for hepatic resection. For example, Lange et al. published an algorithm using thin-plate splines to deform preoperatively acquired vessels to intraoperative vessels acquired from tracked iUS [55]. Hu et al. presented a method using coherent point drift to nonrigidly register vessel landmarks, such as bifurcations [56]. Alternatively, other approaches have concentrated on achieving

surface-based deformation correction methods. Rucker et al. described an inverse approach which optimizes boundary conditions described by a parameterized posterior displacement field, based on the reality of organ deformation during operative mobilization, to minimize the residual error between the intraoperatively collected anterior surface digitization and the deformed model surface [60]. More recently, Heiselman et al. expanded upon the work of Rucker et al. by reformulating the application of boundary conditions to a control point strategy which allows for multiple independent support surfaces to be designated [61]. Both surface-based methods have demonstrated effective correction of soft-tissue deformation in phantom and clinical applications for hepatic resection [60-64].

Current clinical standards for ablation procedural planning entail geometric estimates of expected ablation zone size and shape provided by device manufacturers based on experimental measurements taken from *ex vivo* animal tissue. As such, these predictions ignore patient-specific anatomical and physiological variation, potential tissue heterogeneity, tissue perfusion, and differences in disease state that may be present. Accordingly, such estimates have been observed to overpredict size and result in more homogenous shape when compared to clinical ablation outcomes [65-66]. Predictive, biophysical modeling of MWA presents a strong alternative to the manufacturer-provided estimates of ablation outcome by utilizing numerical approaches to solve the physical governing equations defining energy deposition and heat transfer. Recent approaches have focused on treating tissue properties as a function of temperature [74-76]. However, these models have generally been characterized within *ex vivo* animal tissue or simulation and inherently overlook variation that can present between patients due to differences in tissue properties [74-76] related to perfusion [79-83] or disease state (e.g. cirrhosis or fatty liver disease [84-85]). As a result, there is a further need for prospective MWA modeling

approaches which address the differences in tissue properties that can occur on a patient-to-patient basis. Furthermore, these ablation estimates and models are often presented as either tables or contours rather than being fully integrated with patient imaging data, therefore posing a challenge for physicians when planning procedural approach. As such, the integration of advanced surgical navigation methods with accurate, prospective MWA modeling presents a powerful alternative to the current clinical standard for ablation planning and execution.

Based on our existing image-guidance work for surgical resection [60-64], we propose that soft-tissue deformation correction methods can be applied to image-guided MWA to improve the accuracy and efficiency of intraoperative tumor localization and probe placement. Furthermore, we suggest that computational modeling of MWA can be integrated within the surgical environment for guidance purposes using these advanced image-to-physical registration methods. As an initial step, we present a hepatic deformation phantom experiment designed to evaluate the accuracy of ablation probe localization when using the deformation correction method of [61] in comparison to a clinically-relevant rigid registration method [42]. Additionally, we present a retrospective model of microwave ablation which we combine with our image-to-physical registration strategies, allowing us to quantify and distinguish the errors associated with the MWA model and image-to-physical registration methods. To our knowledge, this is the first study to evaluate the combined errors associated with localized procedural modeling and image-guidance methods for hepatic MWA procedures. While providing anatomical localization is the principal feature of a model-based deformation correction strategy, it is equally interesting to extend biophysical modeling methods into this domain and determine their contribution to fidelity relative to procedural ground truth.

V.2.2 Methods

V.2.2.1 Overview of Validation Study

In this study a deformable hepatic phantom constructed of albumin suspended in agar was treated with 915 MHz microwave ablation (ST antenna, Perseon, Salt Lake City, UT) creating a visible ablation lesion. The ablated phantom was imaged using T_2-weighted MRI, from which the phantom boundary, ablation zone, antenna tip, and antenna insertion point were segmented in the initial "pre-deformation" pose of the phantom. Next, support blocks were inserted beneath the phantom to change the underlying posterior support surface shape as well as to shift the ablation. The phantom was then re-imaged in this "post-deformation" state, providing the same information as before but in this new deformed pose. This two-step process effectively provided all procedural delivery information and ablation physical outcomes in a 'before' and 'after' deforming event.

Image-to-physical registration was then performed by registering the initial pre-deformation image to the mock operating room/interventional suite (OR/IS) surface digitization of the organ generated from the post-deformation imaging data (surgical/OR setting utilizing partial surface data, interventional/IS setting utilizing full surface data). This experimental setup allowed the ablation information to effectively be used as a geometric target for registration assessment. In addition, a retrospective model of the MWA procedure (i.e. a model of antenna power deposition and thermal distribution) was simulated in the pre-deformation pose given the antenna location segmented from MRI. Together, these experiments allow the investigation of how well a computationally-modeled, deformation-corrected ablation prediction performed versus the ground truth ablation extent and location (i.e. the evaluation of a model-based therapeutic and localization system). The experiment

included a total of 3 ablations present in 8 image-to-physical registration scenarios.

V.2.2.2 Summary of Image-to-Physical Registration Methods

Two methods of image-to-physical registration were evaluated in this study: a conventional rigid registration and a nonrigid registration approach which corrects for deformation. Rigid registration methods are currently the standard method used in commercial navigation systems for image-to-physical registration. These methods are very fast, an essential requirement in the OR, but they rely on the assumption that the transformation from image to physical space is purely rigid and therefore could have poor behavior when deformation is present. The rigid registration method used in this study iteratively seeks to align the anterior organ surface and salient anatomical features in the pre-deformation image to the analogous sparse surface and feature data designated in physical space. These data are synthesized from the post-deformation image data in this experiment, although in a typical clinical case, the sparse surface and feature data would be collected by the physician in the operating room with an optically tracked stylus. Typical data collection involves the acquisition of 3D points over the mock anterior liver surface, and specific features (falciform, round ligament, and inferior ridges). To mimic the quality of data available in a clinical setting, a sparse clinical collection pattern was taken of the anterior liver phantom surface in its post-deformation state. We should note that this distribution was extracted from the image volume data rather than acquired from conventional image-guidance instrumentation (details are in section II.G). With respect to the details of the rigid registration, these are described in Clements et al. [42] and its clinical efficacy has been reported in subsequent work [60-64].

To better account for intraoperative deformations in the image-to-physical

alignment, the second method of registration evaluated in this study was a nonrigid, model-based approach designed to account for soft-tissue deformations. This deformable registration method seeks to minimize the difference between the surface generated from the segmented image volume of the preoperative image and the sparse anterior surface data acquired in the mock intraoperative physical space. Briefly, the technique manipulates a set of surface control points distributed across the model surface in areas of anticipated deformation. Perturbations of the control points provide a precomputed distribution of volumetric displacements to the biomechanical model. Intra-procedurally, optimization ensues iteratively with an active boundary condition reconstruction with simultaneous rigid parameter update until the preoperative organ shape matches the intraoperative counterpart. Optimization is performed using the Levenberg–Marquardt algorithm. The details of this method have been reported by Heiselman et al. [61].

V.2.2.3 Microwave Ablation Model

We utilize a 2D axially-symmetric computational model developed within COMSOL Multiphysics (COMSOL Inc, Burlington, MA) and Matlab 2017b (The Mathworks Inc, Natick, MA) to retrospectively model microwave ablation with the 915 MHz Perseon Short-tip (ST) antenna within an agar-albumin phantom. These retrospective models were then registered to their known locations in image space, simulating a preoperatively determined procedural plan. Following image-to-physical registration, we can then evaluate the accuracy of the registered ablation model when compared to the ground-truth ablation zone.

The electromagnetic wave equation was implemented to describe the propagation of electromagnetic waves through the mock soft-tissue phantom.

$$(\nabla^2 + \omega^2\mu\varepsilon_c)\vec{E} = 0 \quad \text{Eq. V.1}$$

where ω [rad/s] is the angular frequency of the electromagnetic wave, μ [H/m] is the permeability, ε_c is the complex permittivity, and $\vec{E}$ [V/m] is the electric field strength. Penne's bioheat transfer equation was employed to describe the temperature evolution and heat transfer.

$$\rho c \frac{\partial T}{\partial t} = \nabla \cdot k\nabla T + Q - Q_p \quad \text{Eq. V.2}$$

where ρ [kg/m^3] is mass density, c [J/kg·K] is specific heat capacity, k [W/m·K] is thermal conductivity, T [K] is the instantaneous temperature, Q [W/m^3] is heat generation, and Q_p [W/m^3] is heat loss due to perfusion. Perfusion was not implemented within the phantom and as a result was excluded from the model. Heat generation within the phantom, Q, was modeled as a function of the rate of microwave energy absorption, as such:

$$Q = \frac{1}{2}\sigma\|E\|^2 \quad \text{Eq. V.3}$$

where σ [S/m] is the electrical conductivity.

An electromagnetic wave transparent boundary condition was applied at the outer edges of the modeling domain to prohibit microwave reflection.

$$\vec{n} \times (\nabla \times \vec{E}) - jk\vec{n} \times (\vec{E} \times \vec{n}) = 0 \quad \text{Eq. V.4}$$

where $\vec{n}$ is the direction normal to the boundary and k is the wave number. In addition, external boundaries where set to a fixed temperature (room temperature). Internal boundaries between the phantom and ablation antenna simulated saline cooling within the antenna with a convective heat flux condition.

$$\vec{n} \cdot (-k\nabla T) = h \cdot (T - T_{ext}) \quad \text{Eq. V.5}$$

where $\vec{n}$ is the normal vector to the element, k [W/m·K] is the thermal conductivity, h [W/m^2·K] is the heat transfer coefficient, T [K] is temperature, and T_{ext} is the saline

temperature (room temperature).

To simulate biological ablation, a mock cell necrosis was approximated as a function of protein denaturation and was estimated at each time step by the Arrhenius damage integral:

$$\alpha = \int_0^t Aexp\left(-\frac{E_a}{RT(t)}\right)dt \quad \text{Eq. V.6}$$

where α is the degree of damage at a given time, A [1/s] is a frequency factor, E_a [J/mol] is the activation energy required to denature the protein within the phantom, R [J/mol·K] is the universal gas constant, and $T(t)$ [K] is the phantom temperature history. The estimated fraction of denatured protein was then calculated by:

$$\theta_d = 1 - e^{-\alpha} \quad \text{Eq. V.7}$$

V.2.2.4 Phantom Property Reconstruction

The model described in Part V.2.2.3 was retrospectively fit to ground truth data from mock histology of our phantom from which ablation extent could be determined. The computational model fitting framework is based on a nonlinear optimization approach where a parameter set defining the dielectric and thermal properties of the phantom domain within the finite element model is iteratively chosen to maximize the overlap between the model-predicted and observed ablation zones.

$$P = [\sigma, \varepsilon, k, c] \quad \text{Eq. V.8}$$

where $\sigma, \varepsilon, k,$ and c are the electrical conductivity, relative permittivity, thermal conductivity, and specific heat capacity of phantom respectively. The objective function is defined by the degree of overlap between the model-predicted and observed ablation zones as such:

$$\Omega = 1 - \frac{N_{TP}}{N_{TP} + N_{FP} + N_{FN}} \quad \text{Eq. V.9}$$

where Ω signifies the ratio of the intersection and union of the model-predicted and observed ablation zones. For this framework, we use the Nelder-Mead downhill simplex method to optimize the parameter set (Eq. V.8) by minimizing the objective function (Eq. V.9). The Nelder-Mead algorithm is a heuristic search approach used to solve nonlinear optimization problems without requiring derivative information.

V.2.2.5 Agar-Albumin Hepatic Deformation Phantom

The deformable hepatic phantom used in this study consisted of a combination of purified water, 1.5 wt% agar-agar powder (Thermo Fischer Scientific, Waltham, MA), and 50 wt% liquid egg whites (Break Free Liquid Egg Whites, The Kroger Company, Cincinnati, OH). Liquid egg whites were used to produce a permanent visual history of the thermal induced ablation lesion, similar in nature to the ablation lesions which form in tissue. Egg whites contain around 10% ovalbumin protein dissolved in 90% water with nearly no carbohydrate or fat content. Thermal denaturing of the ovalbumin protein leads to aggregation which causes optical scattering and a large reduction in the T_2 relaxation coefficient of the material. The resulting ablation lesions were imaged using T_2-weighted MRI and visually observed with mock histology by sectioning the phantom along the midline of the ablation antenna and backlighting the section (As seen in Figure V.1.B-C).

To create the phantom, powdered agar-agar was thoroughly mixed with water and heated to boiling on a hot plate while being continuously stirred to produce a 1.5% agar gel. The solution was then cooled to <60°C with continuous stirring before adding the liquid egg whites. This cooling ensured that no protein denatured prematurely. The mixture was then mixed for 1 minute and then poured into the phantom mold to allow the gel to set. A plaster negative derived from contrast-enhanced CT imaging of a patient liver was used as the

phantom mold to produce a hepatic phantom with clinically-relevant anatomical structure (Fig. V.1).

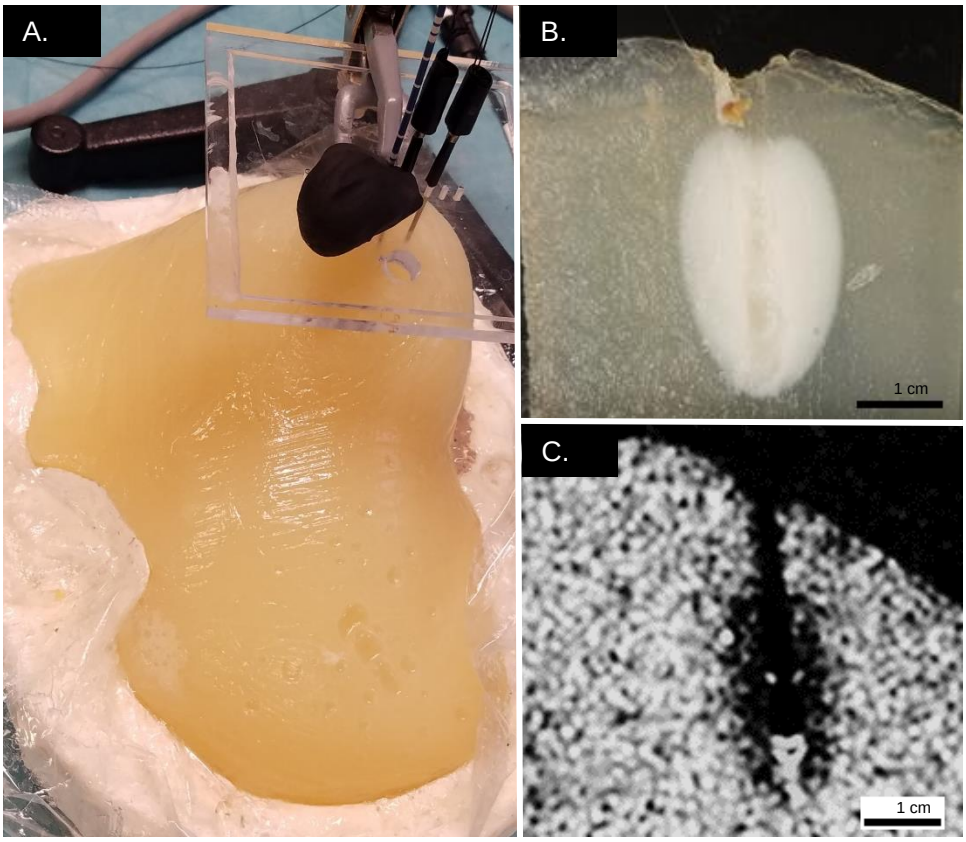

Fig. V.1. (A) Agar-albumin phantom liver in its pre-deformation state. A Microwave ablation antenna is seen inserted into the right lobe. (B) Mock-histology of an ablation within the agar-albumin phantom. The outer ablation contour, ablation antenna tip location, and ablation antenna shaft are clearly visible. (C) Slice from the T2-weighted MRI of the ablation zone from which the outer ablation contour, ablation antenna tip location, and ablation antenna shaft were segmented.

V.2.2.6 Applied Deformations

The proposed modeling and registration framework was evaluated across a range of clinically-relevant organ deformations. In open surgery, deformations occur due to the introduction of packing material beneath and around the organ following mobilization of the organ from surrounding anatomy. These changes between diagnostic and intraprocedural presentation incur shape change. To impose soft tissue deformations, silicone support blocks

(roughly 20-30 mm thick) were inserted beneath varying areas of the phantom. Figure V.2 provides an example of the extent of deformation induced in the phantom. In total, 4 unique applications of deformation were applied to the phantom. In case 1, support material was placed beneath the lateral superior right lobe, raising the largest volume of the phantom. In case 2, support material was added beneath both the lateral superior and inferior right lobe, causing the right lobe to rise and rotate about the falciform ligament. In case 3, support material was inserted beneath the lateral inferior right lobe and the left lobe, causing the medial area of the liver to sag. Finally, in case 4 support material was inserted beneath the lateral inferior right lobe, causing it to rise.

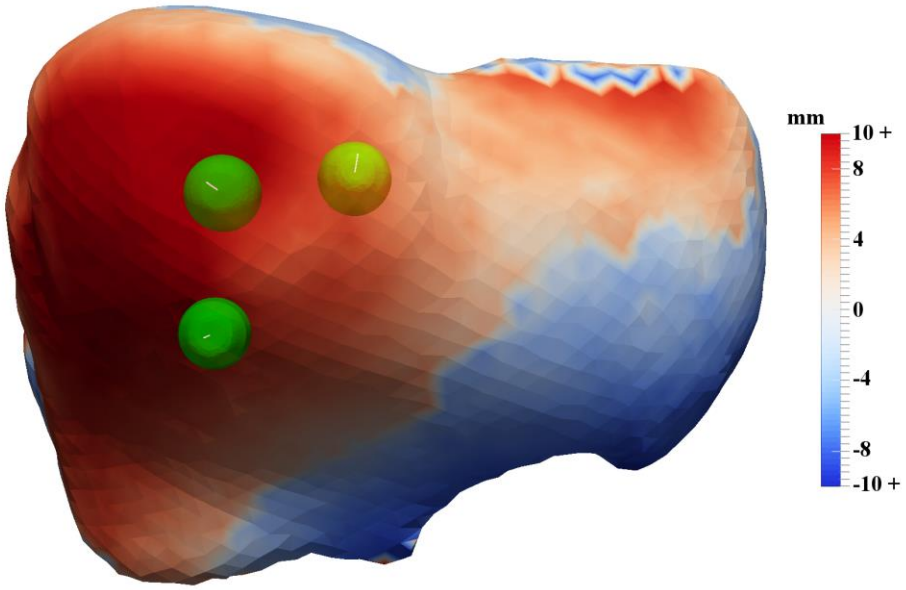

Fig. V.2. Representation of the degree of deformation achieved in the deformable hepatic ablation phantom. The colormap represents the signed surface error after rigidly registering the pre- and post-deformation phantom image segmentations. The ablation antenna shafts are presented as white lines and ablation zones as green volumes. In total, 4 applications of deformation were applied and imaged within the phantom.

V.2.2.7 Data Collection

T_2-weighted MRI scans were acquired for each state of phantom deformation (i.e. 1

pre-deformation image set and 4 post-deformation image sets). 3D models were generated from each set of images using ITK-SNAP [136]. Salient feature regions were manually designated from the surface of each model. To date, these image-to-physical registration methods have been clinically implemented using sparse digitizations of the anterior organ surface attained intraoperatively. Within this study, we present and compare results following registration using (1) IS-inspired full surface data, (2) OR-inspired sparse surface data, and (3) resampled sparse surface data using the resampling method presented by Collins et al. [63].

Sparse anterior surface data, akin to what would be available clinically, were generated using a method similar to the human-to-phantom data described by [63]. Briefly, sparse surface data gathered from actual clinical cases (an IRB approved study at Memorial Sloan Kettering Cancer Center in [62]) were rigidly registered to our mock phantom image volume in its deformed state. This was accomplished using the weighted salient feature registration method of Clements et al. [42]. Once initialized, an affine registration was performed to account for any differences in organ size between the clinical and phantom data. Next, the clinical surface data were projected to their closest points on the deformed phantom surface, resulting in unique realistic sparse anterior surface designations for each case. However, unlike the method of [63], no additional noise was added to these synthesized sparse surface data. All synthesized designations had an extent of organ coverage between 25-30% which is within the range of typical clinical data acquisition [61, 133]. It should be noted that the above process could be performed in the reciprocal workflow allowing for a second set of novel conditions. In total, this created 8 registration scenarios (the original 4 cases from section II.F and the 4 reciprocal instances) for the results herein, each with an independent set of simulated physical space data to drive the registrations.

V.2.2.8 Analysis

Two methods of image-to-physical registration were compared in this study: (1) the salient feature weighted iterative closest point rigid registration method by Clements et al. [42] and (2) the deformable control point nonrigid registration method by Heiselman et al. [61]. Average target registration error (TRE) was used as the primary quantification of registration accuracy. A total of nine targets were measured across the three ablations in each image-to-physical registration scenario: (a) the antenna tip locations, (b) the antenna insertion points on the phantom surface, and (c) the centroids of the MRI-segmented ablation zones. Average TRE for a registration scenario was calculated as the average distance between corresponding points in the registered image and physical data sets. This metric measures the accuracy of the registration methods evaluated in this study exclusively, independent of the MWA modeling.

The positive predictive value (PPV) was used to evaluate volumetric accuracy of the predictive MWA model. PPV was calculated by the following equation:

$$\text{PPV} = \frac{N_{TP}}{N_{TP} + N_{FP}} \qquad \text{Eq. V.10}$$

Where N_{TP} is the volume of the model-predicted ablation zone overlapping with the observed ablation zone and N_{FP} is the volume of the model-predicted ablation zone which does not overlap with the true ablation zone. We present the metric of PPV in this study for two separate purposes: (1) to quantify the predictive capability of the MWA model without compounding registration error and (2) to evaluate the accuracy of the combined registration and MWA modeling framework.

To singularly evaluate the accuracy of the MWA model, the model-predicted ablation zones were directly compared to the mock histology. This comparison was made assuming

perfect registration after manually aligning the ablation antenna tip and shaft from the model space with the corresponding locations in the mock histology image space. The outer ablation contours from each space were then revolved to create 3D volumes which were then compared by calculating the PPV. The combined registration and modeling framework accuracy was also evaluated by computing the PPV following image-to-physical registration of the model-predicted ablation zone. Inaccuracies in both the image-to-physical registration methods and MWA modeling contribute to the error encompassed by this metric.

A t-test was used to determine significance in differences between the distributions of average TRE and PPV resulting from each evaluated registration method ($\alpha = 0.05$).

V.2.3 Results

V.2.3.1 Microwave Ablation Model

Model-predicted temperature maps for each of the 3 ablations with the agar-albumin deformation phantom are presented in Fig. V.3 alongside contours defining the observed and model-predicted ablation zone extents (as black and dashed red lines respectively). These results are under the condition of perfect localization which was achieved by manually aligning the observed and modeled ablation antennas. The degree of ablation zone overlap for this condition presented as the positive predictive value is on average 96.3 ± 0.3%. The observed transverse and axial ablation zone dimensions gathered from mock histology were 20.1 ± 1.0 and 31.6 ± 1.2 mm respectively. Model-predicted ablation zone transverse and axial dimensions were 19.9 ± 1.8 mm and 29.9 ± 0.6 mm

respectively (differing from the mock histology by 4.2% and 5.3% respectively).

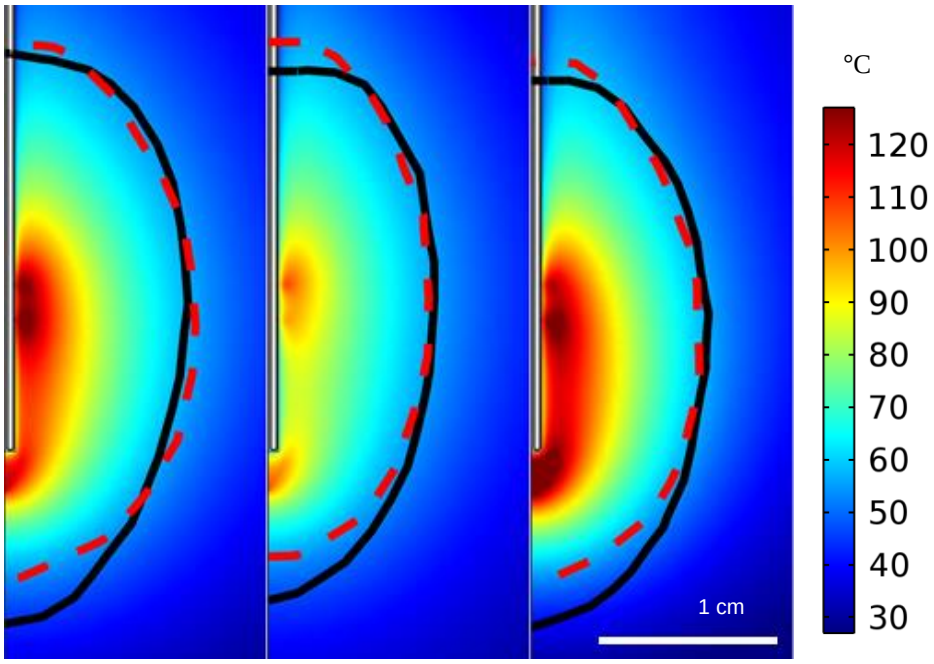

Fig. V.3. Model-predicted temperature maps, observed (black line), and model-predicted (red dashed line) ablation zones are presented for each case of ablation with the Perseon ST antenna within the agar-albumin hepatic deformation phantom. The observed ablation zone extent was gathered from mock-histology and used to drive the retrospective inverse MWA model. It is important to note that each ablation occurred in a different area of the phantom with varying tissue thickness and antenna depth.

V.2.3.2 Image-to-Physical Registration

Target registration errors resulting from rigid registration and deformation correction approaches applied to the 8 image-to-physical registration scenarios within the deformable hepatic ablation phantom are presented in Fig. V.4 for full surface data (top), and sparse surface data (bottom), in blue/yellow and grey/orange, respectively. Average TRE results from driving the registrations with full surface, sparse surface, and resampled sparse surface data are tabulated for both methods of registration in Table V.I.

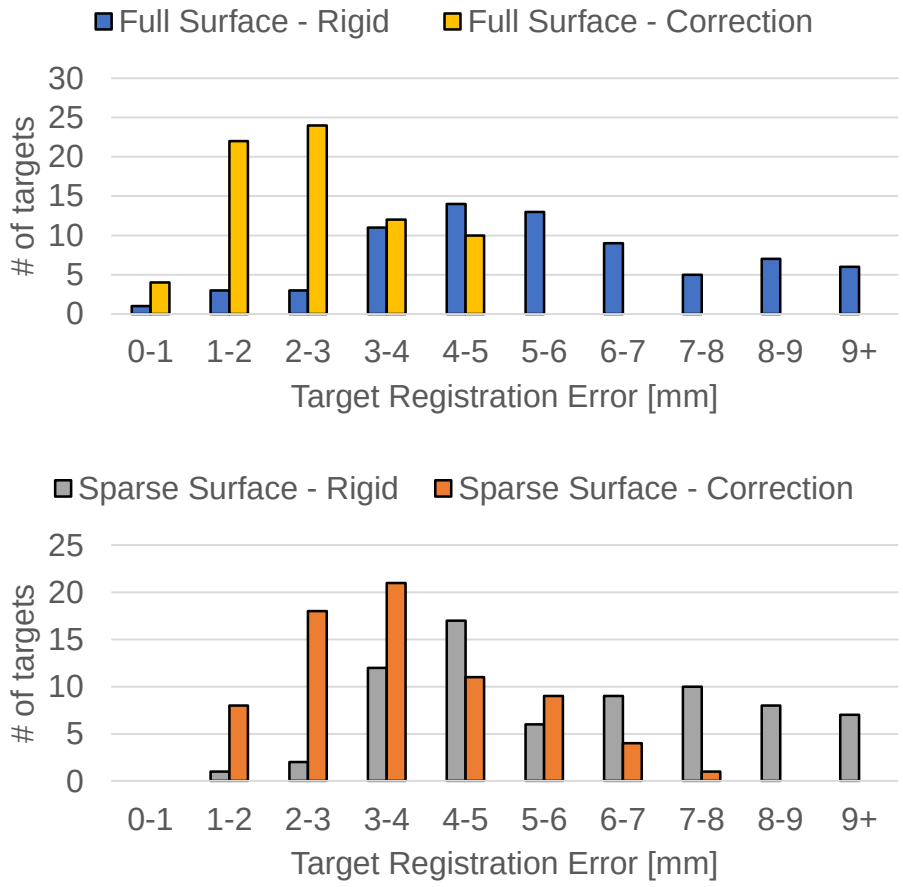

Fig. V.4. Histograms of the target errors resulting from the two methods of registration applied to the 8 image-to-physical registration scenarios within our agar-albumin deformation phantom. Results of the rigid registration using the weighted salient feature ICP method of Clements et al. [42] are presented in blue/grey. Results of the deformation correction method of Heiselman et al. [61] are presented in yellow/orange. (Top) Results from registering with IS/full surface data. (Bottom) Results from registering with OR/sparse surface data.

Table V.I. Average and standard deviation target registration error are presented for each source of surface data and each evaluated method of registration.

	Average Target Registration Error [mm]	
Surface Data	Rigid registration	Deformation Correction
Full	5.6 ± 2.3	2.5 ± 1.1
Sparse	6.0 ± 2.3	3.7 ± 1.4
Resampled	4.9 ± 2.1	3.8 ± 1.3

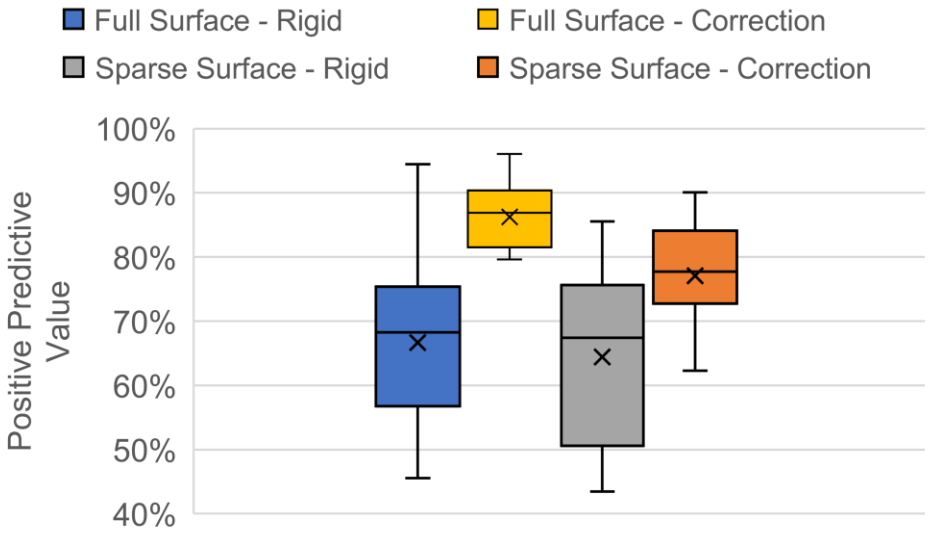

Fig. V.5. Distributions of the volumetric overlap of observed and predicted ablation zones represented by the positive predictive value. The box and whiskers represent the mean, median, upper and lower quartiles, maximum, and minimum PPV for the rigid registration method of Clements et al. [42] in blue/grey and the deformation correction method of Heiselman et al. [61] in yellow/orange. Presented results are from registering with full surface data (blue/yellow) and sparse surface data (grey/orange).

Distributions of the volumetric overlap (represented by PPV) resulting from the rigid registration and deformation correction methods using full and sparse surface data are presented in Fig. V.5 in blue/yellow (full data) and grey/orange (partial data) respectively. Average PPV results from driving the registrations with full surface, sparse surface, and resampled sparse surface data are presented for both methods of registration in Table V.II. Fig. V.6 presents the PPV plotted as a function of the average TRE for the corresponding ablation antenna for each method of registration as well as for the perfectly localized model (i.e. TRE of 0 mm). Results depicted in Fig. V.6 are from driving the registration methods with full surface data.

Table V.II. Average and standard deviation volumetric overlap are presented as the positive predictive value for each source of surface data and each evaluated method of registration. Additionally, the positive predictive value is presented for the case of perfect localization to distinguish model error from registration error.

	Average Positive Predictive Value [%]	
Surface Data	Rigid registration	Deformation Correction
Full	67.0 ± 11.8	85.6 ± 5.0
Sparse	64.8 ± 12.4	77.1 ± 8.0
Resampled	69 ± 11.1	75.1 ± 6.5
Perfect Localization	96.3 ± 0.3	

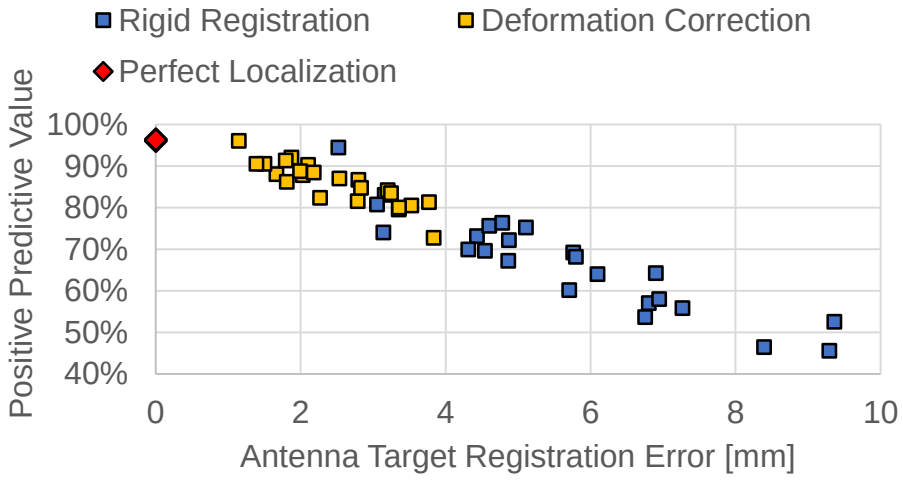

Fig. V.6. The positive predictive value is presented for each registered ablation (24 total) as a function of the average target registration of the corresponding ablation antenna. Antenna TRE was calculated as the average error of the antenna tip, insertion point, and ablation centroid. Results of the rigid registration method of Clements et al. [42] are presented in blue and the deformation correction method of Heiselman et al. [61] are presented in yellow. MWA model results in the condition of perfect registration (manual alignment) are presented for comparison in red. Presented results are from registering with full surface data.

Fig. V.7 presents an example of the retrospective ablation model following rigid registration and deformation correction using sparse anterior surface data. In each panel, the green ellipse and line represent the ground truth ablation zone and antenna pose respectively. The modeled ablation zone following rigid registration is presented in (A) and magnified in (B). The MWA model result following deformation correction is presented in (C) and magnified in (D).

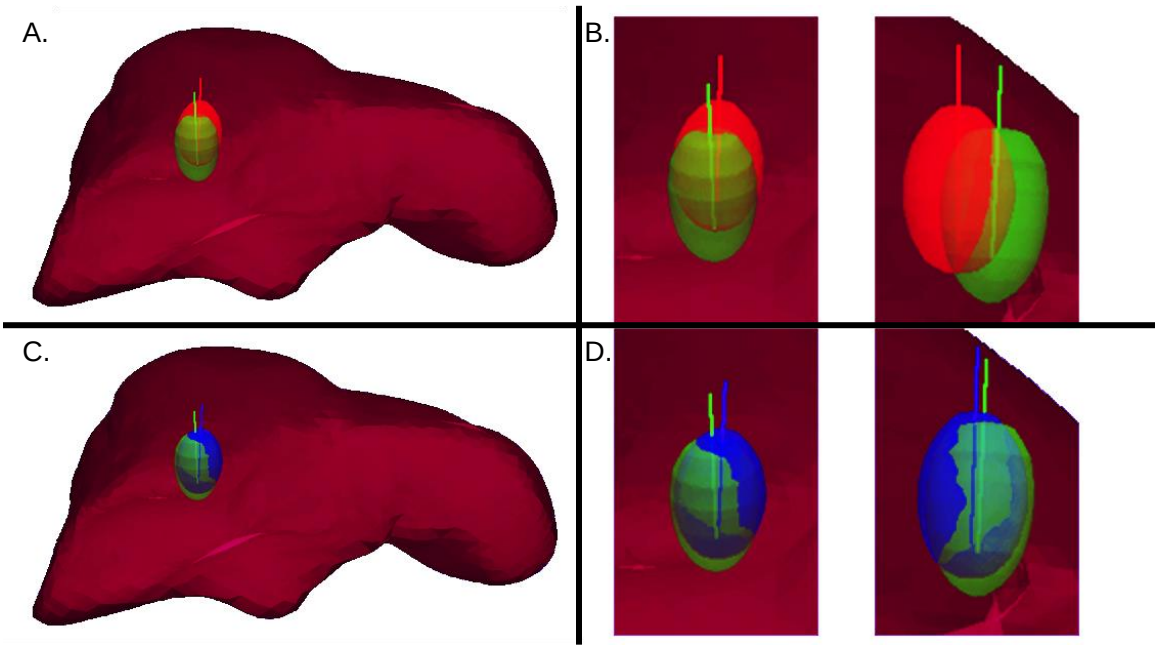

Fig. V.7. An example of ablation model predictions following registration with sparse anterior surface data. In each panel, green represents the ground truth ablation zone as observed in MRI. The rigidly registered ablation model is presented in (A) and detailed views in (B). The registered ablation model following deformation correction is presented in (C) and detailed views in (D). Additionally, in each panel the registered ablation antennas are indicated by lines with color corresponding to the registration method.

V.2.4 Discussion

In this study, we presented the first effort to evaluate deformation correction methods for image-guided microwave ablation in the liver. Further, we coupled retrospective

modeling of the ablation procedure with these surgical navigation techniques, allowing us to quantify the magnitude of error that would be associated with a combined modeling and surgical navigation approach. We evaluated these methods within a deformable hepatic ablation phantom which allows for comprehensive validation with both individual point targets and volumetric overlap of predicted and ground-truth ablation zones. To our knowledge, this combined evaluation is a unique contribution to the literature.

The example visualization of the rigid registration and deformation correction algorithms on ablation antenna positioning (Fig. V.7) indicate that the deformation correction method provides considerable improvement to the rigid registration approach when soft-tissue deformation is present. In addition, the quantitative results of the ablation antenna point target errors (Fig. V.4 and Table V.I) indicate that the deformation correction algorithm of [61] represents a significant improvement over the rigid registration results of [42] ($p < .001$). Furthermore, the point target errors presented in Fig. V.4 and Table V.I demonstrate that a more complete source of surface data (e.g. using the full surface data often available in IS) for driving the registration provides further improvement to the deformation correction algorithm when compared to the sparse surface driving data that is available in the OR ($p < .001$). It is also interesting to note that the source of surface data had much more profound impact on the deformation correction method than on the rigid registration. This observation qualitatively represents the degree to which soft-tissue deformation impacts the maximum achievable accuracy of rigid registration approaches.

In addition to reporting the antenna point target errors in Fig. V.4 and Table V.I, the volumetric error associated with the retrospectively modeled ablation zones have been presented in Fig. V.5 and Table V.II. Again, these results demonstrate improved localization by our deformation-corrected method and Fig. V.7 visualizes clearly better fidelity when

comparing the overlap of the red ablation on ground truth green (rigid registration) to that of the overlap of the blue ablation on the same ground truth (deformation corrected). As with the point target errors, we see that for each data source (Table V.II) the deformation correction method of [61] significantly outperforms the rigid alignment method of [42] ($p < .001$).

Fig. V.3 and Table V.II present the maximum volumetric accuracy of the retrospective ablation modeling utilized within this study under the condition of perfect localization. Furthermore, Fig. V.6 presents these results in comparison to the modeled ablation zones following registration. These novel results represent the decline in model-predictive capacity (-5.95% / mm, $p < .001$, $r = .93$) that is associated with localization error in a combined surgical navigation and modeling framework.

This study is not without its limitations. In this investigation we employ an inverse-model approach to reconstruct phantom-specific properties to retrospectively model the ablation outcome, which limits its immediate clinical applicability. However, there is precedence for determining disease state and approximating tissue properties from preoperative imaging using MRI [86] or ultrasound [87]. Another limitation is that neither the phantom nor the retrospective model include tissue perfusion which has been shown to have an impact on ablation outcome clinically [79-83] but is difficult to achieve in a phantom setting. We also note that the relatively low rigid registration results achieved in this study, as compared to prior phantom studies, indicate that the degree of applied soft-tissue deformation was less than previously achieved such as in [60]. This is in large part due to the nature of the agar-albumin phantom which is prone to shearing when subjected to large deformations. However, we suggest that the 20-30 mm of deformation that was achieved in this study was adequate for understanding the relative performance under assumptions of

rigid versus nonrigid deformation-corrected alignment. Furthermore, the sparse data resampled results showed improvement to the rigid registration method. However, this was not the case for the deformation correction methods. This is largely because the simulated sparse surface data did not include digitization noise (i.e. the sparse surface data was selected directly from the MRI surface) which the resampled method was specifically designed to reduce.

In summary, our results suggest that this application is a significant advancement in the field of hepatic image-guided ablation, as soft-tissue deformation is a considerable limitation to current rigid registration-based approaches. While EM-iUS methods [48-49] take a purely intraoperative imaging approach to this soft-tissue deformation problem, they fail to provide additional information concerning relevant critical anatomy, a common desire given the availability of preoperative imaging data. Furthermore, EM-iUS approaches are restricted to US-visible tumors, which further restricts its applicability to image-guided ablation when considering non-echogenic tumors that present due to disease state or following neoadjuvant therapy [52-54]. Other studies have reported targeting accuracy of ablation antennas on the order of 5 – 10 mm, with the current best being a median accuracy of 4.2 mm [49]. In comparison, our presented method of deformation correction has produced favorable accuracies of 2.5 ± 1.1 mm and 3.7 ± 1.4 mm when using full (IS) and sparse (OR) surface data respectively.

V.2.5 Conclusions

The objective of this work was to quantify the localization and volumetric accuracy of a model-based deformation correction method when applied to image-guided hepatic MWA. Evaluation of the applied method shows significant improvement in

localization accuracy when compared to a clinically-relevant rigid registration approach. Furthermore, we incorporate a retrospective model of MWA into the navigational framework, providing an important evaluation of the interplay between localization accuracy and volumetric overlap of predicted and ground-truth ablation zones. While future work is necessary to apply this modeling and navigational framework as a prospective, targeting approach, the deformation correction method applied in this study is certainly an advancement toward improved localization in hepatic MWA procedures. Going further, this work extends the concept of 'model correction' to include a new biophysical domain, namely the deposition of ablative energy, and its corresponding thermal evolution. This combined mechanics/energy framework represents a first study in a more comprehensive model-predictive paradigm for an important image-guided therapeutic process in use today.

Chapter VI

Image Data-Driven Prospective Microwave Ablation Model

VI.1 Summary and Contributions

To date, predictive models of MWA have largely been evaluated within ex vivo bovine tissue samples. As such, these studies have assumed that material properties remain consistent across specimens and have recently taken an approach which emphasizes how this baseline property set changes during a procedure as a function of temperature. However, it is likely a poor assumption that material properties remain constant across patients, especially when considering the vast array of organ disease states that can present clinically. Accordingly, this study presents the first approach for approximating patient-specific baseline material properties from a priori knowledge of organ disease state.

In this work, a prospective implementation of the best-fit microwave ablation model introduced in the previous chapter was developed. This model was initially deployed within an inverse modeling framework to determine the thermal and electrical conductivities of a series of ablation phantoms based on observations of ablation extent and verified by comparing model-predicted and observed procedural temperature measurements. After verifying the application of the inverse model for reconstructing phantom material properties, the inverse model was used to construct a model of these phantom material properties as a function of phantom fat content in a separate series of phantoms with varying levels of added fat. In this second series of phantoms, the phantom fat content was measured with a clinically-relevant quantitative MRI imaging sequence. Next, a leave-one-out validation study was performed to evaluate the predictive capacity of the constructed

material property model by comparing the model-predicted ablation zones to their ground truth counterparts. This work demonstrates, as a proof of concept, that physical modeling parameters can be linked with quantitative medical imaging to improve the utility of procedural modeling for hepatic MWA.

VI.2 Toward image-data driven predictive modeling for guiding thermal ablative therapy

The work in this chapter appears in:

J.A. Collins, J.S. Heiselman, L.W. Clements, J.A. Weis, D.B. Brown, and M.I. Miga, "Toward image-data driven predictive modeling for guiding thermal ablative therapy," *IEEE T Med Imaging*. In submission.

Abstract

Accurate prospective modeling of microwave ablation procedures can provide powerful planning and navigational information to physicians. However, patient-specific tissue properties are generally unavailable and often vary based on factors such as relative perfusion and state of disease. Therefore, a need exists for modeling frameworks that account for variations in tissue properties. In this study, we establish an inverse modeling framework to reconstruct a set of tissue properties that best fit the model-predicted and observed ablation zone contours in a series of phantoms of varying fat content. We then create a model of these tissue properties as a function of fat content and perform a comprehensive leave-one-out evaluation of the predictive property model. Furthermore, we validate the inverse-model predictions in a separate series of phantoms that include co-recorded temperature data. This model-based approach yielded thermal profiles in close agreement with experimental measurements in the series of validation phantoms (average root-mean-square error of 4.8 K). The model-predicted ablation zones showed compelling overlap with observed ablations in both the series of validation phantoms (93.4 ± 2.2%) and the leave-one-out cross validation study (86.6 ± 5.3%). These results demonstrate an average improvement of 17.3% in ablation zone overlap when comparing the presented property-model to the predicted properties based

on phantom component volume fractions. In summary, these results demonstrate accurate model-predicted temperatures and ablation zones based on image-driven determination of tissue properties. The work demonstrates, as a proof of concept, that physical modeling parameters can be linked with quantitative medical imaging to improve the utility of predictive procedural modeling for MWA.

VI.2.1 Introduction

Thermal ablation techniques have become a viable treatment approach in the management of anatomically non-resectable liver malignancies [18-20]. While many ablation modalities exist, microwave ablation (MWA) has had considerably increased interest for hepatic procedures in recent years over its counterparts. The most notable benefits when comparing to the main competing modality, radiofrequency ablation, are that MWA creates a large spatial extent of power distribution, can penetrate through charred tissues, and has the capacity to ablate up to and around large vessels [21-22, 31, 137].

Regarding performance, the success of a complete ablation with acceptable margins is heavily reliant on accurate planning and guidance. Ablation procedures are often performed using image guidance to assist in probe placement, intraoperative localization of the target, and for postoperative evaluation of the ablated necrotic zone. When using traditional methods of guidance such as ultrasound and computed tomography (CT), the ability to monitor thermal lesion development throughout the procedure is significantly limited [38]. Methods using MR thermometry have generated considerable interest although challenges of MR-compatibility, availability, and considerable cost exist [138]. Patient-specific predictive modeling of ablation procedures has been proposed to improve treatment planning as an alternative to direct thermal monitoring [139].

For ablation procedural planning, MWA device manufacturers currently provide 2D specifications for generating expected ablation volumes given specific power and time settings. These estimates are empirically derived from ablations observed within *ex vivo* animal tissue. In doing so, these models ignore the influence of patient-specific anatomical variation, tissue heterogeneity, and tissue perfusion. As a result, the manufacturer specifications are often larger and more uniform than clinically observed ablations [65-66]. Moreover, there is often no integration of these 2D predictions with the 3D patient images, placing burden on the physician to mentally reconstruct and compare complex volumes. The development of clinically accurate, patient-specific computational models of MWA procedures presents a powerful alternative to the ablation zone estimates provided by manufacturers and a lower-cost, less cumbersome alternative to interventional imaging strategies.

Computational models of MWA employ numerical methods to solve the differential equations governing electromagnetic wave propagation, power deposition, and biological heat transfer and have been investigated within the literature for two distinct purposes: (1) assisting the optimization of ablation hardware design [67-71] and (2) more recently towards the eventual development of patient-specific treatment planning [72-76]. For clinical application, research into these approaches seeks to provide more accurate and reliable estimates of personalized procedures for the purposes of planning, guidance, and assessment. When considering the shortcomings of the manufacturer provided charts, computational models tailored to an individual could incorporate specifications for geometric, dielectric, and thermal properties of the tissue. Sensitivity studies performed on models of 2.45 GHz MWA have reflected the extensive influence that these tissue properties have on MWA models, especially the dielectric properties, specific heat, and the rate of

blood perfusion when present [77-78]. Recent studies at both 915 MHz and 2.45 GHz frequencies have incorporated tissue properties that vary as a function of temperature as derived from experimental measurements [74-76] or due to dynamic changes in tissue water content and blood perfusion [79-83]. However, an inherent shortcoming in these models is that they neglect the variation in material properties that can occur between patients. A recent study in MWA antenna design concluded that there is a need for more accurate and comprehensive modeling of dielectric and thermal tissue properties [71]. Presently, patient-specific dielectric and thermal properties are generally unavailable in a clinical setting. As such, these various models of tissue properties are often derived from experimental conditions in animal tissue. Furthermore, there is clear variation between patients presenting with other common disease states such as cirrhosis or fatty liver disease [84-85]. Therefore, a need exists for modeling frameworks that account for patient-specific variations in the state of organ tissue. One possibility is to use MRI methods to non-invasively measure quantities that could be correlated to material property changes, e.g. quantification of varying liver fat content [86] may determine dielectric properties. We propose that *a priori* knowledge of organ disease state can be used to facilitate predictive modeling of thermal ablation.

In this work, we propose a novel approach to modeling microwave ablation procedures that uses quantitative medical imaging to estimate the dielectric and thermal properties of tissue. The paper begins with the development of a methodology to determine thermal and electrical tissue material properties from an inverse modeling approach and reports the fidelity of those predictions within the context of temperature measurements. Once achieved, in a separate series of phantoms with varying fat content, material properties were determined via the inverse modeling approach. These reconstructed properties were then fit to a material property model as a function of phantom fat content, as measured with

a clinically-relevant MRI fat quantification imaging sequence. A leave-one-out cross validation study was then performed which used the constructed material property model to estimate phantom material properties in a prospective implementation of the ablation model. The model-predicted ablation zones were then compared to their observed gross histology counterparts for validation purposes. The material property model developed in this study specifically focused on phantom fat content because it was easily controllable and quantifiable for the purposes of this proof of concept study and remains clinically-relevant when looking at common patient presentations [86]. However, we note that there are additional quantitative medical imaging methods that could complement this work (e.g. electrical conductivity imaging [140]).

VI.2.2 Methods

The objective of this study is to develop a predictive modeling framework for hepatic MWA that estimates tissue properties based on quantitative medical imaging of fat content to better account for patient-specific property variation and more accurately predict ablation outcome prior to treatment. In this work, we present a rigorous proof-of-concept to begin to determine the fidelity of such an approach for therapeutic intervention technologies. The following subsections detail the methods used to collect experimental phantom data (VI.2.2.1-3), develop our MWA model (VI.2.2.4-7), and experimentally validate our MWA model and phantom property models (VI.2.2.8-9).

VI.2.2.1 Phantom Testing Environment

For this study, a heat-sensitive gel phantom was constructed consisting of liquid egg whites, vegetable shortening, and the remainder with agar gel. Egg whites consist of

approximately 90% water and 10% dissolved protein. The denaturing of ovalbumin protein within the egg whites provides a visualization of thermal damage within the phantom. Thermal denaturation of the protein causes aggregation, leading to optical scattering. This denaturation causes the thermal lesion to be clearly visible when prepared in mock histology. Vegetable shortening was used to introduce a controllable variability to the thermal and electrical properties of the phantom. Table VI.I demonstrates the general reduction in thermal and electrical properties of vegetable shortening compared to the other phantom components. The ranges of fat included within this study were chosen to represent the clinical presentation of fatty liver disease (i.e. 5-10% of liver weight).

Table VI.I. Dielectric and thermal properties of the agar-albumin-fat phantom components as reported in the literature.

	Agar-albumin Phantom		
	Agar-water gel (1.5%)	Vegetable Shortening	Liquid Egg Whites
σ [S/m]	0.05 – 0.4 [141]	1.04×10^{-5} [145]	1 [149]
ε	67 – 84 [142]	2.53 – 2.665 [146]	50.2 [149]
c [J/Kg-K]	3900 [143]	1670 [147]	3414 [150]
k [W/m-K]	0.5 – 0.55 [144]	0.155 – 0.170 [148]	0.522 [150]

To make this agar-albumin-fat phantom, 1.5 wt% agar powder (Thermo Fisher Scientific, Waltham, MA) was mixed with an appropriate volume of purified water. The solution was then heated gradually until boiling on a hot plate while being continuously stirred. After the agar gel had exceeded 60°C, the desired amount of vegetable shortening was introduced (Crisco, The J.M. Smucker Company, Orrville, OH). Once heated, the solution was then cooled below 55°C with continuous stirring, at which point 50 wt% liquid egg white (Break Free Liquid Egg Whites, The Kroger Company, Cincinnati, OH) was added and mixed thoroughly for 1 minute. The mixture was then poured into the phantom mold and began to solidify once cooled below 35°C. Note that the liquid egg white solution must

be added when the temperature of the agar gel is below 60°C to avoid prematurely denaturing the ovalbumin protein.

A cubic acrylic box with a volume of 1L served as both the phantom mold and enclosure during the ablation procedures. The lid to the enclosure incorporated a series of holes, centered 5 mm apart, along the midline of the phantom to enforce consistent placement of the ablation antenna and, if present, temperature sensors. During each experiment, the ablation and temperature sensors were positioned within the phantom using these guides and rigidly fixed in position at measured depths.

In total, 6 agar-albumin phantoms with no fat were created for the inverse model validation study (section VI.2.2.8) and 15 agar-albumin-fat phantoms of varying fat percentages were created for the phantom material property model study (section VI.2.2.9).

VI.2.2.2 Ablation Data Collection

As depicted in Fig. VI.1, a 915 MHz Perseon ST microwave ablation antenna was inserted into the center of each phantom to a recorded depth. For the no-fat phantoms, two two-channel Luxtron 812 (LumaSense technologies, Santa Clara, CA) fiber optic temperature sensors in conjunction with 4 STB fiberoptic probes were used to record temperatures at a rate of 2 samples per second and in the range of 0 to 120°C. The system is reported to be accurate within ± 0.5°C and is immune to interference from radiofrequency, microwave, and electromagnetic induction. Continuous power of 60 W was applied for 15 minutes (MicroThermX, Perseon Medical, Salt Lake City, UT). Finally, mock histology was attained by sectioning the phantom along the midline of the MWA antenna. A 2D representation of the ablation zone was then segmented from a photograph (Fig. VI.2). Measurements of the transverse and axial extents of each ablation zone were taken from the

segmented mock gross histology.

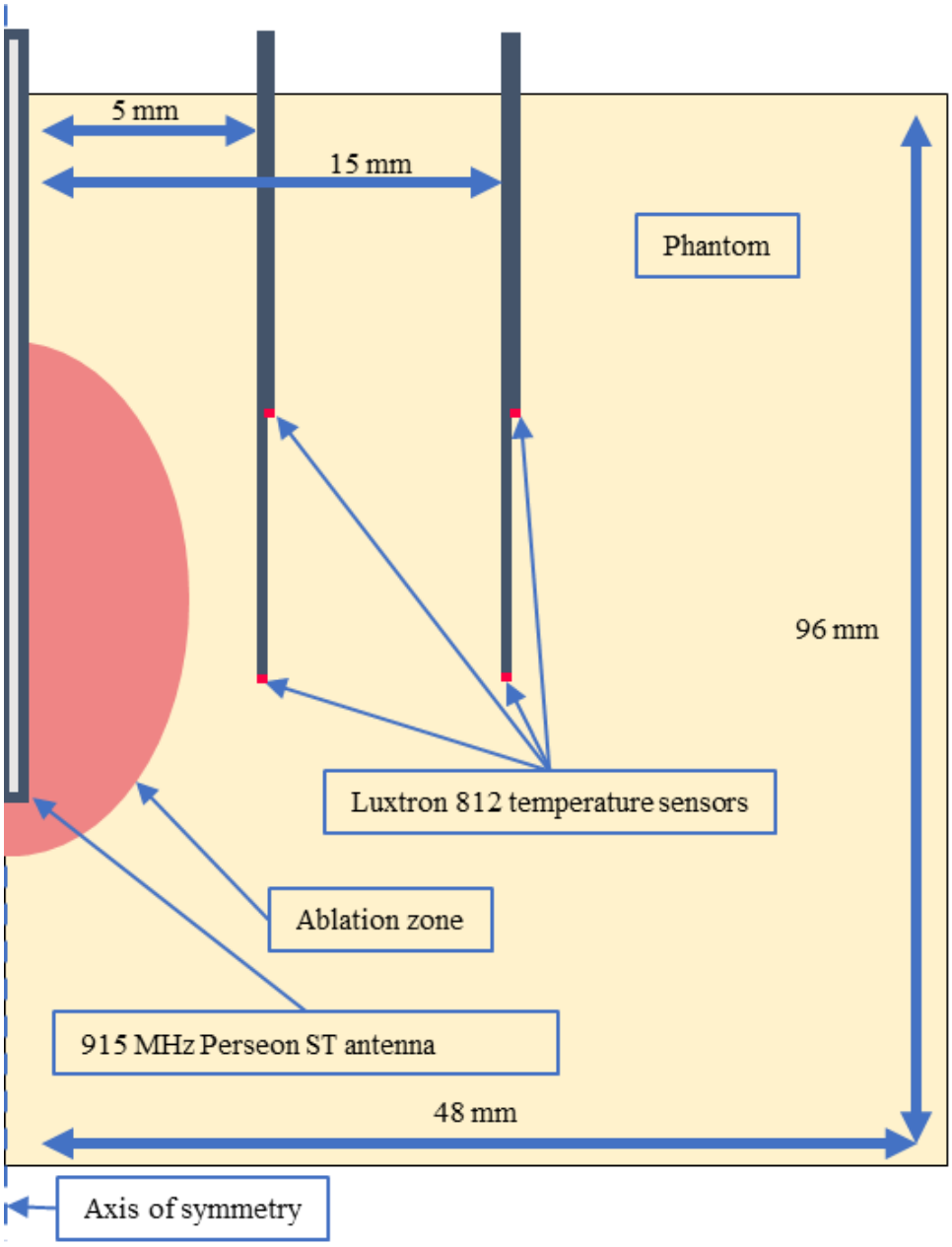

Fig. VI.1. Diagram of the experimental setup and model geometry for ablation with the Perseon ST microwave ablation antenna within an agar-albumin phantom.

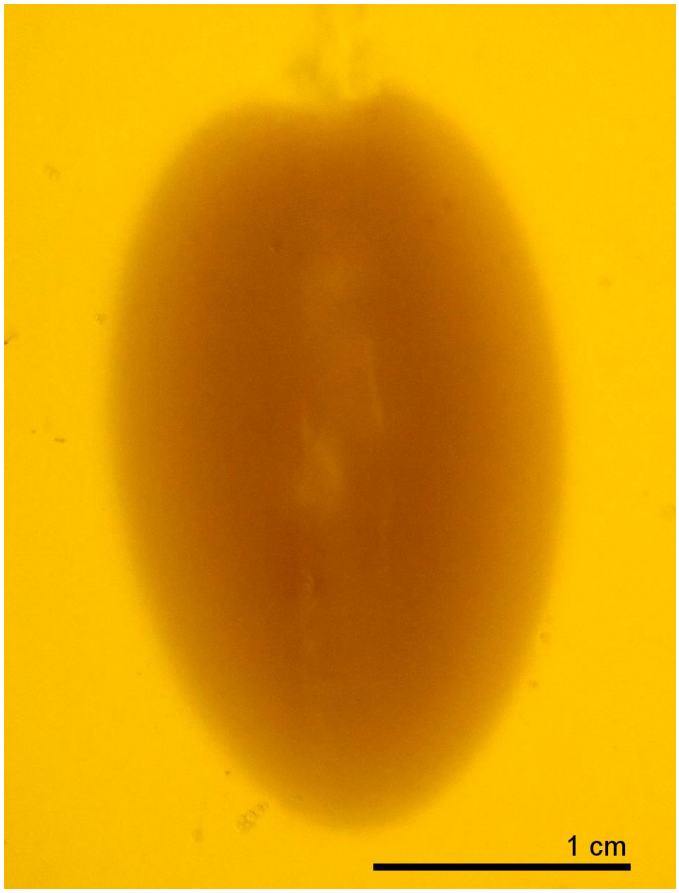

Fig. VI.2. Sample backlit mock histology of ablation zone (cut along the axis of the Perseon ST antenna) following an ablation at 60 W for 15 minutes in an agar-albumin phantom.

VI.2.2.3 MRI Fat Quantification

MRI examination of each phantom was achieved with a 3T Intera Achieva MR scanner (Philips Healthcare, Netherlands). Following ablation, a commercially available fat quantification sequence (mDixon Quant) was used to acquire fat fraction images of each of the 15 phantoms for the phantom material property model study (Philips Healthcare, Netherlands). The mDixon Quant fat quantification protocol has a reported accuracy of ± 3.5% and reproducibility of ± 1.4% [151]. For each phantom, 53 slices were acquired with

3.12 mm spacing and in-plane resolution of 1.56 × 1.56 mm.

VI.2.2.4 Computational Model

We implemented a 2D axially-symmetric finite element model using COMSOL Multiphysics (COMSOL Inc, Burlington, MA) and Matlab 2017b (The Mathworks Inc, Natick, MA) to simulate electromagnetic wave propagation and heat transfer in an agar-albumin phantom with the 915 MHz Perseon Short-tip (ST) antenna (Perseon Medical, Salt Lake City, UT). The development and absorption of electromagnetic waves radiating from the antenna within the phantom, when assuming no initial existing charge, is described by the electromagnetic wave equation.

$$(\nabla^2 + \omega^2 \mu \varepsilon_c)\vec{E} = 0 \qquad \text{Eq. VI.1}$$

where ω [rad/s] is the angular frequency of the electromagnetic wave, μ [H/m] is the permeability, ε_c is the complex permittivity, and $\vec{E}$ [V/m] is the electric field strength. Heat transfer and the resulting temperature history were solved using Pennes' bioheat equation.

$$\rho c \frac{\partial T}{\partial t} = \nabla \cdot k \nabla T + Q - Q_p + Q_m \qquad \text{Eq. VI.2}$$

where ρ [kg/m^3] is mass density, c [J/kg·K] is specific heat capacity, k [W/m·K] is thermal conductivity, T [K] is temperature, Q [W/m^3] is heat generation due to absorbed electromagnetic energy, Q_p [W/m^3] is heat loss due to perfusion, and Q_m [W/m^3] is metabolic heat generation. Metabolic heat generation (Q_m) and perfusion (Q_p) were not present within the phantom and were therefore excluded from the model. Heat generation from power deposition by the applied electric field was calculated by

$$Q = \frac{1}{2}\sigma \|E\|^2 \qquad \text{Eq. VI.3}$$

where σ [S/m] is the electrical conductivity.

VI.2.2.5 Boundary Conditions

A first order electromagnetic scattering condition was applied to the exterior of the phantom to limit the reflection of outgoing waves by simulating a transparent boundary.

$$\vec{n} \times \left(\nabla \times \vec{E}\right) - jk\vec{n} \times \left(\vec{E} \times \vec{n}\right) = 0 \qquad \text{Eq. VI.4}$$

where $\vec{n}$ is the direction normal to the boundary and k is the wave number. Boundaries along the exterior of the phantom were set to a fixed room temperature (20 [°C]). Saline cooling of the Perseon ST antenna was simulated as a convective heat flux condition along the inner boundary of the antenna as follows

$$\vec{n} \cdot (-k\nabla T) = h \cdot (T - T_{ext}) \qquad \text{Eq. VI.5}$$

where $\vec{n}$ is the normal vector to the element, k [W/m·K] is the thermal conductivity, h [W/m^2·K] is the heat transfer coefficient, T [K] is temperature, and T_{ext} is the saline temperature (20 [°C]).

VI.2.2.6 Modeling Tissue Damage

Thermally-induced tissue damage is a function of both instantaneous temperature and thermal history. For this study, the Arrhenius damage integral was used to estimate protein denaturation as a proxy to cell death within the phantom [152]. The degree of damage in tissue experiencing hyperthermia was calculated from

$$\alpha = \int_0^t A exp\left(-\frac{E_a}{RT(t)}\right) dt \qquad \text{Eq. VI.6}$$

where α is the degree of damage at a given time, A [1/s] is the frequency factor, E_a [J/mol] is the activation energy required to damage the mock tissue, R [J/mol·K] is the universal gas constant, and $T(t)$ [K] is the temperature history of the mock tissue. The parameters E_a (2.8819×10^5 [J/mol]) and A (1.8769×10^{41} [1/s]) are mock tissue dependent and were

calibrated to maximize correspondence between thermal history and ablation zone contour fit in the validation phantom set. The fraction of damaged tissue was then determined by

$$\theta_d = 1 - e^{-\alpha} \quad \text{Eq. VI.7}$$

VI.2.2.7 Discretization

The ablation antenna and temperature sensor locations (when present) within the phantom were recorded in each experiment and incorporated into the model geometry as presented in Fig. VI.1. Four temperature sensors were used to record thermal history in each experiment of the validation phantom set with two pairs located at 5 and 15 mm transversely at varying recorded depths (observe the 4 sensor locations in Fig. VI.1). These locations were added within the model geometry to allow for direct comparison between model-predicted and observed temperatures at a given time. The model was discretized as a free triangular mesh with maximum element sizes of 0.15 and 2 mm for the antenna and phantom respectively. An implicit multifrontal massively parallel sparse direct solver (MUMPS) within COMSOL Multiphysics was used to solve both the stationary electromagnetic and transient bioheat transfer problems [153-154]. The model was solved with a continuous input power of 60 W and frequency of 915 MHz at 15 s time steps to the final solution at 15 min.

VI.2.2.8 Model Validation Study

To evaluate the fidelity of our model accuracy, a series of 6 agar-albumin phantoms with no fat were created and ablation and thermal history data were collected as described in sections VI.2.2.1-2. The MWA model described in sections VI.2.2.4-7 was then employed in an inverse fashion to determine a set of phantom electrical and thermal properties which best match the model-predicted ablation zone to the observed ablation zone

(Fig. VI.3). The thermal history data collected in each case were then compared to the model-predicted temperatures at those locations to validate the accuracy of the proposed phantom property reconstruction method.

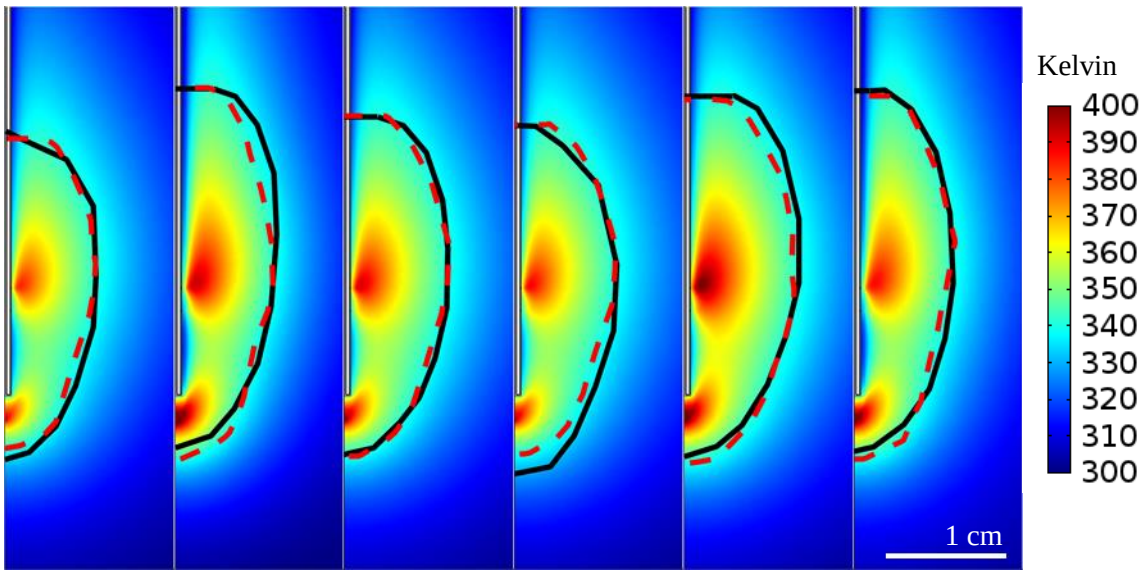

Fig. VI.3. Model-predicted temperature maps, observed (solid black line), and model-predicted (red dashed line) ablation zones are presented for each case of ablation with the Perseon ST antenna at 60 W for 15 minutes within the base agar-albumin phantom used for the model validation study. The observed ablation zone contour was collected from mock-histology and used to drive the inverse MWA model.

Properties defining the electrical and thermal behavior of the phantom were reconstructed by deploying the MWA model within a nonlinear optimization scheme. This inverse modeling approach iteratively selected values for a parameter set, Eq. VI.8, to maximize the overlap between the observed ablation zone and the result of the model (as the Jaccard similarity coefficient, Eq. VI.9-10).

$$P = [\sigma, k] \qquad \text{Eq. VI.8}$$

In Eq. VI.8, σ and k are the electrical and thermal conductivities respectively. These properties were selected for our model as they directly proportional to the electrical and thermal contributions to the bioheat equation (Eq. VI.2-3). Initial values for the parameter set, as well as other properties used in the model but not reconstructed in the optimization,

were estimated to be the average weighted linear combination of the corresponding phantom components across the phantom data set (Table VI.I).

The degree of overlap between the observed and model-predicted ablations was quantified by the Jaccard similarity coefficient and used to define the objective function in the optimization. First, binary masks representing the true and model-predicted ablation zones were generated. Given these masked images, the number of pixels in the model-predicted ablation zone overlapping with the observed ablation zone (N_{TP}), the number of voxels in the model-predicted ablation zone which did not overlap with the observed ablation zone (N_{FP}), and the number of voxels in the observed ablation zone which did not overlap with the model-predicted ablation zone (N_{FN}) were used to calculate the similarity metric:

$$\text{Jaccard} = \frac{N_{TP}}{N_{TP} + N_{FP} + N_{FN}} \quad \text{Eq. VI.9}$$

The Jaccard similarity metric ranges from 0 (no overlap) to 1 (perfect match). Therefore, the objective function for the optimization was as follows:

$$\Omega = 1 - Jaccard \quad \text{Eq. VI.10}$$

The Nelder-Mead downhill simplex algorithm was used to optimize the parameter set for each phantom based on the minimization of the objective function in Eq. VI.10 [154-155]. The algorithm uses a direct search method to solve multidimensional unconstrained problems without requiring derivative information. Therefore, the approach can handle non-smooth or noisy objective functions but can take many iterations to converge. The search algorithm was employed until a minimum first-order optimality measure of 0.01 was reached.

VI.2.2.9 Phantom Property Model Study

The goal of the above validation study was to validate that our inverse modeling

strategy coupled to quantitative ablative data could be used to determine material properties. The objective of the phantom material property model study was to use that methodology to develop a functional model relating quantitative MR imaging to physical ablation modeling parameters. To accomplish this, a model of phantom material properties as a function of phantom fat content (measured by the quantitative MR fat imaging protocol described in section VI.2.2.3) was constructed using the previously described inverse modeling strategy.

Next, a leave-one-out cross validation study was performed to characterize this model of phantom material properties as a function of MR-measured fat content. This was achieved by holding out one phantom experiment from the 15 agar-albumin phantoms of varying fat content and using optimized property values from the remaining 14 phantoms to create a linear regression model. The held-out data was then prospectively evaluated to quantify predictive accuracy. Cycling through each data set as a target provides a measure of the predictive capability of the image data-driven material property model. As before, the model-predictive accuracy was calculated using the Jaccard similarity metric (Eq. VI.9).

VI.2.3 Results

VI.2.3.1 Model Validation Study

Model-predicted temperature maps for each of the 6 agar-albumin ablation phantoms included in the model validation experiment are presented in Fig. VI.3 alongside contours defining the observed and model-predicted ablation zone extents (as black and dashed red lines respectively). The degree of ablation zone overlap is presented in Table VI.II as the Jaccard similarity coefficient (averaging 93.4 ± 2.2%). The average observed transverse and axial dimensions attained from mock histology following ablation were 18.2 ± 1.4 mm and

31.0 ± 1.2 mm respectively. Modeled ablation zone diameters differed from observed diameters by 3.3% on average while lengths differed by an average of 3.5%. Additionally, the reconstructed phantom properties are presented in Table VI.III.

Table VI.II. Jaccard similarity coefficients representing the overlap between the observed and model-predicted ablation zones and root mean square temperature error for each experimental case.

Case #	Agar-albumin Phantom	
	Jaccard similarity coefficient (%)	Root-mean-square temperature error (K)
1	95.1	4.1
2	90.9	4.8
3	96.1	4.2
4	90.6	4.3
5	93.5	5.8
6	94.3	5.6
Average	93.4 ± 2.2	4.8

Table VI.III. Optimized electrical and thermal conductivities for each experimental case of the base agar-albumin phantom in the model validation study.

Case #	Agar-albumin Phantom	
	Electrical conductivity (σ [S/m])	Thermal conductivity (k [W/m-K])
1	0.57	0.67
2	0.44	0.34
3	0.58	0.62
4	0.58	0.67
5	0.54	0.47
6	0.50	0.62
Average	0.53 ± 0.05	0.56 ± 0.13

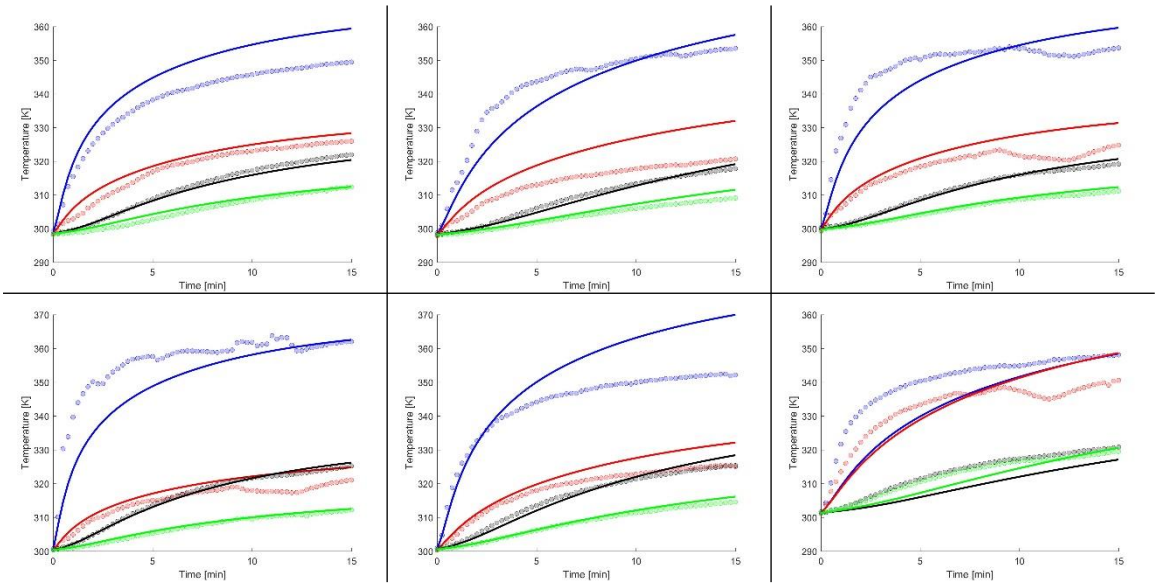

Fig. VI.4. Observed and model-predicted temperatures as a function of time for the base agar-albumin phantom. Observed temperatures at the four sensor locations are represented by markers while model-predicted temperatures are represented by solid lines of corresponding color.

Fig. VI.4 presents the thermal history observations for each temperature sensor in each phantom in the model validation experiment compared to the model-predicted temperatures at those locations presented as markers and lines respectively. The average root-mean-square (RMS) error with respect to the observed and model-predicted temperatures for each phantom are presented in Table VI.II (averaging 4.8 K).

VI.2.3.2 Phantom Property Model Study

The optimized and property-model-predicted values of electrical and thermal conductivity are presented as orange and blue markers respectively in Fig. VI.5. The orange dashed line represents a linear fit to the full set of 15 optimized properties as a function of measured fat content. The values of electrical ($p > .05$, $r = -.32$) and thermal conductivity ($p < .05$, $r = -.76$) were found to decrease with fat content at rates of 0.74% and 2.61% respectively.

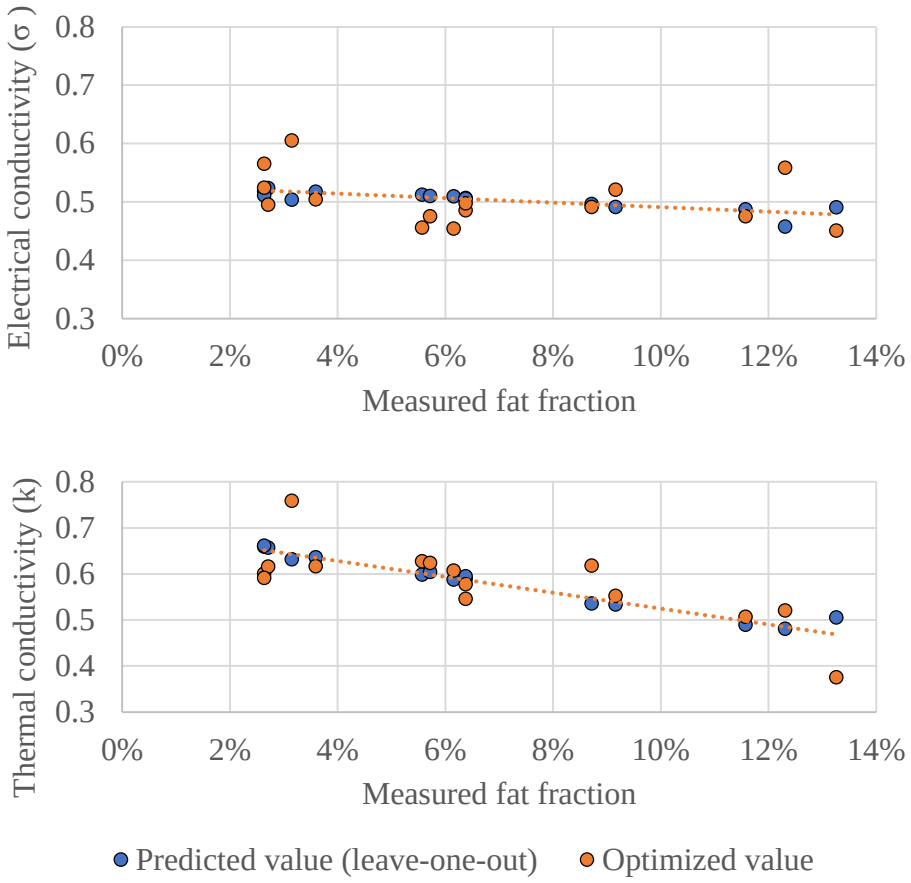

Fig. VI.5. Determined values of electrical conductivity and thermal conductivity as a function of the MRI measured fat fraction for each of the 15 agar-albumin-fat phantom cases. The optimized value for a given case is represented by an orange marker. While the predicted value for each case from the leave-one-out study is presented in blue. The orange dashed line represents a linear fit to the optimized values.

Fig. VI.6 presents the percentage overlap between the modeled and observed ablation zones for the 15 agar-albumin-fat phantoms evaluated within the leave-one-out cross validation study represented by a box and whisker chart of the distributions of the Jaccard similarity coefficient. Results are presented using the optimized property values for each case in orange (averaging 90.2 ± 3.8%), the predicted property values from the leave-one-out cross validation in blue (averaging 86.6 ± 5.3%), and the estimated property values from the phantom component volume fractions (i.e. the initial guesses for the optimization) in grey (averaging 69.3 ± 9.7%).

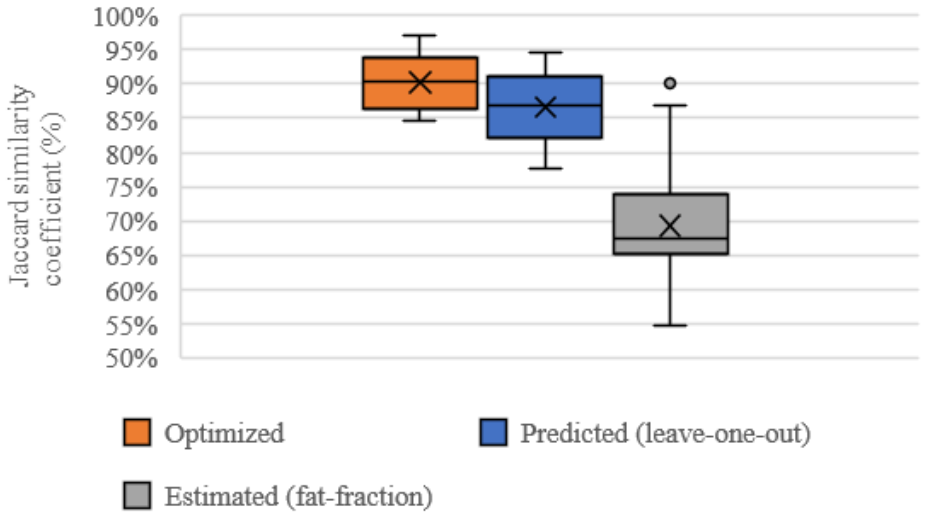

Fig. VI.6. Percentage overlap between modeled and observed ablation zones for the 15 agar-albumin-fat phantom cases represented by the Jaccard similarity coefficient. Results using the optimized (orange), leave-one-out predicted (blue), and fat-fraction estimated (grey) are presented. The box and whiskers represent the mean, median, upper and lower quartiles, outliers, maximum, and minimum Jaccard similarity coefficient from each modeling approach.

VI.2.4 Discussion

Based on the work presented in this study and in the literature, tissue thermal and electrical properties are an important factor in the development of therapeutic ablation zones and therefore play an important role in the accuracy and reproducibility of predictive MWA models [77-78, 84-85]. It is also equally apparent that these tissue properties can vary across patients and are impacted by disease state [84-85]. To date, these variations in tissue properties as a function of patient-specific conditions have been excluded from approaches to predictive modeling of thermal ablation procedures and current state-of-the-art therapeutic applications [67-76]. With this study, we presented two objectives: (1) we developed an inverse modeling approach for reconstructing phantom properties using ablation extent data and (2) we used that reconstruction approach to construct a phantom property model that was then used to predictively estimate tissue properties as a function of quantitative medical imaging of fat content. These methods were tested within an agar-albumin-fat ablation phantom and were shown to predict ablation temperatures and volumetric extent with a high degree of accuracy.

VI.2.4.1 Model Validation Study

The objective of this study was to introduce and validate the inverse modeling approach to phantom property reconstruction from ablation extent data. Ablation zone overlap measurements presented in Table VI.II and visually in Fig. VI.3 indicate a strong volumetric agreement between observed and model-predicted ablation zones in the model validation study (averaging 93.4 ± 2.2%). These results show that the inverse modeling framework was able to provide accurate prediction of the margins achieved during ablation by optimizing the phantom properties for the case of the baseline phantom (i.e. no fat

content). Further, as the maximization of the ablation zone overlap was employed as the objective function in the optimization, it is satisfying to observe a good model-fit correlation.

Of greater interest, results presented in Fig. VI.4 and Table VI.II illustrate the correspondence between the observed and model-predicted temperatures at each of the 4 temperature sensors (average RMS error 4.8 K). As these data were purely bystander, and not utilized in the optimization, the results more appropriately serve as an independent indication of the ability of the modeling framework to reconstruct phantom properties by fitting ablation zone outcomes. Analyzing heating near the active region of the antenna, within the zone of the largest electromagnetic energy deposition (which we expect to occur at the sensor represented by the blue marker/line in Fig. VI.4 for each case), we see very rapid heating within the first 5-7 minutes of the procedure which the model often under predicts before correcting by the final time point. In Eq. VI.3, electromagnetic energy deposition is proportional to the value of electrical conductivity (σ). Cases C-D in Fig. VI.4 present the greatest rate of heating out of the 6 cases, and accordingly resulted in the reconstruction of the largest values of σ (Table VI.III). Contrasting these results to the more gradual temperature profiles associated with the distant temperature sensors (red, black, and green), we observe that heating far from the ablation antenna is dominated by heat transfer rather than electromagnetic energy deposition and that model-predicted temperatures throughout the procedure are more consistent (particularly for black and green, which are the farthest sensors from the active region of the ablation antenna).

VI.2.4.2 Phantom Property Model Study

The purpose of this study was to evaluate a material property model where phantom properties were estimated based on quantitative imaging of phantom fat content

using a leave-one-out cross validation approach. Phantom properties for each of the 15 cases were determined using the property reconstruction framework outlined in the model validation study and are represented by the orange markers in Fig. VI.5. While temperature data were not present for the phantom cases evaluated, the average ablation zone overlap following optimization (90.2 ± 3.8%) was in accordance with the results presented in the model validation study. The leave-one-out cross validation evaluation of the proposed property model resulted in ablation zone overlap of an average 86.6 ± 5.3%. The estimated properties for each case in this evaluation are represented by blue markers in Fig. VI.5. Furthermore, these results represent a 17.3% increase in ablation zone overlap when compared to a separate material property model based on determining property values from the phantom component volume fractions in Table VI.I as seen in Fig. VI.6.

Based on the phantom component volume fractions, it is expected that both the electrical and thermal conductivity would decrease with the addition of fat to the phantom. This expectation was realized by the property reconstructions from our inverse model solutions (Fig. VI.5) which were used to construct the phantom property model. However, only the thermal conductivity was found to have a statistically significant relationship with fat content. Additionally, using linear regression, the ablation zone areas (from mock histology) of the agar-albumin-fat phantoms were found to significantly increase with fat content ($p<.05$, $r = .86$). These results clearly demonstrate that the addition of fat altered the behavior of the phantom and resulted in varying ablation outcome. When considering the clinical application of these results, this could have considerable impact. As an example, when one considers the links between fatty liver disease and hepatocellular carcinoma, the likelihood of patient-specific variability in material properties is high and adds credence to the proposed material property model framework [84-85]. Furthermore, we believe that the

utilization of the agar-albumin-fat phantom as a surrogate for human liver tissue in this study is adequate as the reconstructed properties are within the range presented clinically [84].

In total, 5 material properties (ρ, ε, c, σ, and k) are present within the governing equations to the model (Eq. VI.1-3). The conduction and electromagnetic energy deposition terms are the major contributing factors to the thermal solution of the model and are directly proportional to the thermal (k) and electrical (σ) conductivities respectively (i.e. the two properties reconstructed in the model). To reduce the dimensionality of the property reconstruction problem, we assume that density (ρ), relative permittivity (ε), and specific heat (c) remain constant with changes in fat content.

VI.2.4.3 Limitations

We acknowledge that the phantom work herein could be further strengthened by incorporating *in vivo* processes such as perfusion. Additionally, the current approach reconstructs homogenous steady-state properties for the phantom which could be enhanced with the introduction of nonlinear temperature-dependent representations of properties as others have investigated in the literature [74-75]. It is also important that we identify the challenges to clinical workflow that are introduced. To establish this property model approach, a significant series of clinical data would be required with nonroutine preoperative quantitative imaging to determine fat content and necessary postoperative imaging to assess ablation outcomes. Furthermore, the quantitative fat imaging will be required for any case seeking to utilize the developed property model prospectively. However, there is precedence for additional required imaging for diagnostic purposes and we suggest that the results of this study show considerable promise for the approach as well as point to potential further efforts at additional imaging that could lead to better model predictions of ablative therapy.

VI.2.5 Conclusions

The objective of this work was to develop and experimentally validate a predictive numerical model of microwave ablation procedures with the 915 MHz Perseon ST antenna where patient-specific tissue properties are estimated based on preoperative quantitative MR fat imaging. Procedures were performed in an agar-albumin-fat phantom and were validated with experimental temperature and ablation zone data. While further work is necessary to apply this method to clinical MWA treatment planning, the property model approach provided herein is an advancement toward patient-specific predictive modeling of MWA procedures.

Chapter VII

Summary and Future Directions

VII.1 Summary of Research

This dissertation presented studies that evaluated methodologies and techniques to provide enhanced treatment planning and intraoperative localization for image-guided microwave ablation of hepatic tumors. A true multiphysics framework is developed herein which utilizes patient-specific predictive procedural modeling and advanced surgical navigation methodologies for delivery. This is the first work to demonstrate a model-based therapeutic and guidance framework for hepatic microwave ablation procedures. The results of which demonstrate the feasibility of such an approach and represent a significant advancement towards a more comprehensive modeling paradigm for an important image-guided therapeutic process.

In Chapter IV, a validation framework was introduced that allows for the testing of image-to-physical registration algorithms within a series of clinically-realistic data. This human-to-phantom data framework can generate a large population of realistic registration scenarios, which enables rapid, early stage validation of registration methods in a fully characterized phantom environment while avoiding the burden of collecting such comprehensive data clinically. In addition, Chapter IV presents a surface data resampling method which was validated within the human-to-phantom data framework and was found to significantly improve registration accuracy and reproducibility.

In Chapter V, aspects of the previous human-to-phantom data framework were applied to a new deformable hepatic ablation phantom. This work evaluated the efficacy of rigid registration and model-based deformation correction methods for image-to-physical

registration in image-guided hepatic ablation procedures. In addition, a retrospective model of microwave ablation was developed and deployed within the navigational framework to assess the realistic error associated with a combined model-based therapeutic and guidance system. This work extends the concept of 'model correction' to include a new biophysical domain, namely the deposition of ablative energy and its corresponding thermal evolution. Chapter V demonstrates, in an initial phantom experiment, an advancement toward improved procedural navigation in microwave ablation procedures.

In Chapter VI, the retrospective model of MWA developed in Chapter V was further developed into a truly predictive procedural model which approximates relevant tissue properties from quantitative medical imaging of the state of organ disease (e.g. organ fat content). To date, fully predictive models of MWA have largely assumed tissue properties from empirical measurements in *ex vivo* animal tissue and have therefore ignored any anatomical or pathological differences which may present between patients. The results of this chapter demonstrate accurate model-predicted temperatures and ablation zone extents. This chapter demonstrates, as a proof of concept, that patient-specific modeling parameters can be linked with quantitative medical imaging techniques to improve the predictive capacity of procedural modeling.

VII.2 Future studies

VII.2.1 Ablation Model Improvements

The models developed in Chapters V and VI of this work make many assumptions that will not necessarily hold true when transitioning from the highly controlled phantom environment. Of particular interest are model development of perfusion and convective blood flow (e.g. larger vasculature) which have been shown to have a large influence on ablation zone morphology [81-82]. Model improvements may also be achieved by further developing the image-driven tissue property model outlined in Chapter VI. The current property model is specifically designed for use with the agar-albumin-fat phantom utilized within this work. Future work will need to address changes in phantom or tissue accordingly and ensure appropriate sample size to provide adequate statistical power.

Furthermore, the models developed within this work are 2D-axisymmetric by design and neglect patient-specific geometries. The methods used to develop patient-specific biomechanical models in Chapter III may be employed to generate patient-specific microwave ablation models. However, this transition from 2D to 3D will introduce significantly more degrees of freedom within the model and therefore considerably greater computational burden. Similarly, the work in this dissertation only addresses single ablations. It is also of interest to investigate models of serial and simultaneous ablation, as these are common clinical procedures. Simultaneous ablations are typically performed with ablation antenna aligned parallel to one another to facilitate improved power deposition. Currently, research into non-parallel antenna configurations has been limited. An accurate, 3D computational model of ablation could be used to better understand these more complex ablation scenarios.

VII.2.2 Human-to-Phantom Validation Framework

The human-to-phantom data framework introduced in Chapter IV provides a valuable early-stage validation method for sparse surface driven image-to-physical registration techniques. Further improvements to the framework can be implemented by adding additional phantom deformation experiments and clinical sparse data patterns. Furthermore, this framework can be developed into a standard for registration validation. Currently, plans are being developed to leverage this validation framework to create a sparse surface data challenge that will encourage research groups to test their IGLS methods on common data and be provided with quantitative assessment. In this challenge, teams will be provided with several common sparse surface data sets representing collection of anterior surface data from a hepatic phantom in its deformed state as well as a mesh of the phantom in an undeformed state. The teams will then be asked to align the surface data and the mesh for each case. Once achieved, the teams will be provided with TRE values based on internal targets distributed throughout the phantom.

VII.2.3 *In vivo* Validation

The phantom data used throughout this dissertation has many features which make it highly desirable from a validation perspective. However, the ultimate goal of this research should be to proceed into clinical care. Recent studies have been performed that investigate the application of IGLS methods for open hepatic resection in [62, 64]. A similar study to those of [46, 62] would provide ablation antenna tracking data and could attain ground-truth ablation extent data from postoperative imaging. This clinical data would allow for the retrospective analysis of the microwave ablation model by comparing the model solution in the registration-predicted location to that ground-truth ablation zone from imaging. This

experiment would be similar in structure to the phantom experiment of Chapter V but would require a significant effort to achieve. The data acquired in such a study would contribute to further development of the microwave ablation model (as described above) as well as a better understanding of the sensitivity of the modeling framework to more clinically-relevant localization error which is difficult to recreate in a phantom testing environment.

VII.2.4 Impact of Medical Imaging

Medical imaging currently provides a wealth of information to physicians for diagnostic and treatment selection purposes. In chapter VI, as a proof-of-concept, we further utilized medical imaging data to develop and evaluate an image data-driven predictive modeling framework for hepatic microwave ablation, a common image-guided procedure in use today. The following section will discuss the suitability of the quantitative imaging used in this dissertation as well as other potentially complimentary imaging methods for this proposed image data-driven modeling paradigm.

Nonalcoholic fatty liver disease (NAFLD) is caused by an excessive buildup of fat in the liver and can lead to nonalcoholic steatohepatitis (NASH) when inflammation and tissue damage occur. NAFLD and NASH can further lead to the scarring of liver tissue, or cirrhosis (a common comorbidity to HCC). Studies have suggested that NAFLD and NASH directly promote the development of primary hepatic cancers independent of the presence of cirrhosis [156]. Furthermore, dielectric properties relevant to predictive microwave ablation modeling have been shown to vary predictably with tissue water [157] and fat [158] content. Therefore, there is precedence for basing an ablation material property model on liver water or fat content. As previously described in this work, quantitative medical imaging (e.g. mDixon quant MRI sequence) can be used to non-invasively measure liver water and fat

content.

Tissue perfusion has also been shown to have a large impact on ablation outcome both in simulation and clinically [79-83]. Intravoxel incoherent motion (IVIM) MRI and dynamic contrast-enhanced (DCE) MRI and CT methods have been developed to estimate perfusion and blood volume in tissue. Furthermore, these methods have been utilized to monitor radiofrequency ablation procedures [159] and to quantify NAFLD [160] and cirrhosis [161]. A phantom material property model was developed in chapter VI of this work that correlated phantom properties to measurements of phantom fat content acquired with the mDixon quant MRI sequence. Accordingly, these methods of perfusion imaging have the potential to be used to provide a quantifiable alternative to fat or as a compliment to the existing model.

Finally, MRI [138, 162-163] and US [164] thermometry methods have been developed for monitoring local temperature changes during thermal therapies (e.g. radiofrequency or microwave ablation). These methods allow for the real-time, dynamic mapping of temperatures and estimation of thermal dose and can therefore assist in accurate therapeutic delivery. However, challenges currently exist to MR-compatibility of ablation hardware, MRI availability, and the considerable added cost [138]. Currently, work towards the clinical implementation of ultrasound thermometry for monitoring thermotherapies remains a proof of concept [164]. The predictive modeling methods presented within this work are intended to serve as an alternative to direct thermal monitoring. However, limited MR or US thermometry data could be incorporated within the ablation model in an inverse fashion to better predict volumetric outcome following therapy.

VII.2.5 Realization of the Predictive and Navigational Framework

The individual aims of this dissertation have laid the groundwork a biophysical model-based predictive and navigational framework for the delivery of hepatic microwave ablation. The previous subsections have highlighted additional contributions that can be made to each aim of this work. However, the ultimate goal is to deliver a fully developed planning and guidance framework for clinical use.

In this section I will outline the major components of this theoretical planning and guidance framework. The system will incorporate data from (1) multimodal medical imaging (e.g. MRI, CT, iUS), (2) guidance (e.g. optical or EM tracking), and (3) computational modeling of both the predicted ablation outcome and for intraoperative deformation correction. The ultimate goal of this system will be to utilize preoperative medical imaging to provide accurate predictive modeling of the ablation procedure which is then realized intraoperatively through advanced image-guidance techniques.

Looking forward, in a theoretical procedure, a patient would first be imaged with the current standard medical imaging protocol. An additional scan would then be gathered to quantify some physical state of organ disease (e.g. quantification of organ fat or water content, level of perfusion, or stage of cirrhosis). A 3D model of the patient's organ would then be generated from these medical images for preoperative use in procedural modeling and intraoperative use in deformation correction. Patient-specific material properties would then be estimated from the quantitative medical images. A predictive modeling framework would then be employed within an optimization scheme to define an optimal procedural scenario to ablate the targeted lesion while sparing healthy tissue and ensuring adequate margins. This predictive model would provide the ablation antenna tip and trajectory information that would then be used intraoperatively to achieve this optimal ablation

scenario. During treatment, organ surface data would be collected and used to achieve an image-to-physical registration (e.g. with the rigid registration and deformation correction methods outlined in this dissertation). Next, under image-guidance, the physician would deploy the ablation antenna(s) to the targeted location and trajectory to achieve the preoperatively defined ablation. The antenna location would then be confirmed with intraoperative ultrasound before delivering ablative therapy.

VII.3 Concluding Remarks

This dissertation has laid the groundwork for a model-based predictive and navigational therapeutic approach for image-guided hepatic microwave ablation. This work is the first to address (1) patient-specific tissue properties when modeling MWA in a predictive capacity and (2) to use a model-based correction approach to provide enhanced intraoperative image-guidance. Further advances to this work will ultimately lead to an improved procedural planning routine that can be deployed alongside advanced surgical navigation methods to improve the efficacy of hepatic microwave ablation procedures.

BIBLIOGRAPHY

[1] American Cancer Society. Cancer Facts and Figures 2017. Atlanta: American Cancer Society, 2017.

[2] K.R. Sheth and B.M. Clary, "Management of hepatic metastases from colorectal cancer," *Clin Colon Rectal Surg*, vol. 18, no. 3, pp. 215-223, 2005.

[3] S. Bengmark and L. Hafstrom, "The natural history of primary and secondary malignant tumors of the liver. I. The prognosis for patients with hepatic metastases from colonic and rectal carcinoma by laparotomy," *Cancer*, vol. 23, pp. 198-202, 1969.

[4] B. Cady, D.O. Monson, and N.W. Swinton, "Survival of patients after colonic resection for carcinoma with simultaneous liver metastases," *Surg Gynecol Obstet*, vol. 131, no. 4, pp. 697-700, 1970.

[5] C.R. Scoggins, I.M. Meszoely, C.D. Blanke, R.D. Beauchamp, and S.D. Leach, "Nonoperative management of primary colorectal cancer in patients with stage IV disease," *Ann Surg Oncol*, vol. 6, no. 7, pp. 651-657, 1999.

[6] B. Ohlsson, K.G. Tranberg, C. Lundstedt, H. Ekberg, and E. Hederstrom, "Detection of hepatic metastases in colorectal cancer: a prospective study of laboratory and imaging methods," *Eur J Surg*, vol. 159, no. 5, pp. 275-281, 1993.

[7] I.G. Finlay and C.S. McArdle, "Occult hepatic metastases in colorectal carcinoma," *Br J Surg*, vol. 73, no. 9, pp. 732-735, 1986.

[8] J. Ferlay, I. Soerjomataram, R. dikshit, S. Eser, C. Mathers, M. Rebelo, D.M. Parkin, D. Forman, and F. Bray, "Cancer incidence and mortality worldwide: sources, methods and major patterns in GLOBOCAN 2012," *Int J Cancer*, vol. 136, no. 5, pp. E359-E386, 2014.

[9] K. Ito, A. Govindarajan, H. Ito, and Y. Fong, "Surgical treatment of hepatic colorectal metastasis: evolving role in the setting of improving systematic therapies and ablative treatments in the 21st century," *Cancer J*, vol. 16, no. 2, pp. 103-110, 2010.

[10] E. Norero, N. Jarufe, J.M. Butte, B. Norero, I. Duarte, J. Torres, G. Pinedo, F. Lopez, J.F. Guerra, L. Ibanez, A. Zuniga, S. Guzman, and J. Martinez, "Outcome of surgical treatment of liver metastasis from colorectal cancer," *Rev Med Chile*, vol. 137, no. 4, pp. 487-496, 2009.

[11] R.P. DeMatteo, C. Palese, W.R. Jarnagin, R.L. Sim, L.H. Blumgart, and Y. Fong, "Anatomic segmental hepatic resection is superior to wedge resection as an oncologic operation for colorectal liver metastases," *J Gastrointest Surg*, vol. 4, no. 2, pp. 178-184, 2000.

[12] T. Mizuno, J.M. Cloyd, K. Omichi, Y.S. Chun, C. Conrad, C.W.D. Tzeng, S.H. Wei, T.A. Aloia, and J.N. Vauthey, "Two-stage hepatectomy vs one-stage major hepatectomy with contralateral resection or ablation for advanced bilobar colorectal liver metastases," *J Am Coll Surgeons*, vol. 226, no. 5, pp. 825-834, 2018.

[13] F. Alemi, E. Kwon, J. Chiu, H. Aoki, L. Stewart, and C.U. Corvera, "Laparoscopic treatment of liver tumours using a two-needle probe bipolar radiofrequency ablation device," *HPB Oxford*, vol. 13, no. 9, pp. 656-664, 2011.

[14] I. Reccia, J. Kumar, T. Kusano, A. Zanellato, A. Draz, D. Spalding, N. Habib, and M. Pai, "A systematic review on radiofrequency assisted laparoscopic liver resection: challenges and window to excel," *Surg Onc*, vol. 26, no. 3, pp. 296-304, 2017.

[15] M. Nikfarjam, S. Shereef, E.T. Kimchi, N.J. Gusani, Y. Jiang, D.M. Avella, R.P. Mahraj, and K.F. Staveley-O'Carroll, "Survival outcomes of patients with colorectal liver metastases following hepatic resection or ablation in the era of effective chemotherapy," *Ann Surg Onc*, vol. 16, no. 7, pp. 1860-1867, 2009.

[16] F. Manizate, S.P. Hiotis, D. Labow, S. Roayaie, and M. Schwartz, "Liver functional reserve estimation: state of the art and relevance to local treatments," *Onc*, vol. 78, no. 1, pp. 131-134, 2010.

[17] E.K. Abdalla, R. Adam, A.J. Bilchik, D. Jaeck, J.N. Vauthey, and D. Mahvi, "Improving resectability of hepatic colorectal metastases: expert consensus statement," *Ann Surg Onc*, vol. 13, no. 10, pp. 1271-1280, 2006.

[18] U. Leung, D. Kuk, M.I. D'Angelica, T.P. Kingham, P.J. Allen, R.P. DeMatteo, W.R. Jarnagin, and Y. Fong, "Long-term outcomes following microwave ablation for liver malignancies," *Br J Surg*, vol. 102, pp. 85-91, 2015.

[19] E.S. Alexander, F.J. Wolf, J.T. Machan, K.P. Charpentier, M.D. Beland, J.D. Iannuccilli, R.H. Haas, and D.E. Dupuy, "Microwave ablation of focal hepatic malignancies regardless of size: A 9-year retrospective study of 64 patients," *Eur J Radiol*, vol. 84, no. 6, pp. 1083-1090, 2015.

[20] R.C.G. Martin, C.R. Scoggins, and K.M. McMasters, "Safety and efficacy of microwave ablation of hepatic tumors: a prospective review of a 5-year experience," *Ann Surg Oncol*, vol. 17, pp. 171-178, 2010.

[21] C. Correa-Gallego, Y. Fong, M. Gonen, M.I. D'Angelica, P.J. Allen, R.P. DeMatteo, W.R. Jarnagin, and T.P. Kingham, "A retrospective comparison of microwave ablation vs radiofrequency ablation for colorectal cancer hepatic metastases," *Ann Surg Oncol*, vol. 21, no. 13, pp. 4278-4283, 2014.

[22] T.A. Potretzke, T.J. Ziemlewicz, J.L. Hinshaw, M.G. Lubner, S.A. Wells, C.L.

Brace, P. Agarwal, and F.T. Lee, “Microwave versus radiofrequency ablation treatment for hepatocellular carcinoma: A comparison of efficacy at a single center,” *J Vasc Int Radiol*, vol. 27, no. 5, pp. 631-638, 2016.

[23] L. Solbiati, T. Livraghi, S.N. Goldberg, T. Ierace, F. Meloni, M. Dellanoce, L. Cova, E.F. Halpern, and G.S. Gazelle, “Percutaneous radio-frequency ablation of hepatic metastases from colorectal cancer: Long-term results in 117 patients,” *Radiology*, vol. 221, no. 1, pp. 159-166, 2001.

[24] N.V. Violi, R. Duran, B. Guiu, J.P. Cercueil, C. Aube, A. Digklia, I. Pache, P. Deltenre, J.F. Knebel, and A. Denys, “Efficacy of microwave ablation versus radiofrequency ablation for the treatment of hepatocellular carcinoma in patients with chronic liver disease: a randomized controlled phase 2 trial,” *Lancet Gastroenterol Hepatol*, vol. 3, no. 5, pp. 317-325, 2018.

[25] P. Liang, B. Dong, X. Yu, Y. Yang, D. Yu, L. Su, Q. Xiao, and L. Sheng, “Prognostic factors for percutaneous microwave coagulation therapy of hepatic metastases,” *Am J Roentg*, vol. 181, no. 5, pp. 1319-1325, 2003.

[26] H. Shen, S. Zhou, Y. Lou, Y. Gao, S. Cao, D. Wu, and G. Li, “Microwave-assisted ablation improved prognosis of patients with hepatocellular carcinoma undergoing liver resection,” *Technol Cancer Res T*, vol. 17, 2018.

[27] C.C.N. Chong, K.F. Lee, C.M. Chu, A.W.H. Chan, J. Wong, S.L. Chan, H.T. Lok, A.K.Y. Fung, A.K.W. Fong, Y.S. Cheung, S.C.H. Yu, P. Johnson, and P.B.S. Lai, “Microwave ablation provides better survival than liver resection for hepatocellular carcinoma in patients with borderline liver function: application of ALBI score to patient selection,” *HPB*, vol. 20, no. 6, pp. 546-554, 2018.

[28] A.R. Kolarich, R. Cabrera, S.J. Hughes, T.J. George, B.S. Geller, J.R. Grajo, “Thermal ablation versus wedge or segmental resection in patients with early stage hepatocellular carcinoma: a population survival analysis,” *HPB*, 2018.

[29] I.R. Andersen, F.V. Mortensen, J. Kirkegaard, F. Rasmussen, D.T. Nielsen, and D.W. Kjaer, “Long-term survival following ablation of colorectal liver metastases,” *J Surgery*, vol. 6, pp. 13-18, 2018.

[30] H. Takahashi, B. Kahramangil, and E. Berber, “Local recurrence after microwave thermosphere ablation of malignant liver tumors: results of a surgical series,” *Surgery*, vol. 163, no. 4, pp. 709-713, 2018.

[31] C. Simon, D.E. Dupuy, and W.W. Mayo-Smith, “Microwave ablation: principles and applications,” *Radiographics*, vol. 25, pp. S69-S83, 2005.

[32] T. Ikemoto, M. Shimada, and S. Yamada, “Pathophysiology of recurrent hepatocellular carcinoma after radiofrequency ablation,” *Hepatol Res*, vol. 47,

2016.

[33] S.N. Goldberg, J.W. Charboneau, G.D. Dodd, et al., “Image-guided tumor ablation: proposal for standardization of terms and reporting criteria,” *Radiology*, vol. 228, pp. 335-345, 2003.

[34] S.G. Silverman, B.D. Collick. M.R. Figueira, et al., “Interactive MR-guided biopsy in an open-configuration MR imaging system,” *Radiology*, vol. 197, no. 1, 1995.

[35] K.M. Pondman, J.J. Futterer, B.T Haken, et al., “MR-guided biopsy of the prostate: an overview of techniques and a systematic review,” *Euro Urology*, vol. 54, no.3, pp. 517-527, 2008.

[36] G.S. Gazelle and J.R. Haaga, “Guided percutaneous biopsy of intraabdominal lesions,” *Am J Roentgenol*, vol. 153, no. 1, pp. 929-935, 1989.

[37] H. Hirschberg, E. Samset, P.K. Hol, T. Tillung, and K. Lote, “Impact of intraoperative MRI on the surgical results for high-grade gliomas,” *Min Inv Neurosurg*, vol. 48, no. 2, pp. 77-84, 2005.

[38] M.A. Lewis, R.M. Staruch, and R. Chopra, “Thermometry and ablation monitoring with ultrasound,” *Int J Hyperthermia*, vol. 31, no. 2, pp. 163-181, 2015.

[39] P.J. Besl and N.D. McKay, “Method for registration of 3-d shapes,” *IEEE T Pattern Anal*, vol. 14, pp. 239-256, 1992.

[40] D.M. Cash, T.K. Sinha, W.C. Chapman, et al., “Incorporation of a laser range scanner into image-guided liver surgery: surface acquisition, registration, and tracking,” *Med Phys*, vol. 30, no. 1671, 2003.

[41] D.M. Cash, M.I. Miga, S.C. Glasgow, et al., “Concepts and preliminary data toward the realization of image-guided liver surgery,” *J Gastrointest Surg*, vol. 11, no. 7, pp. 844-859, 2007.

[42] L.W. Clements, W.C. Chapman, B.M. Dawant, et al., “Robust surface registration using salient anatomical features for image-guided liver surgery: algorithm and validation,” *Med Phys*, vol. 35, no. 6, pp. 2528-2540, 2008.

[43] T.P. Kingham, M.A. Scherer, B.W. Neese, L.W. Clements, J.D. Stefansic, and W.R. Jarnagin, “Image-guided liver surgery, intraoperative projection of computed tomography images utilizing tracked ultrasound,” *HPB*, vol. 14, no. 9, pp. 594-603, 2012.

[44] R.C.G. Martin and D.A. North, “Enhanced ultrasound with navigation leads to improved liver lesion identification and needle placement,” *J Surg Res*, vol. 200, no. 2, pp. 420-426, 2016.

[45] D. Sindram, R.Z. Swan, K.N. Lau, I.H. McKillop, D.A. Iannitti, and J.B. Martinie, "Real-time three-dimensional guided ultrasound targeting system for microwave ablation of liver tumours: a human pilot study," *HPB*, vol. 13, no. 3, pp. 185-191, 2011.

[46] C.W. Hammill, L.W. Clements, J.D. Stefansic, R.F. Wolf, P.D. Hansen, and D.A. Gerber, "Evaluation of a minimally invasive image-guided surgery system for hepatic ablation procedures," *Surg Innov*, vol. 21, no. 4, pp. 419-426, 2014

[47] V.M. Banz, P.C. Muller, P. Tinguely, D. Inderbitzin, D. Ribes, M. Peterhans, D. Candinas, and S. Weber, "Intraoperative image-guided navigation system: development and applicability in 65 patients undergoing liver surgery," *Langenbeck Arch Surg*, vol. 401, pp. 495-502, 2016.

[48] D. Sindram, K.A. Simo, R.Z. Swan, S. Razzaque, D.J. Niemeyer, R.M. Seshadri, E. Hanna, I.H. McKillop, D.A. Iannitti, and J.B. Martinie, "Laparoscopic microwave ablation of human liver tumours using a novel three-dimensional magnetic guidance system," *HPB*, vol. 17, pp. 87-93, 2015.

[49] I. Paoluucci, M. Schwalbe, G.A. Prevost, A. Lachenmayer, D. Candinas, S. Weber, and P. Tinguely, "Design and implementation of an electromagnetic ultrasound-based navigation technique for laparoscopic ablation of liver tumors," *Surg Endosc*, vol. 32, pp. 3410-3419, 2018.

[50] P. Tinguely, M. Fusaglia, J. Freedman, V. Banz, S. Weber, D. Candinas, and H. Nilsson, "Laparoscopic image-based navigation for microwave ablation of liver tumors – a multi-center study," *Surg Endosc*, vol. 31, pp. 4315-4324, 2017.

[51] D.J. Hawkes, D. Barratt, J.M. Blackall, C. Chan, P.J. Edwards, K. Rhode, G.P. Penney, J. McClelland, and D.L.G. Hill, "Tissue deformation and shape models in image-guided interventions: a discussion paper," *Med Image Anal*, vol. 9, no. 2, pp. 163-175, 2005.

[52] A. Irshad, M. Anis, and S.J. Ackerman, "Current role of ultrasound in chronic liver disease: surveillance, diagnosis and management of hepatic neoplasms," *Curr Probl Diagn Radiol*, vol. 41, pp. 43-51, 2012.

[53] T.P. Kingham, L.M. Pak, A.L. Simpson, U. Leung, A. Doussot, M.I. D'Angelica, R.P. DeMatteo, P.J. Allen, W.R. Jarnagin, "3D image guidance assisted identification of colorectal cancer liver metastases not seen on intraoperative ultrasound: results from a prospective trial," *HPB*, vol. 20, no. 3, pp. 260-267, 2018.

[54] V.M. Banz, M. Baechtold, S. Weber, M. Peterhans, D. Inderbitzin, and D. Candinas, "Computer planned, image-guided combined resection and ablation for bilobar colorectal liver metastases," *World J Gastroenterol*, vol. 20, pp. 14992-

14996, 2014.

[55] T. Lange, S. Eulenstein, M. Hunerbein, and P.M. Schlag, "Vessel-based non-rigid registration of MR/CT and 3D ultrasound for navigation in liver surgery," *Comput Aided Surg*, vol. 8, no. 5, pp. 228-240, 2003.

[56] Y. Hu, E.J. Rijkhorst, R. Manber, D. Hawkes, and D. Barratt, "Deformable vessel-based registration using landmark-guided coherent point drift," Medical Imaging and Augmented Reality 2010. Lect Notes Comput Sc, vol. 6326, pp. 60-69, 2010.

[57] M.I. Miga, T.K. Sinha, D.M. Cash, R.L. Galloway, and R.J. Weil, "Cortical surface registration for image-guided neurosurgery using laser range scanning," *IEEE T Med Imaging*, vol. 22, pp. 973-985, 2003.

[58] D.M. Cash, M.I. Miga, T.K. Sinha, R.L. Galloway, and W.C. Chapman, "Compensating for intraoperative soft-tissue deformations using incomplete surface data and finite elements," *IEEE T Med Imaging*, vol. 24, no. 11, pp. 1479-1491, 2005.

[59] P. Dumpuri, L.W. Clements, B.M. Dawant, and M.I. Miga, "Model-updated image-guided liver surgery: preliminary results using surface characterization," *Prog Biophys Mol Bio*, vol. 103, no. 2-3, pp. 197-207, 2010.

[60] D.C. Rucker, Y. Wu, L.W. Clements, J.E. Ondrake, T.S. Pheiffer, A.L. Simpson, W.R. Jarnagin, and M.I. Miga, "A mechanics-based nonrigid registration method for liver surgery using sparse intraoperative data," *IEEE T Med Imaging*, vol. 33, pp. 147-158, 2014.

[61] J.S. Heiselman, L.W. Clements, J.A. Collins, J.A. Weis, A.L. Simpson, S.K. Geevarghese, T.P. Kingham, W.R. Jarnagin, and M.I. Miga, "Characterization and correction of intraoperative soft tissue deformation in image-guided laparoscopic liver surgery," *J Med Imag*, vol. 5, no. 2, 2017.

[62] L.W. Clements, J.A. Collins, J.A. Weis, A.L. Simpson, L.B. Adams, W.R. Jarnagin, and M.I. Miga, "Evaluation of model-based deformation correction in image-guided liver surgery via tracked intraoperative ultrasound," *J Med Imag*, vol. 3, 2016.

[63] J.A. Collins, J.A. Weis, J.S. Heiselman, L.W. Clements, A.L. Simpson, W.R. Jarnagin, and M.I. Miga, "Improving registration robustness for image-guided liver surgery in a novel human-to-phantom data framework," *IEEE T Med Imaging*, vol. 36, no. 7, pp. 1502-1510, 2017.

[64] L.W. Clements, J.A. Collins, J.A. Weis, A.L. Simpson, T.P. Kingham, W.R. Jarnagin, and M.I. Miga, "Deformation correction of image guided liver surgery: an intraoperative fidelity assessment," *Surgery*, vol. 162, no. 3, pp. 537-547, 2017.

[65] R.S. Winokur, J.Y. Du, B.B. Pua, A.D. Talenfeld, A.K. Sista, M.A. Schiffman, D.W. Trost, and D.C. Madoff, "Characterization of *in vivo* ablation zones following percutaneous microwave ablation of the liver with two commercially available devices: Are manufacturer published reference values useful?" *J Vasc Interv Radiol,* vol. 25, no. 12, pp. 1939-1946, 2014.

[66] D.T. Glidden, M. Cook, S. Collins, G. Deshazer, K. Nand, G.L. Baird, B. Kimia, D. Merck, and D.E. Dupuy, "Clinically observed ablation volumes as compared to vendor specified volumes: the emperor's new clothes," *J Vasc Interv Radiol,* vol. 25, no. 3, pp. S76, 2014.

[67] C.L. Brace, "Dual-slot antennas for microwave tissue heating: parametric design analysis and experimental validation," *Med Phys,* vol. 38, pp. 4232-4240, 2011.

[68] C.L. Brace, P.F. Laeseke, D.W. van der Weide, and F.T. Lee, "Microwave ablation with a triaxial antenna: results in *ex vivo* bovine liver," *IEEE Trans Microwave Theory and Techniques,* vol. 53, pp. 215-220, 2005.

[69] Y. Liu, X. Yang, Q. Nan, J. Xiao, and L. Li, "Phantom experimental study on microwave ablation with a water-cooled antenna," *Int J Hyperthermia,* vol. 23, no. 4, pp. 381-386, 2007.

[70] P. Prakash, G. Deng, M.C. Converse, J.G. Webster, D.M. Mahvi, and M.C. Ferris, "Design optimization of a robust sleeve antenna for hepatic microwave ablation," *Phys Med Biol,* vol. 53, no. 4, pp. 1057-1069, 2008.

[71] S. Etoz and C.L. Brace, "Analysis of microwave ablation antenna optimization techniques," *Int J RF Microw C E,* 2017.

[72] W. Zhai, J. Xu, Y. Zhao, Y. Song, L. Sheng, and P. Jia, "Preoperative surgery planning for percutaneous hepatic microwave ablation," MICCAI, New York, NY, 2008, pp. 569-577.

[73] J.A. Collins, D.B. Brown, T.P. Kingham, W.R. Jarnagin, M.I. Miga, and L.W. Clements, "Method for evaluation of predictive models of microwave ablation via post-procedural clinical imaging," SPIE Medical Imaging, Orlando, FL, 2015.

[74] G. Deshazer, M. Hagmann, D. Merck, J. Sebek, K.B. Moore, and P. Prakash, "Computational modelling of 915 MHz microwave ablation: comparative assessment of temperature-dependent tissue dielectric models," *Med Phys,* vol. 44, no. 9, pp. 4859-4868, 2017.

[75] Z. Ji and C.L. Brace, "Expanded modelling of temperature-dependent dielectric properties for microwave thermal ablation," *Phys Med Biol,* vol. 56, no. 16, pp. 5249-5264, 2011.

[76] D. Liu and C.L. Brace, "Numerical simulation of microwave ablation incorporating tissue contraction based on thermal dose," *Phys Med Biol*, vol. 62, no. 6, pp. 2070-2086, 2017.

[77] V. Lopresto, R. Pinto, L. Farina, and M. Cavagnaro, "Microwave thermal ablation: effects of tissue properties variations on predictive models for treatment planning," *Med Eng Phys*, vol. 46, pp. 63-70, 2017.

[78] J. Sebek, N. Albin, R. Bortel, B. Natarajan, and P. Prakash, "Sensitivity of microwave ablation models to tissue biophysical properties: A first step toward probabilistic modelling and treatment planning," *Med Phys*, vol. 43, no. 5, pp. 2649-2661, 2016.

[79] C. Rossmann and D. Haemmerich, "Review of temperature dependence of thermal properties, dielectric properties, and perfusion of biological tissues at hyperthermic and ablation temperatures," *Crit Rev Biomed Eng*, vol. 42, no. 6, pp. 467-492, 2014.

[80] D. Yang, M.C. Converse, D.M. Mahvi, and J.G. Webster, "Measurement and analysis of tissue temperature during microwave liver ablation," *IEEE Trans Biomed Eng*, vol. 54, pp. 150-155, 2006.

[81] D. Haemmerich, A.W. Wright, D.M. Mahvi, F.T. Lee, and J.G. Webster, "Hepatic bipolar radiofrequency ablation creates coagulation zones close to blood vessels: A finite element study," *Med Biol Eng Comput*, vol. 41, no. 3, pp. 317-323, 2003.

[82] W. Schramm, D. Yang, and D. Haemmerich, "Contribution of direct heating, thermal conduction and perfusion during radiofrequency and microwave ablation," IEEE EMBS, New York, NY, 2006.

[83] N.C. Yu, S.S. Raman, Y.J. Kim, C. Lassman, X. Chang, and D.S.K. Lu, "Microwave liver ablation: influence of hepatic vein size on heat-sink effect in a porcine model," *J Vasc Interv Radiol*, vol. 19, no. 7, pp. 1087-1092, 2008.

[84] A. Marengo, C. Rosso, and E. Bugianesi, "Liver cancer: connections with obesity, fatty liver, and cirrhosis," *Annu Rev Med*, vol. 67, pp. 103-117, 2016.

[85] A.P. O'Rourke, M. Lazebnik, J.M. Bertram, M.C. Converse, S.C. Hagness, J.G. Webster, and D.M. Mahvi, "Dielectric properties of human normal, malignant and cirrhotic liver tissue: *in vivo* and *ex vivo* measurements from 0.5 to 20 GHz using a precision open-ended coaxial probe," *Phys Med Biol*, vol. 52, no. 15, pp. 4707-4719, 2007.

[86] V. Bhat, S. Velandai, V. Belliappa, J. Illayraja, K.G. Halli, and G. Gopalakrishnan, "Quantification of liver fat with mDIXON magnetic resonance imaging, comparison with the computed tomography and the biopsy," *J Clin Diagn Res*, vol. 11, no. 7, pp. 6-10, 2017.

[87] Y. Fujiwara, H. Kuroda, T. Abe, K. Ishida, T. Oguri, S. Noguchi, T. Sugai, N. Kamiyama, and Y. Takikawa, “The b-mode image-guided ultrasound attenuation parameter accurately detects hepative steatosis in chronic liver disease,” *Ultrasound Med Biol*, [in press], 2018.

[88] S. Gabriel, R.W. Lau, and C. Gabriel, “The dielectric properties of biological tissues: II. Measurements in the frequency range 10 Hz to 20 GHz,” *Phys Med Bio*, vol. 41, no. 11, pp. 2251-2269, 1996.

[89] W.C. Dewey and C.J. Diederich, “Hyperthermia classic commentary: ‘Arrhenius relationships from the molecule and cell to the clinic’ by William Dewey,” *Int J Hyperthermia*, vol. 25, pp. 21-24, 2009.

[90] F. Henriques, “Studies of thermal injury. V. The predictability and the significance of thermally induced rate processes leading to irreversible epidermal injury,” *Arch Patho*, vol. 23, pp. 695, 1947.

[91] S. Pisa, M. Cavagnaro, P. Bernardi, and J.C. Lin, “A 915-MHz antenna for microwave thermal ablation treatment: physical design, computer modeling and experimental measurement,” *IEEE Trans Biomed Eng*, vol. 48, pp. 599-601, 2001.

[92] D. Yang, “Measurements, antenna design and advanced computer modeling for microwave tissue ablation,” in Biomedical Engineering. Madison, WI: University of Wisconsin, 2006.

[93] F. Gao, G.B. Wang, Z.W. Xiang, B. Yang, J.B. Xue, Z.Q. Mo, Z.H. Zhong, T. Zhang, F.J. Zhang, and W.J. Fan, “A preoperative mathematic model for computed tomographic guided microwave ablation treatment of hepatic dome tumors,” *Oncotarget*, vol. 7, no. 18, pp. 25949-25959.

[94] J.M. Bertram, D. Yang, M.C. Converse, J.G. Webster, and D.M. Mahvi, “Antenna design for microwave hepatic ablation using an axisymmetric electromagnetic model,” *Biomed Eng Online*, pp. 5-15, 2006.

[95] P. Phasukkit, S. Tungjitkusolmun, and M. Sangworasil, “Finite-element analysis and in vitro experiments of placement configurations using triple antennas in microwave hepatic ablation,” *IEEE Trans Biomed Eng*, vol. 56, no. 11, pp. 2564-2572, 2009.

[96] M. Cavagnaro, R. Pinto, and V. Lopresto, “Numerical models to evaluate the temperature increase induced by *ex vivo* microwave thermal ablation,” *Phys Med Biol*, vol. 60, pp. 3287-3311, 2015.

[97] V. Lopresto, R. Pinto, and M. Cavagnaro, "Experimental characterisation of the thermal lesion induced by microwave ablation," *Int J Hyperthermia*, vol. 30, no. 2, pp. 110-118, 2014.

[98] M. Lazebnik, M.C. Converse, J.H. Booske, and S.C. Hagness, "Ultrawideband temperature-dependent dielectric properties of animal liver tissue in the microwave frequency range," *Phys Med Biol*, vol. 51, pp. 1941-1955, 2006.

[99] P.R. Stauffer, F. Rossetto, M. Prakash, D.G. Neuman, and T. Lee, "Phantom and animal tissues for modelling the electrical properties of human liver," *Int J Hyperthermia*, vol. 19, pp. 89-101, 2003.

[100] C.L. Brace, "Temperature-dependent dielectric properties of liver tissue measured during thermal ablation: toward an improved numerical model," Conf. Proc. IEEE Eng Med Biol Soc, pp. 230-233, 2008.

[101] H.H. Pennes, "Analysis of tissue and arterial blood temperatures in the resting human forearm," *J Appl Physiol*, vol. 85, pp. 5-34, 1978.

[102] D. Haemmerich, D.J. Schutt, I. dos Santos, eJ.G. Webster, and D.M. Mahvi, "Measurement of temperature-dependent specific heat of biological tissues," *Physiol Meas*, vol. 26, pp. 59-67, 2005.

[103] G. Shafirstein, W. Baumler, M. Lapidoth, S. Ferguson, P.E. North, and M. Waner, "A new mathematical approach to the diffusion approximation theory for selective photothermolysis modeling and its implication in laser treatment of port-wine stains," *Lasers Surg Med*, vol. 34, pp. 335-347, 2004.

[104] J.W. Valvano, J.R. Cochran, and K.R. Diller, "Thermal-conductivity and diffusivity of biomaterials measured with self-heated thermistors," *Int J Thermophys*, vol. 6, pp. 301-311, 1985.

[105] L. Zhu, L.X. Xu, and N. Chencinski, "Quantification of the 3-D electromagnetic power absorption rate in tissue during transurethral prostatic microwave thermotherapy using heat transfer model," *IEEE T Biomed Eng*, vol. 45, pp. 1163-1172, 1998.

[106] F. Liu, P. Liang, X. Yu, T. Lu, Z. Cheng, C. Lei and Z. Han., "A three-dimensional visualization preoperative treatment planning system in microwave ablation for liver cancer: A preliminary clinical application," *Int J Hyperthermia*, vol. 29, no. 7, pp. 671-677, 2013.

[107] P. Liang and Y. Wang, "Microwave ablation of hepatocellular carcinoma," *Oncology*, vol. 72, pp. S124-S131, 2007.

[108] P. Zhou, P. Liang, X. Yu, Y. Wang, and B. Dong, "Percutaneous microwave ablation of liver cancer adjacent to the gastrointestinal tract," *J Gastrointest Surg*, vol. 13, pp. 318-324, 2009.

[109] E. Berber, "The first clinical application of planning software for laparoscopic

microwave thermosphere ablation of malignant liver tumours," *HPB*, vol. 17, pp. 632-636, 2015.

[110] P.A. Yushkevich, J. Piven, H.C. Hazlett, R.G. Smith, S. Ho, J.C. Gee, and G. Gerig, "User-guided 3d active contour segmentation of anatomical structures: significantly improved efficiency and reliability," *Neuroimage*, vol. 31, no. 3, pp. 1116-1128, 2006.

[111] W.E. Lorensen and H.E. Cline, "Marching cubes: a high resolution 3d surface construction algorithm," *ACM SIGGRAPH Comput Graph*, vol. 21, no. 4, pp. 163-169, 1987.

[112] W.J. Scheroeder and W.A. Hoffman, "The visualization toolkit user's guide," 2006.

[113] J.M. Sullivan, G. Charron, and K.D. Paulsen, "A three-dimensional mesh generator for arbitrary multiple material domains," *Finite Elements in Analysis and Design*, vol. 25, no. 3, pp. 219-241, 1997.

[114] N.D. Glossop, "Advantages of optical compared with electromagnetic tracking," *J Bone Joint Surg Am*, vol. 91, pp. 23-28, 2009.

[115] T. Pheiffer, "Surgical navigation using tracked ultrasound," in Biomedical Engineering. Nashville, TN: Vanderbilt University, 2014.

[116] J. D'Errico. (2005). Surface fitting using gridfit. [Online]. Matlab Central File Exchange.

[117] T.P. Kingham, S. Jayaraman, L.W. Clements, M.A. Scherer, J.D. Stefansic, and W.R. Jarnagin, "Evolution of image-guided liver surgery: transition from open to laparoscopic procedures," *J Gastro Surg*, vol. 17, no. 7, pp. 1274-1282, 2013.

[118] L. Maier-Hein, P. Mountney, A. Bartoli, H. Elhawary, D. Elson, A. Groch, A. Kolb, M. Rodrigues, J. Sorger, S. Speidel, and D. Stoyanov, "Optical techniques for 3D surface reconstruction in computer-assisted laparoscopic surgery," *Med Imag An*, vol. 17, pp. 974-996, 2013.

[119] Y. Song, J. Totz, S. Thompson, S. Johnsen, D. Barratt, C. Schneider, K. Gurusamy, B. Davidson, S. Ourselin, D. Hawkes, and M.J. Clarkson, "Locally rigid, vessel-based registration for laparoscopic liver surgery," *Int J Comput Ass Rad*, vol. 10, pp. 1951-1961, 2015.

[120] M.A. Clifford, F. Banovac, E. Levy, and K. Cleary, "Assessment of hepatic motion secondary to respiration for computer assisted interventions," *Comput Aided Surg*, vol. 7, no. 5, pp. 291-299, 2002.

[121] O. Heizmann, S. Zidowitz, H. Bourquain, S. Potthast, H.O. Peitgen, D. Oertli, and

C. Kettelhack, “Assessment of intraoperative liver deformation during hepatic resection: Prospective clinical study,” *World J Surg*, vol. 34, pp. 1887-1893, 2010.

[122] L.W. Clements, P. Dumpuri, W.C. Chapman, B.M. Dawant, R.L. Galloway, and M.I. Miga, “Organ surface deformation measurement and analysis in open hepatic surgery: Method and preliminary results from 12 clinical cases,” *IEEE T Biomed Eng*, vol. 58, no. 8, pp. 2280-2289, 2011.

[123] S. Khallagi, C.G.M. Leung, K. Hastrudi-Zaad, P. Foroughi, C. Nguan, and P. Abolmaesumi, “Experimental validation of an intrasubject eleastic registration algorithm for dynamic-3D ultrasound images,” *Med Phys*, vol. 39, pp. 5488-5497, 2012.

[124] A. D. Wiles, D. G. Thompson, and D. D. Frantz. (2004, May). Accuracy assessment and interpretation for optical tracking systems. Presented at SPIE Medical Imaging. [Online]. SPIE Digital Library.

[125] T. Lange, M. Hunerbein, S. Eulenstein, S. Beller, P. M. Schlag, “Development of navigation systems for image-guided laparoscopic tumor resections in liver surgery,” in Minimally Invasive Tumor Therapies, Berlin, Germany: Springer, 2006, ch. 1, pp. 13-36.

[126] M. Peterhans, A. vom Berg, B. Dagon, D. Inderbitzin, C. Baur, D. Candinas, and S. Weber, “A navigation system for open liver surgery: design, workflow and first clinical applications,” *Int J Med Robot Comp*, vol. 7, no. 1, pp. 7-16, 2011.

[127] S. Placht, J. Stancanello, C. Schaller, M. Balda, and E. Angelopoulou, “Fast time-of-flight camera based surface registration for radiotherapy patient positioning,” *Med Phys*, vol. 39, no. 1, pp. 4-17, 2012.

[128] P. Paul, X. Morandi, and P. Jannin, “A surface registration method for quantification of intraoperative brain deformations in image-guided neurosurgery,” *IEEE T Inf Technol B*, vol. 13, no. 6, pp. 976-983, 2009.

[129] L.M. Su, B.P. Vagvolgyi, R. Agarwal, C.E. Reiley, R.H. Taylor, and G.D. Hager, “Augmented reality during robot-assisted laparoscopic partial nephrectomy: toward real-time 3D-CT to stereoscopic video registration,” *Urololgy*, vol. 73, no. 4, pp. 896-900, 2009.

[130] R. A. Lathrop, D. M. Hackworth, and R. J. Webster, “Minimally invasive holographic surface scanning for soft-tissue image registration,” *IEEE T Biomed Eng*, vol. 57, no. 6, pp. 1497-1506, 2010.

[131] A.L. Simpson, J. Burgner, C.L. Glisson, S.D. Herrell, T.S. Pheiffer, R.J. Webster, M.I. Miga, “Comparison study of intraoperative surface acquisition methods for surgical navigation,” *IEEE T Biomed Eng*, vol. 60, no. 4, pp. 1090-1099, 2013.

[132] K. J. M. Surry, H. J. B. Austin, A Fenster, and T. M. Peters, "Poly(vinyl alcohol) cryogel phantoms for use in ultrasound and MR imaging," *Phys Med Bio*, vol. 49, no. 24, pp. 5529-5546.

[133] R. Plantefeve, I. Peterlik, N. Haouchine, and S. Cotin, "Patient-specific biomechanical modeling for guidance during minimally-invasive hepatic surgery," *Ann Biomed Eng*, vol. 44, no. 1, pp. 139-153.

[134] D. J. Kroon. (2009). Finite iterative closest point. [Online]. Available: Matlab Central File Exchange.

[135] Y. Wu, D. C. Rucker, R. H. Conley, T. S. Pheiffer, A. L. Simpson, S. K. Geevarghese, and M. I. Miga, "Registration of liver iamges to minimally invasive intraoperative surface and subsurface data," Proc. SPIE 9036, Medical Imaging 2014: Image-Guided Procedures, Robotic Interventions, and Modeling, 2014.

[136] P.A. Yushkevich, J. Piven, H.C. Hazlett, R.G. Smith, S. Ho, J.C. Gee, and G. Geric, "User-guided 2D active contour segmentation of anatomical structures: significantly improved efficiency and reliability," *Neuroimage*, vol. 31, no. 3, pp. 1116-1128, 2006.

[137] S. Pathak, R. Jones, J.M.F. Tang, C. Parmar, S. Fenwick, H. Malik, and G. Poston, "Ablative therapies for colorectal liver metastases: a systematic review," *Colorectal Disease*, vol. 13, no. 9, pp. e252-e265, 2011.

[138] B.D. de Senneville, C. Mougenot, B. Quesson, I. Dragonu, N. Grenier, and C.T.W. Moonen, "MR thermometry for monitoring tumor ablation," *Eur Radiol*, vol. 17, no. 9, pp. 2401-2410, 2007.

[139] P. Prakash, "Theoretical modelling for hepatic microwave ablation," *Open Biomed Eng J*, vol. 4, pp. 27-38, 2010.

[140] O.F. Oran and Y.Z. Ider, "Feasibility of conductivity imaging using subject eddy currents induced by switching of MRI gradients," *Magn Reson Med*, vol. 77, no. 5, pp. 1926-1937, 2017.

[141] M.A. Kandadai, J.L. Raymond, and G.J. Shaw, "Comparison of electrical conductivities of various brain phantom gels: developing a brain gel model," *Mat Sci Eng C*, vol. 32, no. 8, pp. 2664-2667, 2012.

[142] B.D. Roebuck and S.A. Goldblith, "Dielectric properties at microwave frequencies of agar gels," *J Food Sci*, vol. 40, no. 5, pp. 899-902, 1975.

[143] O.K. Bates, "Thermal conductivity of liquid silicones," *Ind Eng Chem*, vol. 41, no. 9, pp. 1966-1968, 1949.

[144] M. Zhang, Z. Che, J. Chen, H. Zhao, L. Yang, Z. Zhong, and J. Lu, “Experimental determination of thermal conductivity of water-agar gel at different concentrations and temperatures,” *J Chem Eng Data*, vol. 56, no. 4, pp. 859-864, 2011.

[145] J. Corach, P.A. Sorichetti, and S.D. Romano, “Electrical properties of vegetable oils between 20 Hz and 2 MHz,” *Int J Hydrogen Energ*, vol. 39, no. 16, pp. 8754-8758, 2014.

[146] W.E. Pace, W.B. Westphal, and S.A. Goldblith, “Dielectric properties of commercial cooking oils,” *J Food Sci*, vol. 33, pp. 30-36, 1968.

[147] Engineering ToolBox (2003). Specific heat of liquids and fluids. [Online]. Available: https://engineeringtoolbox.com/specific-heat-fluids-d_151.html

[148] A. Turgut, I. Tavman, and S. Tavman, “Measurement of thermal conductivity of edible oils using transient hot wire method,” *Int J Food Prop*, vol. 12, no. 4, pp. 741-747, 2009.

[149] J. Wang, J. Tang, Y. Wang, and B. Swanson, “Dielectric properties of egg whites and whole eggs as influenced by thermal treatments,” *LWT-Food Sci Technol*, vol. 42, no. 7, pp. 1204-1212, 2009.

[150] J.S.R. Coimbra, A.L. Gabas, L.A. Minim, E.E.G Rojas, V.R.N. Telis, and J. Telis-Romero, “Density, heat capacity and thermal conductivity of liquid egg products,” *J Food Eng*, vol. 74, no. 2, pp. 186-190, 2006.

[151] (2015, November). Product brochure Philips mDIXON Quant MR clinical application. Philips. Amsterdam, Netherlands. [Online]. Available: https://www.usa.philips.com/healthcare/product/HCNMRB462/

[152] I.A. Chang and U.D. Nguyen, “Thermal modeling of lesion growth with radiofrequency ablation devices,” *Biomed Eng Online*, vol. 3, 2004.

[153] P.R. Amestoy, I.S. Duff, J.Y. L’Excellent, and J. Koster, “A fully asynchronous multifrontal solver using distributed dynamic scheduling,” *SIAM J Matrix Anal A*, vol. 23, pp. 15-41, 2001.

[154] COMSOL Multiphysics Reference Manual, COMSOL Inc., Burlington MA, 2013.

[155] J.C. Lagarias, J.A. Reeds, M.H. Wright, and P.E. Wright, “Convergence properties of the Nelder-Mead simplex method in low dimensions,” *SIAM J Optimiz*, vol. 9, pp. 112-147, 1998.

[156] D.M. Torres and S.A. Harrison, “Nonalcoholic steatohepatitis and noncirrhotic hepatocellular carcinoma: fertile soil,” Semin Liver Dis, vol. 32, pp. 30-38, 2012.

[157] L. Petaja, J. Nuutinen, A. Uusaro, T. Lahtinen, and E. Ruokonen, “Dielectric constant of skin and subcutaneous fat to assess fluid changes after cardiac surgery,” Physiol Meas, vol. 24, no. 2, 2003.

[158] X. Zhu, W. Guo, and Z. Liang, “Determination of the fat content in cow’s milk based on dielectric properties,” Food Bioprocess Tech, vol. 8, no. 7, 1485-1494, 2015.

[159] Z.Y. Guo, Q. Zhang, X.G. Li, and Z.Y. Jing, “Intravoxel incoherent motion diffusion weighted MR imaging for monitoring the instantly therapeutic efficacy of radiofrequency ablation in rabbit VX2 tumors without evident links between conventional perfusion weighted images,” Plos One, vol. 10, 2015.

[160] I. Joo, J.M. Lee, J.H. Yoon, J.J. Jang, J.K. Han, and B.I. Choi, “Nonalcoholic fatty liver disease: intravoxel incoherent motion diffusion-weighted MR imaging – an experimental study in a rabbit model,” Radiology, vol. 270, pp. 131-140, 2014.

[161] J. Patel, E.E. Sigmund, H. Rusinek, M. Oei, J.S. Babb, and B. Taouli, “Diagnosis of cirrhosis with intravoxel incoherent motion diffusion MRI and dynamic contrast-enhanced MRI along and in combination: preliminary experience,” J Magn Reson Imaging, vol. 31, pp. 589-600, 2010.

[162] V. Rieke and K.B. Pauly, “MR thermometry,” J Magn Reson Imaging, vol. 27, pp. 376-390, 2008.

[163] P. Saccomandi, C. Giraudau, F. Davrieux, G. Quero, E. Schena, L. Breschi, F.M. Di Matteo, G. Costamagna, and J. Marescaux, “In vivo image-guided MR thermometry during laser ablation: experience in kidney and liver,” IEEE Int Symposium Med Me, Rome, Italy, 2018.

[164] Y. Kim, C. Audigier, J. Ziegle, M. Friebe, and E.M. Boctor, “Ultrasound thermal monitoring with an external ultrasound source for customized bipolar RF ablation shapes,” Int J Comput Ass Rad, vol. 13, pp. 815-826, 2018.